TECHNISCHE UNIVERSITÄT MÜNCHEN
Physik Department
Theoretische Physik T37

Dissertation

Ions and Peptides at Interfaces: From Ion-specificity to Bioadhesion

Nadine Schwierz

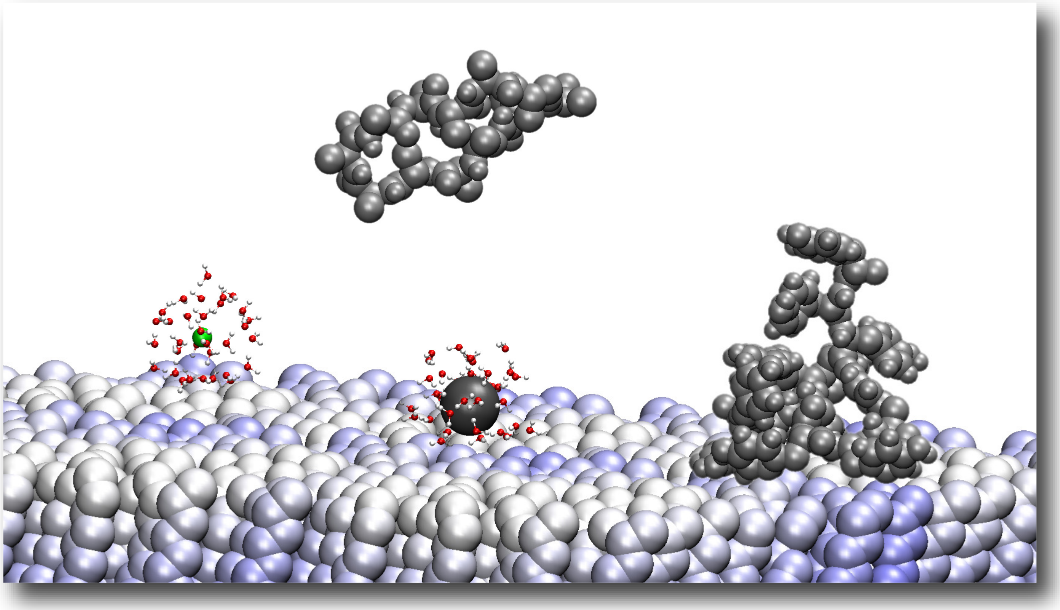

TECHNISCHE UNIVERSITÄT MÜNCHEN
Physik Department
Theoretische Physik T37

Ions and Peptides at Interfaces: From Ion-specificity to Bioadhesion

Dipl.-Phys.
Nadine Schwierz

Vollständiger Abdruck der von der Fakultät für Physik der Technischen Universität München zur Erlangung des akademischen Grades eines

Doktors der Naturwissenschaften (Dr. rer. nat.)

genehmigten Dissertation.

Vorsitzender:		Univ.-Prof. Dr. Thorsten Hugel
Prüfer der Dissertation:	1.	Univ.-Prof. Dr. Roland Netz, Freie Universität Berlin
	2.	Univ.-Prof. Dr. Martin Zacharias

Die Dissertation wurde am 22.11.2011 bei der Technischen Universität München eingereicht und durch die Fakultät für Physik am 15.12.2011 angenommen.

Zwei Dinge sind zu unserer Arbeit nötig: Unermüdliche Ausdauer und die Bereitschaft, etwas, in das man viel Zeit und Arbeit gesteckt hat, wieder wegzuwerfen.

Albert Einstein (1879 - 1955)

Contents

Abstract

Ion specific effects are ubiquitous. The term denotes the fact that most aqueous physicochemical processes not only depend on ion concentration and valency, but also on the ion type. Early on, it was recognized that anions and cations can be ordered reproducibly according to their efficiency to precipitate proteins from solution into the *Hofmeister series*. The identification of the mechanism underlying this series and the implementation into a generally applicable theory remain challenging. Moreover, the universality of the Hofmeister series is called into question by state of the art experiments which reveal a whole spectrum of direct, altered and reversed series.

The aim of the first part of this thesis is to describe this diverse spectrum of experimentally observed phenomena, for which so far no theoretical framework exists. Using molecular modeling, we design model surfaces consisting of biologically relevant surface groups ranging from methyl, hydroxyl, carboxyl to carboxylate groups. We use a novel combination of explicit water molecular dynamics simulations and coarse-grained Poisson-Boltzmann theory. This approach provides microscopic insight into the different interactions responsible for ion specific effects and bridges from computational results to macroscopic experimentally accessible properties. Firstly, we successfully describe the full spectrum of anionic Hofmeister series at surfaces of varying charge and polarity. Secondly, the results are complemented by the cationic Hofmeister series. Thirdly, ion binding to charged groups is investigated. Finally, the fundamental physical correlations underlying ion-specificity are described in a general analytical theory. These results provide a first step toward a clear molecular understanding of the mechanism underlying ion specific effects.

Despite the importance of ion specific effects in biological processes like peptide-surface interactions, it is worthwhile to have a closer look at such systems in the absence of ions. Gaining insight into peptide-surface interactions and controlling their adsorption at synthetic surfaces is the ultimate goal for designing biocompatible implants and fouling resistant surfaces.

In the last part of this thesis, we present the work resulting from a close cooperation with the experimental group of Professor Hugel at TUM. In accordance with experimental single-molecule techniques we develop a fully atomistic description of peptide-surface interactions. A detailed analysis of the involved energetics allows to identify the main contributions underlying peptide adsorption and adsorption resistance.

Zusammenfassung

Ionenspezifische Effekte sind allgegenwärtig. Der Ausdruck bezeichnet die Tatsache, dass die meisten physikochemischen Prozesse in wässriger Lösung nicht nur von der Ionenkonzentration und Wertigkeit sondern auch von der Ionenart anhängen. Es wurde frühzeitig erkannt, dass Anionen und Kationen, entsprechend ihrer Fähigkeit Proteine zu fällen, reproduzierbar in die Hofmeister-Reihe eingeordnet werden können. Bislang ist der grundlegende Mechanismus dieser Reihe unklar und die Beschreibung in einer allgemeingültigen Theorie stellt eine Herausforderung dar. Zudem wird die Allgemeingültigkeit der Hofmeister-Reihe durch modernste Experimente, die ein ganzes Spektrum an direkten, modifizierten und umgekehrten Reihen enthüllen, in Frage gestellt.

Das Ziel des ersten Teils dieser Arbeit ist es, dieses vielfältige Spektrum an experimentellen Phänomenen, für das es bisher keine theoretische Beschreibung gibt, zu erklären. Mit Hilfe von molekularer Modellierung werden Modelloberflächen gestaltet, die aus biologisch relevanten Gruppen wie Methyl-, Hydroxyl-, Carboxyl- oder Carboxylatgruppen bestehen. Hierbei kommt eine neuartige Verknüpfung von Molekulardynamik Simulationen und Poisson-Boltzmann Theorie zum Einsatz. Dieser Ansatz gewährt einen mikroskopischen Einblick in die unterschiedlichen Wechselwirkungen, die grundlegend für ionenspezifische Effekte sind, und stellt eine Verbindung zwischen computergestützten Ergebnissen und makroskopischen, experimentell zugänglichen Größen her. Zuerst wird das gesamte Spektrum der Hofmeister-Reihen von Anionen an Oberflächen mit veränderlicher Landung und Polarität erfolgreich beschrieben. Anschießend werden die Ergebnisse durch die Hofmeister-Reihen von Kationen vervollständigt. Daraufhin wird die Bindung der Ionen an geladene Gruppen genau untersucht. Im Anschluss werden die zentralen physikalischen Zusammenhänge in einer allgemeinen analytischen Theorie zusammengefasst. Diese Ergebnisse legen den Grundstein für ein molekulares Verständnis des grundlegenden Mechnismus von ionenspezifischen Effekten.

Obwohl ionenspezifische Effekte bei biologischen Prozessen wie beispielsweise der Wechselwirkung zwischen einem Peptid und einer Oberfläche eine bedeutende Rolle spielen, lohnt es sich, solche Systeme ohne Ionen näher zu betrachten. Der Einblick in die Peptid-Oberflächenwechselwirkung und die gezielte Steuerung der Peptidadsorption zielen darauf ab, medizinische Implantate biologisch verträglich zu gestalten und fäulnisresistente Oberflächen zu entwickeln.

Im letzten Teil dieser Arbeit werden die Ergebnisse aus einer engen Zusammenarbeit mit der Arbeitsgruppe von Professor Hugel an der TUM vorgestellt. In Übereinstimmung mit Einzelmolekül-Experimenten wird eine vollständige atomistische Beschreibung für die Peptid-Oberflächenwechselwirkung entwickelt. Eine detaillierte Auswertung der einzelnen Energiebeiträge ermöglicht es, die Hauptbeiträge, die grundlegend für die Peptidadsorption und die Adsorptionsresistenz sind, zu identifizieren.

Chapter 1

Introduction and Outline

1.1. From Ion-specificity to Bioadhesion

> *The Hofmeister phenomena remain ubiquitous in physical and biochemistry,*
> *and are as important in the scheme of things as was Mendel's work in genetics.*
>
> Barry W. Ninham

The story about ion specific effects goes back to the late 19th century, when Franz Hofmeister and his co-workers published a series of seven papers with the title "Zur Lehre von der Wirkung der Salze" (about the science of the effect of salt). Hofmeister's work arose at a time when Jan van't Hoff, Svante Arrhenius, Wilhelm Ostwald and Wilhelm Pfeffer contributed remarkable work to the field of ion effects. It is striking that the work predates the concepts of pH and buffer [9]. Moreover, the work was published at a time when the terminology of oppositely charged ions had not entered scientific writing entirely, even though Michael Faraday established his famous laws of electrolysis in 1834 and identified ions as charge carriers in electrolytes.

The important discovery of Hofmeister and his co-workers was that different inorganic salts can be ordered reproducibly according to their efficiency to precipitate proteins from blood serum and hen egg whites [10]. Hofmeister's systematic analysis led to a series for anions and cations, which is nowadays known as the *Hofmeister series* or *lyotropic series* [11–13]. Today, scientists refer to Hofmeister or ion specific phenomena when ions of different size but of the same valency, behave differently [14].

Specific ion effects are ubiquitous in biology and chemistry [15]. The effects range from the distinct influence of different ions on protein stability and denaturation [16–19], protein crystallization [20, 21], protein-protein interactions [22] and protein-DNA interactions [23] to their impact on the function of nucleic acids [24] and enzyme activity [25, 26]. Already in 1910, Traube found the same Hofmeister series to govern more than twenty properties, including water surface tension, solubility of gases and colloids, catalysis of chemical reactions, or irritability of nerve cells [27], suggesting that these diverse phenomena have a common origin [15, 20, 28–33]. However, despite the widespread applicability of the series, ion specific effects continue to defy an all-embracing theory [34].

Over the last decade, there has been increased interest in the Hofmeister series and its molecular origin [9, 12]. The reasons for the renewed interest are the development of advanced experimental techniques like X-ray adsorption spectroscopy [35, 36] and solution neutron and X-ray diffraction [37]. While traditional surface tension and electric potential measurements only indirectly sample the ionic distribution at a surface, the detailed microscopic structure of the interface can now be probed directly with recently developed experimental techniques [38]. Examples for such surface-specific techniques are sum-frequency generation [39, 40] and second-harmonic generation [41–43]. Besides, theoretical models and computer simulations improved significantly over the last decade [9, 34].

For almost a century ion specific effects have been attributed to the changes that ions provoke in the hydrogen bonding network of water [11, 12]. Traditionally, ions are divided into two classes: kosmotropes and chaotropes. If ions are small, the surrounding water molecules are tightly bound and the ion is called kosmotrope. If ions are large, the hydration shell is weakly bound and the ion is called chaotrope. The discrimination of the two classes depends on the strength of the ion-water interaction compared to the water-water interaction [20]. In this simplified picture the making and breaking of water structure is central to the Hofmeister series: kosmotropic ions like fluoride salt-out proteins from solutions (decrease their solubility) and stabilize their folded structure [31]. Chaotropes like thiocyanate denature folded proteins and give rise to salting-in behavior (increase their solubility). However, several recent experiments casted doubt on the central role of water structure [31, 44–46]. Today, there is common agreement that ion-specificity results from direct ion-macromolecule interactions including partial ion dehydration upon surface binding [31]. Therefore, non-uniform ion distributions (accumulation or exclusion) near surfaces are responsible for thermodynamic effects for a very wide range of aqueous processes [47]. Still, heuristic rules are widely used, especially the famous law of matching water affinities by Collins [20, 48, 49], since they turned out to qualitatively describe numerous specific ion effects [9].

The classical electrostatic theories of Debye and Hückel for bulk solutions [50], of Gouy and Chapman for ions at charged surfaces [51, 52] and of Onsager and Samaras for the surface tension [53] do not take ion-specificity into account. Several improvements have been made to these so-called primitive models, taking into account finite ion sizes, ion hydration, polarizability, local variations of the dielectric constant and dispersion [54–59]. The consideration of dispersion forces and short-ranged repulsive interactions due to the finite volume of the ions was proposed in the famous paper by Ninham and Yaminsky [60]. The merit of this approach is to naturally include ion-specificity and to explain the different behavior of ions near the air/water and the oil/water interface. However, the continuum approaches are oversimplified since they neglect the discrete nature of water, especially its geometry around ions and at surfaces. This simplification can even lead to qualitatively wrong thermodynamic results. Still, continuum models have the advantage of providing a general analytical solution and further improvements to these models extend the range of agreement with experiments [61–63].

Promising directions to describe ion specific effects, are computer simulations such as molecular dynamics (MD) and Monte Carlo simulations, which include the properties of water explicitly. This microscopic modeling has helped to understand ion-specificity of relatively simple systems such as the air/water interface [64–66]. Only recently, ion binding to nonpolar and polar groups of a protein has been addressed by simulations [67]. However, the choice of the so-called force field, which is the required input for any molecular simulation, is a subtle issue. Especially, it is still a matter of debate whether polarizability needs to be included or not. The underlying atomistic potential of a classical force field either relies on parameterized functions or on a quantum-mechanical potential derived by quantum chemistry. Although quantum chemical methods are quite accurate, their computational demand limits the accessible simulation time and system size. In classical simulations, polarizability can be taken into account by adding parameterized atomistic polarizability to the force field. In principle, such force fields have the potential to be closer to the full quantum mechanical description of molecular systems. Moreover, the work by Jungwirth and Tobias [65] predicted that adsorption of the large halide ions at the air/water interface is only obtained with polarizable force fields but not with standard non-polarizable ones. However, if non-polarizable force fields are properly optimized, the surface affinity is reproduced in very good agreement with experimental surface tension results [66, 68]. Meaningful results, concerning the simulations of ions, are expected for ionic force fields which are optimized to reproduce thermodynamic bulk properties. Unfortunately, up to now no rational optimization of polarizable ionic force fields exists due to the high complexity of the optimization that already occurs for non-polarizable force fields [68].

With the progress of the last years, the solution to the riddle of the origin of ion specific effects seems to come into reach. Yet, the Hofmeister story does not end here, since more and more exceptions from the presumably universal Hofmeister order appear in the literature. In contrast to Hofmeister's results, the solubility of lysozyme follows the reversed order [21, 59, 69]. The reason is that lysozyme has a very high isoelectric point (pI ≈ 11.16). Experiments using different proteins at different pH reveal that the direct order is obtained for negatively charged proteins (pH>pI) while cationic proteins (pH<pI) show the inverse order [59, 70]. This provides the first evidence that the surface charge influences the Hofmeister order and is further supported using colloidal systems or well-defined surfaces [71–73]. Such simple systems allow to clearly disentangle the influence of the surface charge and the chemical composition of the surface on the Hofmeister order which are of unique importance in protein science as well [18, 47]. It is striking that besides the surface charge, the nature of the surface has a distinct influence on the Hofmeister order [73]. This effect is clearly evident in the reversal which takes place

when the nature of the surface is changed from hydrophobic to hydrophilic [74]. For these reasons, the presumably universal Hofmeister series makes way for a whole spectrum of direct, altered and reversed series and the ordering may depend on temperature, salt concentration, pH, buffer and the nature of the surface [9, 27, 69, 74–76].

The aim of the first part of this thesis (chapter 2-5) is to describe this full spectrum of experimentally observed phenomena for which so far no theoretical framework exists. Often, it is non-trivial to establish a connection between experimentally relevant properties, such as particle aggregation or long-ranged forces, due to time and size restrictions of atomistic modeling of complex biological systems. Therefore, we use a combination of explicit water MD simulations and coarse-grained modeling. This approach provides insight into the microscopic adsorption mechanism and bridges from computational results to macroscopic experimentally accessible properties. Thus, our results provide a first step toward a clear molecular understanding of the diverse and subtle interactions responsible for ion specific effects.

Ion specific effects are important in various biological processes. Especially, the influence of ions on protein-surface interactions are of high importance in fields ranging from bionanotechnology to biomedical engineering. However, it is worthwhile to have a closer look at such systems in the absence of cosolutes like ions.

Intermolecular forces in aqueous solutions determine biological processes like recognition, protein folding and aggregation. Gaining control over nonspecific protein adsorption at artificial surfaces is fundamental in technological and medical applications involving contact of these surfaces with biological fluids. Examples include biosensors monitoring the adsorption of charged proteins [77], sensitive solid-phase immunoassays retaining selectivity even at large serum protein concentrations [78], solid-phase supports for the growth of adhered cells [79] or the initial stage of blood clotting involving adsorption of certain, large proteins to injured vessel walls [80]. Moreover, understanding how to prevent the adsorption of proteins to surfaces is the ultimate goal for designing biocompatible implants and fouling resistant surfaces. The most unfavorable effect of marine biofouling is the increased fuel consumption of ships, since biofouling causes additional drag on a moving vehicle. The proven technology to reduce or prevent biofouling is to use toxic paints or biocides which kill the colonizing organisms [81]. Since this is neither environmentally beneficial nor an option for food industry, there is a high demand to develop chemically inert, nontoxic surface coatings.

Various surface properties have been investigated in the past in order to design surfaces which inhibit the adsorption of fouling species or at least reduce the adsorption strength such that the organism can be removed easily by shear force [82]. An assortment of surface properties is related to adsorption resistance. These include the type of hydrogen bonding at the surface where hydrogen-bond acceptors but not donors are adsorption resistant [83], physical properties such as the sign and density of surface charges [84] as well as the surface energy, commonly measured by water contact angles. The interfacial tension between water and a solid shows an influence on the adsorption of macromolecules which is related to the Berg limit [85]. The Berg limit defines the transition from hydration repulsion to hydrophobic attraction at a contact angle of $\Theta \approx 65^\circ$ [86]. Above the Berg limit, i.e. for hydrophobic surfaces, the surface becomes attractive to adhesion while below, i.e. for hydrophilic surfaces, the interaction becomes negligible [85].

Basic research can provide insight into the adhesion mechanism and help to systematically design adsorption resistant surfaces. The first step in a bottom-up approach to understand complex biomolecule-surface interactions is to focus on a simple model system consisting of the building blocks of proteins - the amino acids. Biomolecular fragments, especially homopolypeptides consisting of a uniform sequence of the same amino acid, are more convenient for a rigorous molecular modeling compared to proteins which consist of hundreds of amino acids. Subsequently, the knowledge gained from simple systems can be applied to large complex systems. Explicit-solvent MD simulations allow a quantitative understanding of peptide-surface interactions [87, 88] and enable an identification of the main contributions in the desorption process [89, 90]. On the experimental side, a particularly enlightening approach to study peptide-surface interactions is single-molecule force spectroscopy with an atomic force microscope (AFM). This method is capable to measure forces in the physiological piconewton range with a spatial sub-nanometer resolution and has been successfully applied to experimentally determine polymer binding to surfaces [91–93].

In the last part of this thesis (chapter 6), we present work resulting from a fruitful cooperation with the experimental group of Professor Hugel at TUM. The combination of simulation and experimental techniques enables us to address peptide-surface interactions from different perspectives and to identify the main contributions underlying peptide adsorption and adsorption resistance, respectively.

1.2. Outline of this Work

The aim of this thesis is to provide a clear molecular understanding of ion specific effects and to identify the main contributions underlying peptide-surface interactions.

Chapter 2 addresses the reversal of the anionic Hofmeister series [1–3]. We introduce a two-scale modeling approach toward anion-specificity at surfaces of varying charge and polarity. Explicit-solvent atomistic MD simulations at neutral hydrophobic and neutral hydrophilic self-assembled monolayers provide potentials of mean force for the sodium cation and the halide anions fluoride, chloride and iodide. The ion-surface potentials are imported into Poisson-Boltzmann theory to calculate ionic distributions at surfaces of arbitrary charge for finite ion concentration. Based on calculated long-ranged electrostatic forces and coagulation properties, we obtain the direct anionic Hofmeister series at negatively charged hydrophobic surfaces. Reversal of the Hofmeister series takes place when going to negative polar or to positive nonpolar surfaces, leading to the indirect series. For positively charged polar surfaces the direct series is again obtained. This double reversal is in full accordance with a recent experimental classification of colloidal coagulation kinetics and also reflects the trends of the ion specific solubility properties of proteins.

In chapter 3, the anionic Hofmeister series is complemented by the cationic series for the halide cations lithium, sodium, potassium and cesium [4]. We extend the two-scale modeling approach to more realistic surfaces, consisting of hydrophobic and hydrophilic surface patches, similar to proteins. The microscopic ion-surface interaction gives insight into the long standing mystery why small anions but large cations are more efficient in precipitating proteins from solutions. We provide evidence that cations can have as strong an effect on macroscopic properties as anions. However, the underlying microscopic mechanism is by far more complex for cations due to their in general smaller size.

In chapter 4, we investigate ion binding to charged surface groups [5]. Ion binding is one of the central mechanisms for ion-specificity if ionizable groups like carboxyl groups are present on the surface of a macromolecule. The investigation of ion binding in dependence of the degree of dissociation complements our bottom-up approach to provide a clear molecular understanding of possible ion-macromolecule interactions.

In chapter 5, we reduce the in general complex ion-surface interactions to a generic continuum model [6]. The model is simple enough to be solved analytically on the Poisson-Boltzmann level and can be analyzed globally for varying surface charge, salt concentration and ion-surface affinity. On the other hand, it takes long-ranged electrostatic, short-ranged entropic and depletion effects into account and displays the salting-in/salting-out behavior which is characteristic for proteins. Moreover, the strength of this approach is that the generic model can be adjusted easily to realistic ion-surface interactions obtained by simulations. The resulting Hofmeister phase diagram features the full spectrum of experimentally observed Hofmeister order.

In chapter 6, we present a combination of simulations and experimental techniques to investigate peptide-surface interactions [7, 8]. In close collaboration with the group of Professor Hugel at TUM, we develop a fully atomistic description of the complete system including peptide, surface and water. To characterize peptide-surface interactions, we determine the force necessary to desorb homopolypeptides of varying side-chain hydrophobicity from self-assembled monolayers using explicit water MD simulations and single-molecule AFM experiments. The surface hydrophobicity is tailored in a well defined and reproducible fashion by using different functional methyl and hydroxyl end-groups. A detailed analysis of the involved energetics allows to identify the main contributions underlying the adsorption of peptides at the hydrophobic surfaces and the adsorption resistance of the hydrophilic surfaces.

In chapter 7, we summarize the main results of this work and give an outlook on possibilities of further research.

Chapter 2

Reversed Anionic Hofmeister Series

2.1. Introduction

2.1.1. Motivation

More than 120 years ago, Hofmeister discovered that different ions can be ordered reproducibly according to their efficiency in precipitating hen-egg white proteins [10]. That sequence now runs under the name *Hofmeister series* (HS) and is e.g. for the halide anions directly related to the ion size: the large iodide ion is less efficient than the smaller fluoride ion, meaning that a higher concentration of I^- is needed compared to F^- in order to precipitate egg white proteins from solution. Already in 1910, Traube found the same HS to govern more than twenty other properties, including water surface tension, solubility of gases and colloids, catalysis of chemical reactions, or the irritability of nerve cells [27], suggesting a common origin for these vastly different phenomena [15, 20, 28–33]. We now know that the process observed by Hofmeister is essentially related to the precipitation of ovalbumin, at neutral pH a negatively charged protein and the main constituent of egg white [59]. Early on, it was realized that the different binding affinities of ions to hydrophobic surface patches or groups not only explain ion specific protein precipitation [18] but also ion specific peptide denaturation [16, 19] via essentially the same mechanism: Ions that are strongly repelled from hydrophobic surfaces (such as F^-) will raise the interfacial tension strongly. Realizing that the driving force for protein aggregation mainly comes from the adhesion between hydrophobic surface patches, it transpires that those ions will be strong precipitators compared to ions that are less strongly repelled or even attracted to hydrophobic surfaces (such as I^-). By the same token, since peptide denaturing mainly involves solvation of hydrophobic groups that are buried in the interior of the native protein structure, it is clear that ions that strongly precipitate proteins from solution (such as F^-) at the same time tend to be only weakly denaturing agents or even structural stabilizers. In contrast, salts that adsorb to hydrophobic interfaces can be as strong denaturants as urea [19] and are at the same time only weak precipitators.

Analogous trends as described here for anions are also observed for cations as will be discussed in the next chapter.

But the HS story does not end here: Firstly, the ion ordering is found to be reversed for cationic proteins, i.e. for proteins at pH below their isoelectric point [21, 69], which is theoretically explained by the combination of specific ion-surface interactions and Coulombic screening effects [59]. Secondly, surfaces of folded peptides contain a mix of hydrophobic and hydrophilic groups, and based on experimental data ionic affinities to those surface groups have been inferred to be different [18, 47]. Roughly speaking, the outer surface of a protein displays of the order of 1/3 hydrophobic and 2/3 hydrophilic patches, while the interior of a protein contains only about 1/3 hydrophilic groups (mostly associated with the peptide backbone) [47]. This reconciles the surprising finding that many cosolutes that raise the interfacial tension of water (such as urea) act at the same time as strong denaturants [94, 95]: The presence of polar groups on protein surfaces means that the ion-specificity of nonpolar (e.g. air/water or oil/water) interfaces and protein surfaces are expected to be fundamentally different. Furthermore, the different polar/nonpolar compositions of the outer surface and the interior of proteins implies that ions influence protein precipitation and denaturation in different ways. Thirdly and finally, ionic binding to surfaces involves water replacement and thus in a more general framework water-osmotic effects count as well [96, 97]. Our modeling strategy addresses all 3 issues.

In the following we denote by the polarity of a surface its degree of hydrophilicity, which we treat as a parameter independent of the surface charge. To be specific, we denote a surface which has only small partial charges on terminal groups and is characterized by a large contact angle as *nonpolar*, and a surface which has large positive and negative partial charges on terminal groups (but not necessarily a net charge) and which is able to hydrogen bond with interfacial water and thus has a small (or vanishing) contact angle as *polar*. Therefore, in our modeling we allow both polar and nonpolar surfaces to carry a net charge. For a nonpolar surface this would correspond to a situation where the charge is distributed evenly over the surface, which can be realized using back-gated semiconductors or self-assembled monolayers [77]. For typical biological or organic surfaces a charged nonpolar surface corresponds to an idealized limit. Yet, the distinction between surface polarity and surface charge has been recently used to successfully classify a broad range of different experimental colloidal surfaces [71, 72, 74], which motivated the present study.

Although, in the biological community proteins are the ultimate object of ion specific studies, they are far from ideal for understanding the physicochemical foundations of Hofmeister effects. This is in part caused by the subtle interplay of (partial) protein unfolding and aggregation, but mostly due to the fact that proteins by evolutionary design exhibit a rather narrow range of surface polarity and charge and therefore do not allow to explore wide variations of these relevant surface parameters. In contrast, synthetic colloids are very stable and can be produced with almost any surface charge and polarity. In fact, in a series of groundbreaking studies, it was shown that rather hydrophobic anionic colloids show the direct HS while the series is reversed for cationic colloids [71, 74], similar to proteins. Even more striking, when going from hydrophobic to very polar

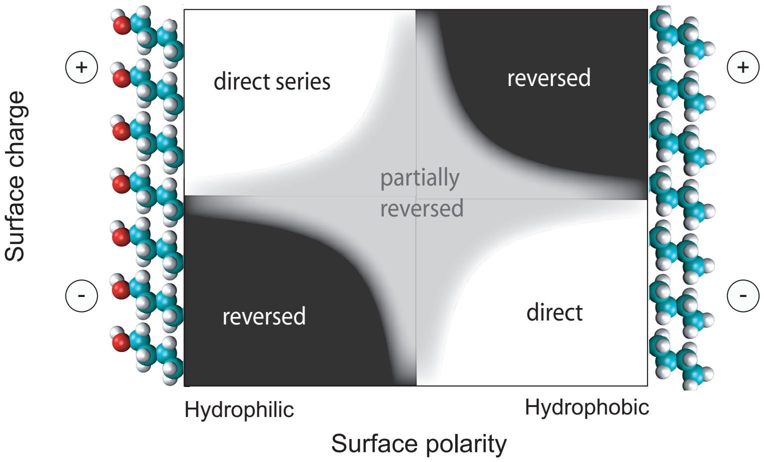

Figure 2.1.: Schematic Hofmeister phase diagram as a function of surface charge and polarity, featuring direct and reversed (i.e. indirect) series as well as partial reversion (derived from our modeling results and in agreement with experimental results for colloids [74]).

colloids another reversal takes place: Anionic polar colloids obey the reverse HS, cationic polar colloids obey the direct HS, while for intermediate situations partial reversal is observed [72, 74]. Thus, colloids allow to clearly disentangle the striking influence of surface charge and polarity on Hofmeister effects, factors that are found to be important in protein science as well [18, 47]. This situation, cast into a schematic phase diagram in Fig. 2.1, is the main subject of this communication and is approached by a combination of atomistic simulation and coarse-grained modeling.

During the last decade, the modeling of Hofmeister effects steadily progressed. It is now generally accepted that the subtle interplay of ion hydration in bulk and partial ion dehydration upon surface binding has to be accounted for by explicit water simulations if ion specificity is to be understood beyond the purely heuristic level of fitting experimental data (for a recent example, see [98]). The salting-out of small hydrophobic solutes was shown to follow the direct HS [99, 100], as in classical experimental solubility studies on e.g. benzene in water [16]. For hydrophobic plates, the repulsion and thus depletion of ions from the nonpolar surfaces was found to be directly proportional to the ionic surface-charge density [101, 102], similar to the free air-water interface where large anions such as iodide even exhibit slight interfacial enhancement [38, 65, 103]. Ionic depletion increases the interfacial tension, and in the absence of long-ranged electrostatic effects gives rise to a short-ranged inter-plate attraction, as directly extracted from the simulations [102]. For surfaces exhibiting both nonpolar and polar groups or patches, the situation is more complicated for two reasons: i) Cl^- binds stronger than I^- to cationic surface groups, indicative of a reversed HS, i.e., the smaller the anion, the stronger the binding [67]. ii) Because of the long relaxation times of ion binding at polar surface groups, all-atomistic simulations at finite salt concentration become cumbersome, suggesting multiscale modeling approaches as an alternative. Indeed, potentials of mean force (PMFs) between ions and nonpolar surfaces derived from explicit-solvent simulations have been successfully used in the context of integral equation theory [104], Poisson-Boltzmann (PB) mean-field theory [105] and primitive model Monte Carlo simulations [106] to calculate effective forces between mesoscopic bodies.

2.1.2. Outline

Theories for predicting or explaining Hofmeister effects have appeared in the literature, but no attempt was made to describe the full spectrum of experimental phenomena, in particular the HS reversal when reversing the charge and the polar/nonpolar character of the surface, and no theoretical framework exists that would account for the all too often neglected phenomenon of partial HS reversal. In this chapter we fill this gap by combining molecular dynamics (MD) simulations of single ions at neutral polar and neutral nonpolar surfaces, which yield ionic PMFs, with PB theory which accounts for surface charge and finite salt concentration effects. Although, cations exhibit direct and reversed ionic series as well [73, 98], we here consider a small subset of the anionic HS consisting of the salts NaF, NaCl, and NaI. The reason is mainly that a systematically derived force field for these ions exists [68] which was shown to reproduce the experimental trends for the air/water interfacial tension very well [66].

We derive three complementary observables that highlight different ion specific features: i) The tension of a single surface, which mirrors ionic surface affinities and clearly displays the HS reversal when going from nonpolar to polar surfaces. ii) The electrostatic far-field generated by asymmetric surface adsorption of anions and cations, which directly illustrates the HS reversal upon reversing the surface charge. iii) The critical coagulation concentration as function of surface charge, which is a measure for the coagulation kinetics of colloids and results from the balance of dispersion attraction and electrostatic repulsion. In summary, the double reversal of the Hofmeister series seen in colloidal interaction when changing the surface polarity and when changing the surface charge [71, 72, 74] is shown to be a direct consequence of ion specific surface adsorption which gives rise to an ion specific double layer charge.

2.2. Methods

2.2.1. Simulation Details

In the simulations the surface is a 3.5 nm × 3.464 nm self-assembled monolayer (SAM) consisting of 56 $C_{20}H_{40}$ chains with a terminal CH_3-group for the nonpolar and a terminal CH_2OH-group for the polar SAM. The chain lattice spacing corresponds to a gold (111) substrate with a tilt angle of 30° close to experimental values. The lower 6 C-atoms of each chain are restrained by harmonic potentials with spring constant $k = 5 \times 10^5$ kJ/(mol nm^2). The simulation box has an extension of 9 nm in the z-direction and is filled with about 2,700 SPC/E water molecules. The SAM is modeled with the GROMOS96 force field [107]. The force field parameters used for anions and cations were previously optimized for the SPC/E water model [108] to reproduce thermodynamic solvation properties [68]. From the three different cation parameter sets given in [68] we have used parameter set 2 for Na^+ in our calculations. This choice was mainly motivated by recent work that showed that relatively high Lennard-Jones energy parameter for cations yield accurate ion pairing properties as judged by comparison with experimental osmotic coefficient data [109]. The terminal CH_3-group on the hydrophobic SAM carries a small negative charge, which is negligible with respect to the wetting properties and still renders a very hydrophobic surface [110]. All Lennard-Jones parameters are listed in table A.5 of the appendix A. The simulations are done at a temperature of 300 K and a pressure of 1 bar maintained by anisotropic pressure coupling. Periodic boundary conditions are applied, long range Coulomb forces are calculated using the particle-mesh Ewald summation [111] and for the van-der-Waals interactions a cutoff radius of 1.2 nm is used. A single ion is placed into the water phase and its potential of mean force (PMF) is calculated by umbrella sampling [112] with a window spacing of 0.025 nm and 1 ns simulation time discarding the first 200 ps for ions at the hydrophobic surface and 3 ns simulation time discarding the first 1 ns at the hydrophilic surface using a time step of 2 fs and the weighted histogram analysis method [113]. The density profile for 1M NaI at the hydrophobic and hydrophilic SAM surfaces is calculated in 100 ns simulations. All simulations are performed with the Gromacs 3.3.1 simulation package [114].

2.2.2. Poisson-Boltzmann Modeling

The PB equation for a planar surface including ion specific PMFs reads [59, 105, 115]

$$\epsilon_0 \frac{d}{dz} \epsilon(z) \frac{d}{dz} \Phi(z) = -\sum_i q_i c_0 e^{-\left(V_i^{\mathrm{PMF}}(z) + q_i \Phi(z)\right)/k_B T} \tag{2.1}$$

where z is the distance perpendicular to the surface, q_i is the charge of ions of type i, c_0 is the bulk salt concentration, ϵ_0 is the dielectric constant of vacuum, $\epsilon(z)$ is the relative dielectric constant profile as a function of the distance from the surface, $V_i^{\mathrm{PMF}}(z)$ is the PMF of the i-th ion as obtained in the MD simulations, and $\Phi(z)$ is the electrostatic potential. The PMFs are fitted by heuristic fit functions which are given explicitly in the appendix A (table A.1). The local dielectric constant $\epsilon(z)$ which enters the Poisson-Boltzmann equation is assumed proportional to the water density

$$\epsilon(z) = \epsilon_{\mathrm{SAM}} + \frac{\rho(z)}{\rho_0} \left(\epsilon - \epsilon_{\mathrm{SAM}}\right) \tag{2.2}$$

where $\epsilon_{\mathrm{SAM}} = 4$ is the value taken for the dielectric constant of the SAM, $\epsilon = 78$ is the dielectric constant of water, $\rho(z)$ is the water density profile from MD simulation approximated by a fit function and ρ_0 is the bulk density of water. The linear relation between water density and dielectric constant profile has been confirmed in extensive MD simulations where the local dielectric constant has been determined from the local dipolar fluctuation strength.

To determine the surface tension change with increasing bulk salt concentration according to the Gibbs adsorption equation, the position of the Gibbs dividing surface z_{GDS} is calculated from the requirement, that the surface excess for water Γ_w itself vanishes

$$\Gamma_w = \int_{-\infty}^{z_\mathrm{GDS}} \rho(z)\mathrm{d}z + \int_{z_\mathrm{GDS}}^{\infty} \left(\rho(z) - \rho_0\right)\mathrm{d}z = 0. \tag{2.3}$$

The fit function and fit parameters of the density profile $\rho(z)$ at the CH_3-terminated and the OH-terminated SAM as well as the position of the Gibbs dividing surface are given in the appendix A (table A.6). Eq. 2.1 is solved numerically on a one dimensional grid with a lattice constant of 1 pm, which is small enough that discretization effects can be neglected. For a single surface, the potential satisfies the boundary conditions (i) $\Phi(z) = 0$ in bulk water (z $\to \infty$) and (ii) $\Phi(z) =$ const for z $\to -\infty$. For two surfaces at distance D we use in Eq. 2.1 the sum $V_i^\mathrm{PMF}(z) + V_i^\mathrm{PMF}(D - z)$ and the symmetry boundary condition $\mathrm{d}\Phi(z)/\mathrm{d}z|_{z=D/2} = 0$ at the midplane. An external surface charge is modeled by the modified boundary condition

$$\epsilon_0\epsilon(z)\frac{\mathrm{d}\Phi}{\mathrm{d}z} = -\sigma_\mathrm{surf} \tag{2.4}$$

at the surface at $z = 0$. The location of the surface, i.e. the origin of the z-coordinate, is defined by the mean position of the terminal C and O surface atoms for the hydrophobic and hydrophilic surfaces, respectively. The concentration profile of the i-th ionic species $c_i(z)$ is given by

$$c_i(z) = c_0 e^{-\left(V_i^\mathrm{PMF}(z) + q_i\Phi(z)\right)/k_BT}. \tag{2.5}$$

We calculate the surface tension increment with respect to the uncharged surface at $c_0 = 0$ via thermodynamic integration

$$\Delta\gamma = -k_BT\sum_i \int_0^{c_0} \mathrm{d}c_0' \frac{\Gamma_i}{c_0'} + \int_0^{\sigma_\mathrm{surf}} \mathrm{d}\sigma'_\mathrm{surf}\Phi(z=0) \tag{2.6}$$

valid for nearly ideal solutions with the activities replaced by concentrations. Note that in Eq. 2.6, Γ_i denotes the surface excess of ionic species i for vanishing surface charge $\sigma_\mathrm{surf} = 0$, while the surface potential $\Phi(z = 0)$ is calculated at finite bulk salt concentration c_0 and varying surface charge σ'_surf. The surface excess is for the single surface given by

$$\Gamma_i = \int_{-\infty}^{z_\mathrm{GDS}} c_i(z)\mathrm{d}z + \int_{z_\mathrm{GDS}}^{\infty} \left(c_i(z) - c_0\right)\mathrm{d}z \tag{2.7}$$

and for the slab geometry by

$$\Gamma_i = 2\left[\int_{-\infty}^{z_\mathrm{GDS}} c_i(z)\mathrm{d}z + \int_{z_\mathrm{GDS}}^{D/2} \left(c_i(z) - c_0\right)\mathrm{d}z\right]. \tag{2.8}$$

2.2.3. Debye-Hückel Limit

Sufficiently far from the surface where the PMFs vanish and the potential is small, Eq. 2.1 can be linearized. The Debye-Hückel (DH) potential Φ_DH is calculated by fitting the electrostatic potential $\Phi(z)$ obtained by the extended Poisson-Boltzmann equation at large separations to the expression

$$\Phi(z) \simeq \Phi_{\mathrm{DH}} e^{-\kappa z} \tag{2.9}$$

where the Debye screening length κ^{-1} is defined by $\kappa = \sqrt{2q^2 c_0/\epsilon\epsilon_0 k_B T}$. Note that the DH potential Φ_{DH} is via the relation

$$\sigma_{\mathrm{DH}} = \epsilon\epsilon_0 \kappa \Phi_{\mathrm{DH}} \tag{2.10}$$

a measure of the effective or renormalized surface charge density σ_{DH} [116] and allows to predict the long-ranged forces between two surfaces. Note that the value of Φ_{DH} and thus of σ_{DH} depends sensitively on the location of the surface, i.e. the position where $z = 0$. The ionic pressure $p(D, c_0)$ between two surfaces follows from the surface tension change $\Delta\gamma$ in Eq. 2.6 as

$$p(D, c_0) = -\mathrm{d}\Delta\gamma(D, c_0)/\mathrm{d}D. \tag{2.11}$$

In the Debye-Hückel limit, i.e. at large surface separation, the pressure between two surfaces reads [117]

$$p(D, c_0) = \frac{2\sigma_{\mathrm{DH}}^2}{\epsilon\epsilon_0} \left(\frac{2 + e^{D\kappa} + e^{-D\kappa}}{(e^{D\kappa} - e^{-D\kappa})^2} \right). \tag{2.12}$$

where the effective surface charge density σ_{DH} is related to Φ_{DH} via Eq. 2.10.

2.2.4. Critical Coagulation Concentration

Colloidal stability results from a balance between double-layer repulsion and van-der-Waals attraction. The critical coagulation concentration c_{coag} of the salt is commonly defined as the bulk salt concentration where the repulsive barrier vanishes. In order to connect to the experimental colloid scenario [71, 72, 74], we derive the total potential V_{tot} between two spheres consisting of the sum of van-der-Waals attraction and electrostatic double-layer repulsion. To that end, we first construct the total potential per unit area between two planar surfaces

$$V_{\mathrm{tot}}^{\mathrm{plane}}(D) = V_{\mathrm{A}}^{\mathrm{plane}}(D) + V_{\mathrm{R}}^{\mathrm{plane}}(D) \tag{2.13}$$

which consists of the attractive van-der-Waals interaction energy V_A^{plane} and the repulsive electrostatic interaction energy V_R^{plane}. According to the standard DLVO theory, for two surfaces at separation D, those expressions are given by

$$V_{\mathrm{A}}^{\mathrm{plane}}(D) = -H/(12\pi D^2) \tag{2.14}$$

where H is the Hamaker constant and

$$V_{\mathrm{R}}^{\mathrm{plane}}(D) = 2\epsilon\epsilon_0 \kappa \Phi_{\mathrm{DH}}^2 e^{-\kappa D} \tag{2.15}$$

where Φ_{DH} is the surface potential according to linearized Debye-Hückel theory [116]. The Derjaguin approximation relates the total force between two spherical particles of equal radius R at surface separation D, given by $F_{\mathrm{tot}}(D) = -dV_{\mathrm{tot}}(D)/dD$, to the potential per unit area between two corresponding planes by $F_{\mathrm{tot}}(D) = \pi R V_{\mathrm{tot}}^{\mathrm{plane}}(D)$ [116]. The analogous expression for the force between a plane and a sphere, as relevant for the experimental setup of Ref. [118], is given by $F_{\mathrm{tot}}(D) = 2\pi R V_{\mathrm{tot}}^{\mathrm{plane}}(D)$ [116]. Integrating the force $F_{\mathrm{tot}}(D)$, we thus obtain for the potential between two spheres

$$V_{\mathrm{tot}}(D) = \pi R \left(-\frac{H}{12\pi D} + 2\epsilon_0 \epsilon \Phi_{\mathrm{DH}}^2 e^{-\kappa D} \right). \tag{2.16}$$

For low salt concentration, V_{tot} exhibits a repulsive barrier that separates the divergent minimum at zero separation from a local minimum at finite separation. At higher salt concentration the barrier height decreases and passes through zero. According to simple coagulation kinetic theory, the salt concentration at which the barrier height vanishes, defined by the equations $V_{\mathrm{tot}}(D) = dV_{\mathrm{tot}}(D)/dD = 0$, defines the critical coagulation concentration c_{coag} [116]. This condition can be explicitly written as

$$c_{\mathrm{coag}} = \frac{288(\epsilon\epsilon_0)^3 \pi^2 k_B T \Phi_{\mathrm{DH}}^4}{\exp(2) H^2 q^2}. \tag{2.17}$$

For the Hamaker constant we take a value $H = 2.2 \times 10^{-21}$ J as appropriate for silica surfaces [118]. As Φ_{DH} depends implicitly on the salt concentration, Eq. 2.17 has to be solved numerically. Note that Eq. 2.17 by construction is only valid for low c_0, the results we present in this paper for high c_0 are only indicative, since in this case the barrier occurs at such small surface separation that short-range interactions between the surfaces are important as well. To facilitate the numerical solution, we fit the dependence of the Debye-Hückel surface potential Φ_{DH} on the salt concentration c_0 and bare surface charge σ_{surf} to a polynomial which is given in the appendix A (table A.7). Using the asymptotic result for Φ_{DH}, Eq. 2.17 can be solved numerically to obtain the critical coagulation concentration c_{coag}.

2.3. Results and Discussion

2.3.1. Ion-surface Interaction Potentials

We study ions at two different surfaces, both formed from self-assembled monolayers (SAMs) of end-functionalized alkane chains. Fig. 2.2 displays the main simulation result, namely the ionic PMFs on the hydrophobic SAM, A, with nonpolar methyl end-groups, and on the hydrophilic SAM, B, where each alkane chain is terminated by a polar hydroxyl end-group, with the origin ($z = 0$) defined by the mean position of the terminal C and O surface atoms, respectively. The water density profile obtained by MD simulations and the fit function $\rho(z)$ at the hydrophobic and at the hydrophilic surface are shown in Fig. 2.2 to the right. The water density of the first density maximum is slightly larger at the hydrophobic surface as compared to the hydrophilic surface. This is not a general feature but rather related to the specific geometry of the hydrophilic and hydrophobic surfaces employed in our simulations, see for example Ref. [119] for simulation results

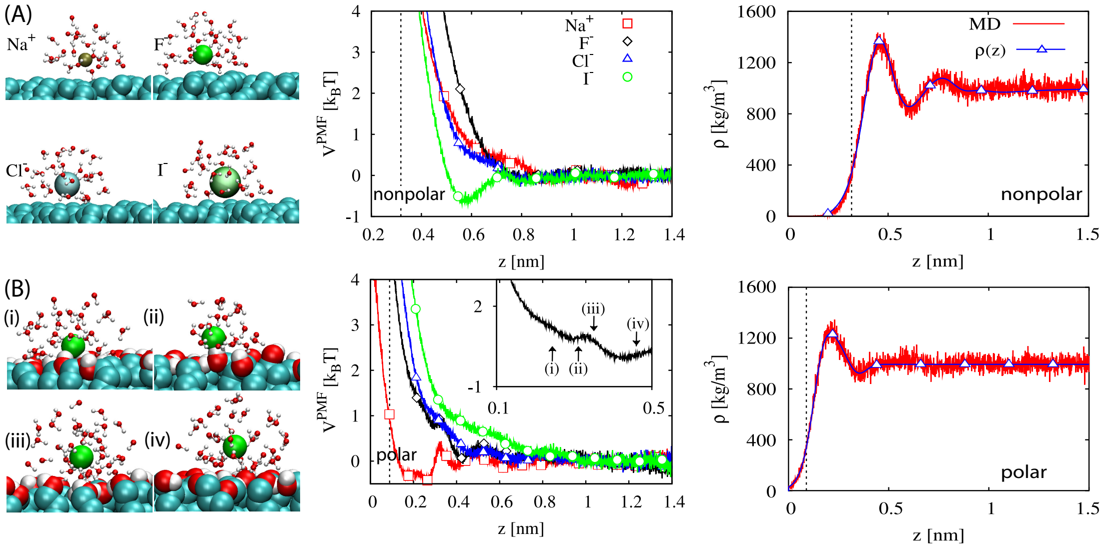

Figure 2.2.: (A) Simulation results at the hydrophobic CH_3-terminated SAM. Left: Snapshots of all ions at fixed surface separation $z = 0.575$ nm (where the I^- PMF shows a minimum). Water molecules within 6Å of the ions are shown and ionic sizes correspond to their Pauling radii. Middle: Potentials of mean force (PMFs); vertical broken line denotes the position of the Gibbs dividing surface z_{GDS}. Right: Water density profile obtained by MD simulation and fit function $\rho(z)$. (B) Results for the hydrophilic OH-terminated SAM. Middle: PMFs of all ions. The inset shows the enlarged F^- PMF and indicates the surface separations for which snapshots of the hydration shell around F^- are shown to the left. Right: Water density profile and fit function $\rho(z)$.

on diamond surfaces or Ref. [120] for simulations on ordered Lennard-Jones surfaces. The ionic adsorption behavior at the nonpolar surface is quite similar to the air/water interface [38, 65, 105]: As seen from the PMFs, the large iodide ion is attracted to the surface, while the smaller halide ions and the sodium cation are repelled. The snapshots (all taken at the distance where the I^- PMF shows a minimum) in Fig. 2.2A show that I^- has partially stripped off its water hydration layer in contrast to the smaller ions, and illustrates that hydrophobic effects are connected to the observed ion-specificity, as at the air-water interface [105]. At the polar surface in Fig. 2.2B the anionic specificity is less pronounced and the situation is in fact reversed for the halides: the small F^- is least repelled from the surface compared to the larger Cl^- and I^-. The snapshots for F^- at four different separations in Fig. 2.2B show that F^- for the smallest separation (i) forms two hydrogen bonds with surface hydroxyl groups, while the slight maximum in the PMF (iii) can be traced back to the unfavorable compression of the first hydration shell of water between the ion and the surface. For even larger separation (iv) the hydration layer is nearly unperturbed and the PMF is essentially flat. This reversal of anion binding affinities (central to Collins' empirical *like-seeks-like* rule [20]) is by no means straightforward: There is no obvious reason why a small F^- ion should show a higher affinity to OH surface groups than to hydration water when compared to larger ions and fine details such as the interfacial water structure and the surface geometry probably matter. Note that Na^+ is most strongly adsorbed of all ions on the polar surface, which has to do with its small hydration radius that allows the formation of a tight ion pair with the surface oxygen. The reversal of anionic binding affinities when going from nonpolar to polar surfaces, in agreement with previous simulations [106], is only one ingredient to the full story of HS reversal.

2.3.2. Ionic Density Profiles and Long-ranged Forces

The extended PB Eq. 2.1 treats the long-ranged electrostatic interactions between ions and the net surface charge and among the ions at finite bulk salt concentration c_0 on an approximate mean-field level and at the same time incorporates the ion specific surface interactions via the PMFs from the MD simulations. The rational behind this splitting, which is at the core of our two-scale modeling approach, is that long-ranged electrostatic interactions are handled quite accurately by the PB approach but lead to various problems in MD simulations. Corrections to the PB approximation have been amply discussed in the literature but are not pursued in this paper, for a review see [121]. The ion concentration profiles for different c_0 follow from Eq. 2.5 and are shown in Fig. 2.3A and C for NaI at the nonpolar and polar surfaces. At the hydrophobic surface I^- adsorbs stronger than Na^+ , leading to a pronounced double layer. The relative adsorption peak of iodide decreases with increasing bulk salt concentration c_0 while the corresponding Na^+ peak increases due to the shrinking screening length. In contrast, at the hydrophilic surface Na^+ adsorbs stronger while I^- is repelled from the interface. The PB approach makes drastic approximations, to give insight into the robustness of all further results we compare in Fig. 2.3B and D PB predictions and MD simulations for a 1M NaI solution at the nonpolar and polar surfaces, respectively. In each graph one can discern deviations between the PB predictions and the actual simulations, especially further away from the surface where specific interactions between the ions become more important than the ion specific interactions with the surface. However, the difference in ion adsorption on the

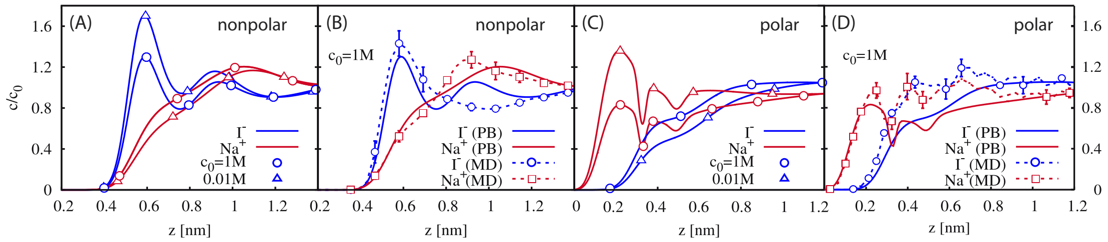

Figure 2.3.: (A) Ion concentration profiles of NaI at the $\mathrm{CH_3}$-SAM obtained from Poisson-Boltzmann (PB) modeling at two different bulk concentrations c_0. (B) Density profile of 1M NaI at the $\mathrm{CH_3}$-SAM from PB compared with explicit finite-concentration MD simulations. (C) Ion concentration profiles of NaI at the hydrophilic OH-terminated SAM from PB. (D) Density profile of 1M NaI at the OH-SAM from PB compared with explicit finite-concentration MD simulations.

polar and nonpolar surfaces is brought out quite accurately by the PB approach. Since all other derived quantities such as surface tension, potential and pressure follow without additional approximations from the density profiles, we are led to conclude that our two-scale modelling approach confidently yields the differences between the ion specific adsorption on polar and nonpolar surfaces.

The electrostatic potential $\Phi(z)$ from the solution of Eq. 2.1 is shown in Fig. 2.4A for NaI at the nonpolar surface at concentration 0.01M and 1M (broken lines) and is compared with an asymptotic exponential fit according to Eq. 2.9 which is equivalent to the linearized Debye-Hückel (DH) theory (solid lines). The comparison becomes excellent for large distances. The DH potential is via Eq. 2.10 related to the effective surface charge σ_{DH} and allows to predict the long-ranged forces between two surfaces, as will be discussed further below. The dependence of Φ_{DH} on the bulk salt concentration is shown in Fig. 2.4B and C for the hydrophobic and hydrophilic SAM. The reversal of the ionic adsorption affinities is clearly recognized: On the nonpolar surface I^- adsorbs most strongly and the potential Φ_{DH} is most negative for NaI and -conversely- positive for NaF. Na^+ and Cl^- have roughly similar PMFs and therefore the potential is quite small. The situation is reversed on the hydrophilic surface: Here, F^- adsorbs strongest. Since Na^+ adsorbs stronger than all anions, the surface potential Φ_{DH} is positive and smallest for NaF and grows as one goes via NaCl to NaI. Fig. 2.4D shows the dependence of Φ_{DH} on the bare surface charge σ_{surf} for 100 mM bulk salt concentration at the hydrophobic

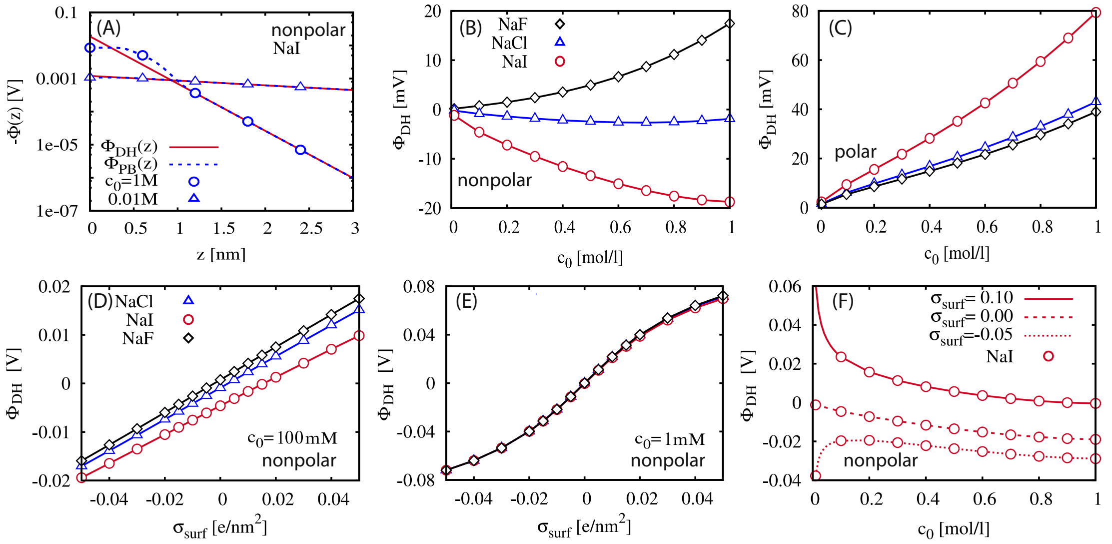

Figure 2.4.: (A) Electrostatic potential distribution $\Phi(z)$ for NaI solutions at the nonpolar surface at two bulk concentrations from PB (broken lines) compared with Debye-Hückel (DH) far-field predictions (solid lines) $\Phi_{\mathrm{DH}} e^{-\kappa z}$. DH potential Φ_{DH} at (B) CH_3-SAM and (C) at OH-SAM. (D) Φ_{DH} as a function of the bare surface charge density σ_{surf} for a bulk salt concentration c_0 =100 mM and (E) for c_0 =1mM at the CH_3-SAM . (F) Φ_{DH} as a function of the bulk salt concentration c_0 of NaI for different values of the the external surface charge density σ_{surf} at the CH_3-SAM.

SAM/water interface. For small values of σ_{surf} and relatively large salt concentration the Debye-Hückel potential increases linearly with increasing surface charge, while for large surface charges and small salt concentration $c_0 = 1\text{mM}$ the increase is nonlinear (Fig. 2.4E). For $c_0 = 1\text{mM}$ the ion-specificity is small and overshadowed by the long-ranged electrostatics while for $c_0 = 100\text{mM}$ electrostatic interactions are sufficiently screened and thus ion-specificity is more pronounced. Fig. 2.4F shows the dependence of the DH potential on the bulk salt concentration of NaI for different values of the external surface charge density σ_{surf}. For positive surface charge the DH potential is positive at low salt concentrations. With increasing bulk concentration of NaI, more iodide ions adsorb, gradually neutralizing the positive surface charge, hence suppressing the electrostatic double layer repulsion between two surfaces in solution and eventually leading to $\Phi_{\text{DH}} = 0$, which defines an instability, as shown in Fig. 2.6B and is discussed in detail later on. At even higher salt concentrations, repulsion reemerges due to surface charge reversal by excess adsorbed anions. For negative surface charge the DH potential is non-monotonic due to the competition between charge screening and ion adsorption effects. Fig. 2.4D-F show that the effective charge of a surface, as defined by the strength and sign of the long-ranged part of the electrostatic potential far from the surface, is strongly influenced by the presence and strength of ion specific adsorption on surfaces.

In Fig. 2.5A and B we show the pressure between two hydrophobic and hydrophilic surfaces as a function of their separation D for 100 mM bulk salt concentration as obtained from PB theory, using Eq. 2.6 and Eq. 2.11 (data points). The lines show the pressure calculated from Eq. 2.12, based on the asymptotic results for Φ_{DH}. The agreement is perfect for large distances. At all surfaces ion specific adsorption leads to effectively charged surfaces, which interact via screened Coulomb interactions with each other. Since we consider identical surfaces, the effective charges on the two opposing surfaces are the same, resulting in long-distance repulsion and thus stabilization (conversely, attraction is expected for unequal pairs of polar/nonpolar surfaces). The insets show the short-distance pressure where both data points and broken lines denote the PB results.

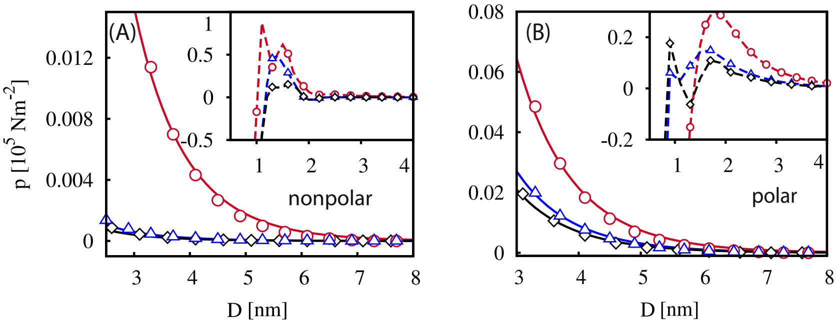

Figure 2.5.: Pressure as function of distance D between (A) two CH_3-terminated SAMs and (B) two OH-terminated SAMs for a bulk salt concentration $c_0 = 100$ mM and different ions obtained by nonlinear PB (data points) compared with the asymptotic Debye-Hückel (DH) pressure from Eq. 2.12 (lines). The notation for different ions is the same as in Fig. 2.4. The insets show the pressure from non-linear PB for small surface separation (dashed lines and symbols).

Here, one discerns a crossover from electrostatic repulsion at large separation to attraction at small separations which is caused by ionic depletion and roughly sets in when the PMFs from the two surfaces start to overlap. The pressure between two CH_3-terminated SAMs shows a maximum at approximately 1 nm separation, which is highest for NaI. I^- thus acts as the least destabilizing halide ion with respect to aggregation of hydrophobic solutes.

2.3.3. Hofmeister Ordering according to Interfacial Tension, Surface Charge and Coagulation Kinetics

Fig. 2.6A1 and A2 show the surface tension increment $\Delta\gamma$ as a function of bulk salt concentration c_0 for the nonpolar and polar neutral surfaces calculated from Eq. 2.6. Note that $\Delta\gamma$ mixes short-ranged ionic adsorption/depletion effects with long-ranged electrostatic interactions within the double layer in a not easily separable fashion. The tension increment is positive for all ions, meaning that the repulsive component of the PMFs dominates for all ion pairs. Experimentally, 1M NaCl increases the interfacial tension at the dodecane/water interface by 1.45 mN/m [122] which is close to the calculated surface tension increment of 1.34 mN/m at the CH_3-terminated SAM displayed in Fig. 2.6A1. In fact, the results for the hydrophobic surface are quite similar to recent results for the air/water interface using the same ionic force fields [66]: $\Delta\gamma$ increases in the order $I^- < Cl^- < F^-$, the direct HS. As would be expected already on basis of the ionic PMFs, the ordering is reversed at the polar surface, $\Delta\gamma$ increases according to $F^- < Cl^- < I^-$ in Fig. 2.6A2, the reversed HS. Although experimental data is available for the dodecanol/water interface [123], no direct comparison is possible with our data on the polar surface since the dodecanol surface is much less polar than our completely hydroxylated SAM surface. Note that the surface tension increment of KI in the experimental studies was found to be negative at the dodecane/water interface and positive at the air/water interface [122]. This stands in contrast to our findings in Fig. 2.6A1 but is also not easily reconciled with the standard classification of iodide as a fairly strong denaturant and stabilizer against precipitation. Possible explanations for the negative interfacial tension increment of KI at the dodecane/water interface involve oxidation of I^- to I_2 due to traces of oxygen in the solution and further reaction to I_3^-. Both I_2 and I_3^- are expected to show different degrees of interfacial activities at the air/water, the dodecane/water and the dodecanol/water interfaces. This is a complication that is absent for the other ions as well as for bulk precipitation or denaturation studies of iodide solutions.

According to the Setschenow equation, the protein concentration of maximum solubility, c_{sol}, upon addition of salt is given by

$$\log[c_{\mathrm{sol}}(c_0)/c_{\mathrm{sol}}(0)] = -k_s c_0. \tag{2.18}$$

The salting out constant k_s is, via the heuristic expression $k_s = \zeta A \Delta\gamma$, assumed proportional to the solvent accessible area of the solute A, the fraction of hydrophobic surface patches ζ and the interfacial tension increment $\Delta\gamma$, for which typically the value of the air-water interfacial tension is used [16, 18]. Fig. 2.6A3 shows $\Delta\gamma$ for a negative hydrophobic surface of charge $\sigma_{\mathrm{surf}} = -0.1$ e/nm^2. Based on the Setschenow equation, for

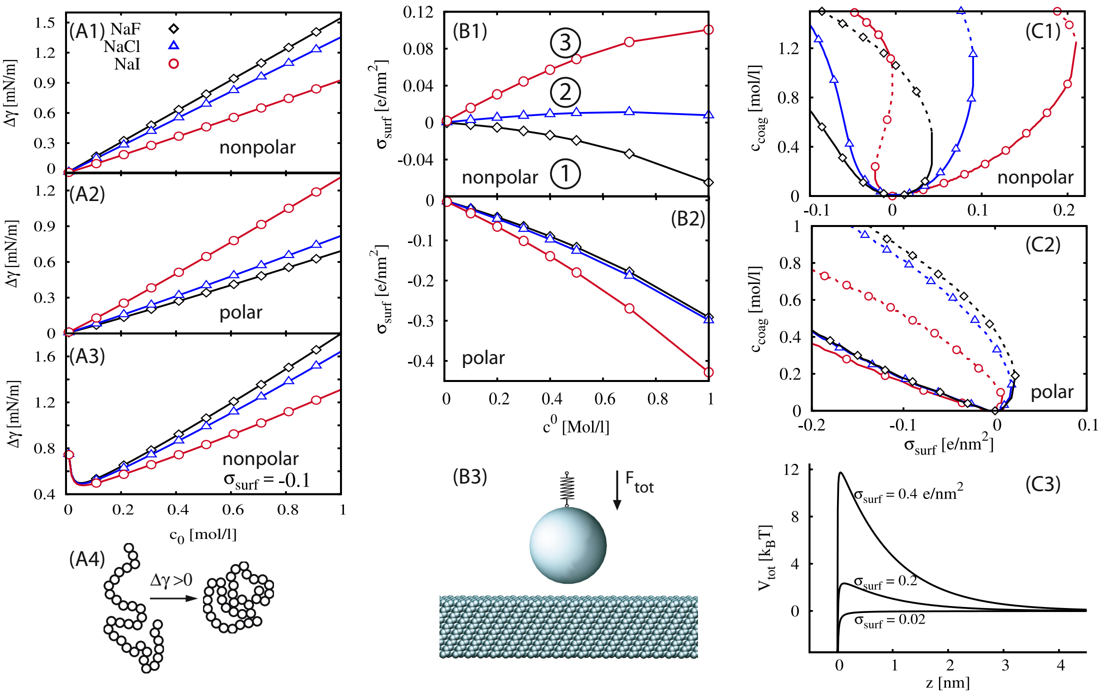

Figure 2.6.: (A) Surface tension increment $\Delta\gamma$ from thermodynamic integration Eq. 2.6 as function of bulk salt concentration c_0 for different ions at the (A1) neutral hydrophobic SAM, (A2) neutral hydrophilic SAM, and (A3) hydrophobic SAM with surface charge $\sigma_{\text{surf}} = -0.1\text{e}/\text{nm}^2$. (A4) Schematics of protein folding driven by a positive $\Delta\gamma$. (B) Lines in the surface charge σ_{surf} and salt concentration c_0 plane on which the DH potential vanishes, $\Phi_{\text{DH}} = 0$, at the (B1) CH_3-terminated SAM and (B2) OH-terminated SAM. The encircled numbers in B1 denote surface charges for which the salt-dependent DH potentials for all ions are presented in Fig. 2.7. (B3) Schematic experimental setup for measurements of long-range forces between two surfaces, indicative of the DH potential Φ_{DH}. (C) Critical coagulation concentration c_{coag} for (C1) two hydrophobic and (C2) two hydrophilic spherical particles. Solid and broken lines distinguish between coagulation and restabilization, respectively. (C3) Total interaction potential V_{tot} between two spherical hydrophobic particles of radius 1nm consisting of electrostatic double layer repulsion and van-der-Waals attraction in a 100 mM NaI solution for different values of the bare surface charge σ_{surf}. At $\sigma_{\text{surf}} = 0.02\text{e}/\text{nm}^2$ the barrier disappears, defining a coagulation instability.

small c_0 salting-in of hydrophobic solutes is predicted as $\Delta\gamma$ decreases with increasing salt concentration, while for large salt concentrations $\Delta\gamma$ increases linearly with c_0 indicative of salting-out behavior, in agreement with experimental trends [18]. The schematic drawing in Fig. 2.6A4 symbolizes that a positive surface tension increment, $\Delta\gamma > 0$, which tends to precipitate proteins (salting-out), at the same time stabilizes proteins against denaturing.

Complementary information is obtained from the DH potential Φ_{DH}. Fig. 2.6B1 and 2.6B2 show in the plane spanned by the bare surface charge σ_{surf} and salt concentration c_0 lines on which $\Phi_{\text{DH}} = 0$. On these lines, the specific ion adsorption exactly cancels the bare surface charge and thus the long-ranged interaction between two such surfaces vanishes. Such forces have been measured recently using an atomic-force microscope, where cationic specificity between a planar surface and a spherical particle was considered [118], see Fig. 2.6B3, where the experimental setup is schematically depicted.

To help unravel the entire information contained in Fig. 2.6B1, which shows results for a hydrophobic surface, we start discussing a negative surface with surface charge $\sigma_{\text{surf}} = -0.08$ e/nm^2 at the bottom, indicated by the encircled 1. For such a negative surface the magnitude of the surface potential $|\Phi_{\text{DH}}|$, which is plotted in Fig. 2.7A, is ordered as $|\Phi_{\text{DH}}(\text{I}^-)| > |\Phi_{\text{DH}}(\text{Cl}^-)| > |\Phi_{\text{DH}}(\text{F}^-)| > 0$. This means that the long-range electrostatic interaction between two hydrophobic surfaces becomes more repulsive as one goes from NaF via NaCl to NaI. This is the direct HS, $\text{I}^- > \text{Cl}^- > \text{F}^-$, denoting stability against precipitation and valid for negative hydrophobic surfaces. As we increase the surface charge (moving up in Fig. 2.6B1) we first approach the line on which $\Phi_{\text{DH}} = 0$ for NaF, equivalent to an instability for NaF. For even higher surface charge or large salt concentrations the line on which $\Phi_{\text{DH}} = 0$ for NaCl is encountered, on which Φ_{DH} for both NaF and NaI are nonzero. This means that F^- and Cl^- have exchanged their position in the HS. To understand this phenomenon better, we consider a surface of charge $\sigma_{\text{surf}} = 0.03\text{e/nm}^2$ as denoted by the encircled 2 in Fig. 2.6B1, for which the salt dependent surface potential magnitudes $|\Phi_{\text{DH}}|$ are shown in Fig. 2.7B.

As a function of salt concentration $|\Phi_{\text{DH}}|$ for NaI reaches zero at a concentration of $c_0 \approx 0.2$ M and at $c_0 \approx 0.39$ M becomes larger than $|\Phi_{\text{DH}}|$ for NaCl. This means that for $c_0 < 0.39$ M the indirect HS is predicted with $0 < |\Phi_{\text{DH}}(\text{I}^-)| < |\Phi_{\text{DH}}(\text{Cl}^-)| < |\Phi_{\text{DH}}(\text{F}^-)|$, while for $c_0 > 0.39$ M partial reversal with the ordering $0 < |\Phi_{\text{DH}}(\text{Cl}^-)| < |\Phi_{\text{DH}}(\text{I}^-)| < |\Phi_{\text{DH}}(\text{F}^-)|$ is predicted. In particular the reversal between iodide and chloride with increasing salt concentration is noteworthy, as it was recently observed experimentally for the cationic protein Lysozyme [69]. In comparing the experimental finding with the behavior depicted in Fig. 2.7B we implicitly assume that the precipitation of Lysozyme is driven by the interaction between hydrophobic patches, which seems plausible.

If we now assume a strongly positively charged hydrophobic surface, denoted by the encircled 3 in Fig. 2.6B1, we observe the indirect HS for all salt concentrations,

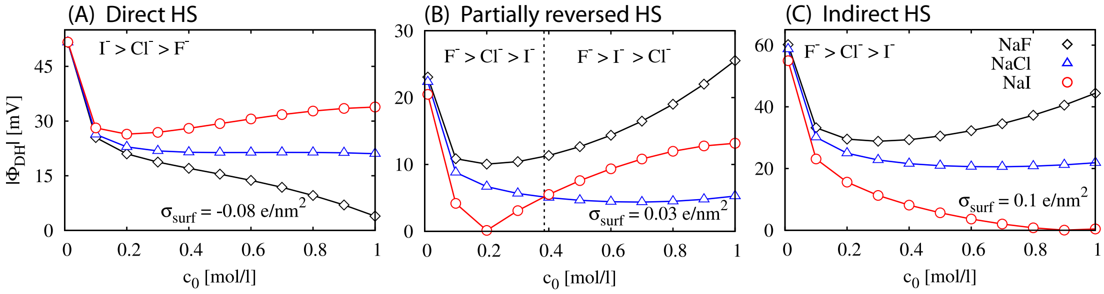

Figure 2.7.: Magnitude of the DH potential $|\Phi_{\text{DH}}|$ as a function of salt concentration at the nonpolar CH_3-SAM for three different values of the bare surface charge σ_{surf}, corresponding to encircled numbers in Fig. 2.6B1.

$0 < |\Phi_{\mathrm{DH}}(\mathrm{I}^-)| < |\Phi_{\mathrm{DH}}(\mathrm{Cl}^-)| < |\Phi_{\mathrm{DH}}(\mathrm{F}^-)|$, as shown in Fig. 2.7C and indeed observed with typical cationic peptides [21, 69] and colloids [74].

In contrast, the stability of the hydrophilic SAM in Fig. 2.6B2 follows an inverse HS only for large negative external surface charge densities. For neutral or positive (and for large salt concentrations slightly negative) external surface charge densities the direct series is predicted, in agreement with experimental results for colloidal hydrophilic systems [74]. Again, various partial reversals between the ions are predicted for intermediate surface charges and salt concentrations. This discussion shows that one expects extended regions in the plane spanned by the salt concentration c_0 and the bare surface charge σ_{surf} where the effective surface potential Φ_{DH} for NaCl is close to zero, while Φ_{DH} is non-zero but has different signs for NaF and NaI. Such regions would be classified as obeying a partially reversed Hofmeister series. This mechanism for partial HS reversion is quite universal and linked to the fact that the repulsion between two equal surfaces depends on the square of the effective surface charge: While the surface potential or the effective surface charge always obeys the direct or reversed Hofmeister series, the interaction between two surfaces displays partial reversal around the ion for which the surface potential vanishes. Note that on both surfaces, we predict HS reversal as a function of salt concentration and as a function of surface charge. By continuity, it also follows that HS reversal takes place when going from polar to nonpolar surfaces and vice versa, we are thus led to the schematic phase diagram depicted in Fig. 2.1. The double HS reversal as function of surface polarity and surface charge is pictorially explained in Fig. 2.8. Note that this mechanism for HS reversal depends on the fact that two surfaces interact with each other and is absent for a single-surface property such as the interfacial tension.

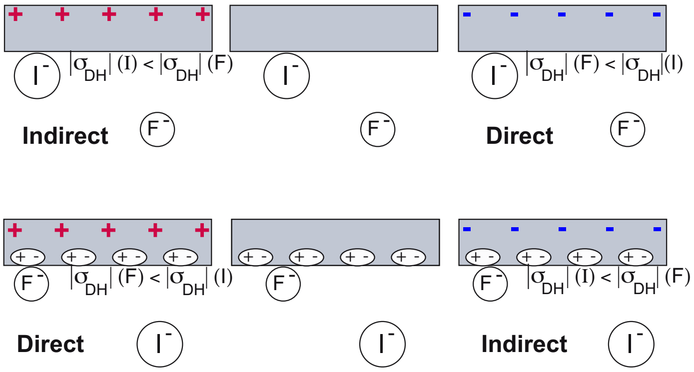

Figure 2.8.: Schematic explanation of the Hofmeister series reversal obtained when changing surface polarity and surface charge. At each surface we show one iodide and one fluoride ion. At the nonpolar surfaces (top row) iodide adsorbs stronger and is thus drawn closer to the surface. At the polar surface (bottom row) the behavior is reversed and fluoride is repelled less strongly than iodide. For the magnitudes of the effective surface charges this means that $|\sigma_{\mathrm{DH}}|(I) > |\sigma_{\mathrm{DH}}|(F)$ for the negative nonpolar and the positive polar surface leading to a stronger long-ranged electrostatic repulsion between surfaces in NaI solutions compared to NaF solutions, corresponding to the direct HS. Conversely, for the positive nonpolar and the negative polar surface we have $|\sigma_{\mathrm{DH}}|(I) < |\sigma_{\mathrm{DH}}|(F)$ and thus the indirect HS.

Note also that our discussion is based on the DH potential Φ_{DH} and thus only valid for the long-ranged part of the interaction between two surfaces. When one considers two surfaces that come into contact, the situation is more complicated as the energetics results from a combination of short-ranged and long-ranged effects.

Fig. 2.6C shows the critical coagulation concentration c_{coag} as a function of σ_{surf} for spherical hydrophobic, C1, and hydrophilic particles, C2, calculated from Eq. 2.17 using the asymptotic results for Φ_{DH}. As illustrated in Fig. 2.6C3, coagulation results from a balance of the strengths of electrostatic repulsion and van-der-Waals attraction and is defined as the salt concentration at which the barrier height vanishes. For negative weakly charged hydrophobic surfaces c_{coag} increases according to the direct HS, $\mathrm{F}^- < \mathrm{Cl}^- < \mathrm{I}^-$, while for positive surface charge the series is reversed, see Fig. 2.6C1. Moreover, the ordering is reversed, if the surface character is changed from hydrophobic to hydrophilic, see Fig. 2.6C2. These findings are in complete agreement with the HS ordering inferred from the DH potential Φ_{DH} in Fig. 6B and the classification as schematically summarized in Fig. 2.1. Most importantly, these findings are in qualitative accordance with recent experiments measuring c_{coag} of charged colloidal particles [74], showing that the combination of charges on the one hand and polar/nonpolar groups on the other hand govern kinetic colloidal Hofmeister effects.

In Fig. 2.6C at high salt concentrations restabilization occurs with the ordering opposite to the instability at low concentration (restabilization lines are denoted by broken lines). Although this high-salt behavior resembles experimental findings for colloidal restabilization [74], care has to be taken when interpreting the theoretical results at large salt concentration since (as we have explained in the Methods section) the usage of the linearized PB equation in deriving the coagulation concentration becomes unreliable.

2.4. Conclusion

MD simulations can at the present level of computing resources not yield the ion specific forces between proteins including surface groups, water and ions on a fully atomistic level. Therefore, we resort to a two-scale approach in which i) single ions are treated with explicit water at atomistically resolved planar surfaces, and ii) the resulting PMFs are imported into coarse-grained PB theory which includes interactions between surface charges and ions at finite concentration on a mean-field level. The advantage of the current approach is that surface polarity, and in specific the crossover from hydrophobic to hydrophilic surfaces, is treated realistically and the changes of ion hydration and surface hydration as an ion approaches the surface are included in the PMF. While the reversal of the Hofmeister ordering of ion adsorption on polar and nonpolar surfaces is already apparent from the PMFs, the additional HS reversal with respect to the surface charge is a collective effect which only comes out from the full PB treatment. The resulting schematic Hofmeister phase diagram in Fig. 2.1 as a function of surface polarity and charge exhibits 4 disconnected Hofmeister regimes and matches experimental results for colloids [74]. One important feature of the diagram is that partial series reversal is a very prominent feature and is expected for surfaces of intermediate polarity or intermediate charge as often encountered in biology [21, 69]. These partial series reversions thus do not reflect an inconsistency of our current understanding of Hofmeister effects, but rather are a direct consequence of the competition of charge and solvation effects: Whereas the tension of a single surface and the effective surface charge (or, equivalently, the electrostatic potential far away from the surface) always obey a fully ordered (direct or reversed) Hofmeister series, the far-distance interaction between two surfaces is proportional to the product of the surface potentials and thus exhibits partial reversal around the ion for which the surface potential changes sign.

In the following we point out directions of further research:

We considered only two surface types, namely a hydrophobic surface formed by a CH_3-terminated SAM and a hydrophilic surface formed by a fully CH_2OH-terminated SAM. These are somewhat extreme and drastically idealized cases. Typical protein surfaces consist of a mixture of polar/nonpolar groups or patches and the immediate question arises whether the influence of polar and nonpolar groups on ions can be considered separately. In fact, the ion specific effects of a large variety of functional groups on oligo-peptides have been found experimentally to be additive [124], meaning that the adsorption of ions on polar and nonpolar surface groups can to first approximation be viewed as the superposition of both separate processes. This in turn opens up attractive possibilities for future modeling of complex heterogeneous surfaces that consist of polar and nonpolar groups and will be discussed in chapter 3.

While hydrophobic surfaces share many properties with the air/water interface and exhibit behavior largely independent of chemical details, for polar groups details matter. The OH group is overall neutral but locally has a relatively high surface charge density, other polar groups of different size and chemical structure span the entire spectrum between the very polar and very nonpolar groups considered by us. It needs to be checked whether surface groups with intermediate surface polarity indeed show intermediate ion specific characteristics. The first step toward a surface of intermediate hydrophilicity is taken in chapter 4 where the Hofmeister order at a COOH-terminated SAM is discussed.

In our two-scale modeling approach we obtain ionic PMFs from simulations of overall neutral surfaces, while a net surface charge is accounted for in the PB approach which treats surface charges as smeared out. This separation is a simplification necessitated by the computational demand of high-precision MD simulations of ions at charged surfaces. In reality surfaces show varying degrees of charge localization around charged groups. Explicit surface charges are discussed in chapter 4 using charged COO^--surface groups as a model system.

The PB level neglects non-electrostatic ion-ion interactions, which might become important at higher salt concentrations. Here, implicit solvent simulations and improved density functional theory that use ion-ion PMFs from explicit-solvent MD will certainly be of use in the future.

Chapter 3

Comparison of Anionic and Cationic Hofmeister Effects

3.1. Introduction

3.1.1. Motivation

Since the discovery of the *Hofmeister series* in 1888 [10] there has been growing interest in ion specific effects. Ion specific effects emerge universally between charged objects immersed in aqueous electrolyte solutions and are therefore relevant to fields ranging from molecular biology to bioengineering. The widespread applicability of the series and the ambiguous origin make the identification of the mechanism and the implementation into a general theory one of the current challenges in interfacial and colloidal science [125].

Traditionally, ions are divided into two classes: kosmotropes and chaotropes. If ions are small, the surrounding water molecules are tightly bound and the ion is called kosmotrope. If ions are large, the hydration shell is weakly bound and the ion is called chaotrope. The discrimination of the two classes depends on the strength of the ion-water interaction compared to the water-water interaction [20]. For almost a century ion specific effects have been attributed to the changes that ions provoke in the hydrogen bonding network of water. In this simplified picture the making and breaking of water structure is central to the Hofmeister series: kosmotropic ions like fluoride salt-out proteins from solutions and stabilize their folded structure while chaotropes like thiocyanate denature folded proteins and give rise to salting-in behavior. However, several recent experiments casted doubt on the central role of water structure [31, 44–46]. Today, there is common agreement that direct ion-macromolecule interactions including partial ion dehydration upon surface binding are largely responsible for ion specificity [31]. Therefore, non uniform ion distributions (accumulation or exclusion) near surfaces are responsible for thermodynamic effects for a very wide range of aqueous processes [47]. Still, the terms kosmotrope, hard, strongly hydrated or chaotrope, soft, weakly hydrated are widely used since this simplified pictures turned out to qualitatively describe numerous specific ion effects [9, 20]. For example, anions and cations can be ranked according to their ability to salt-out small nonpolar solutes like benzene. Salting-out increases as the charge density of the ion increases [16, 99, 100, 126]. This relationship is significant at moderate salt concentration (0.1-1M) and is stronger for anions compared to cations.

Today, the series are getting more and more mixed and the ordering may depend on temperature, salt concentration, pH, buffer etc. [9, 27, 69, 75, 76]. Fig. 3.1 shows a typical Hofmeister ordering of anions and cations based on macroscopic properties like surface tension, solubility of hydrocarbons, protein stability and denaturation [9, 31]. Note that the ordering for cations is defined opposite to Hofmeister's observation [10]: "The strongest precipitation have lithium salts and for the same acids followed with decreasing intensity by sodium, ammonium and magnesium salts." To avoid confusion, we refer to direct order for anions and cations if the order corresponds to the ranking in Fig. 3.1 since this ranking is based on diverse macroscopic properties that turned out to describe a variety of Hofmeister effects [9]. Anions are ordered from left to right from small, most destabilizing, to large, most stabilizing ions, as expected. By contrast, for the cations, it is just the other way around. The reason for this asymmetry will be one of the central topics of this chapter.

Another open question is why ion specific effects are often found to be less pronounced for cations than for anions [31, 127]. For the air-water interface it is suggested that the thermodynamics of transferring cations and anions from bulk to a surface are dominated by different interactions. While for anions the cost of partial dehydration is argued to be the dominant factor for ion-specificity, for the cations no correlation between partial dehydration and specific adsorption is observed [128]. The less influential role of the cations in the field of ion specific effects might be an explanation for the multitude of different cationic series occurring in the literature. The most prominent example is the small lithium ion which is known to switch its position within the ranking depending on its hydration [27].

However, recent experimental studies on the crystallization of lysozyme showed that cations can have an influence as significant as anions, despite the fact that lysozyme is positively charged at neutral pH [129]. These results suggest that cations and anions can interact with proteins leading to specific interactions in both cases. Yet, a systematic study of anions and cations at simple model solid surfaces, which are closely related to biological surfaces and which can contribute microscopic insight into these basic questions, has not been reported so far.

Moreover, as discussed in detail in the previous chapter the Hofmeister order is not universal but depends on the surface charge, the bulk salt concentration and the nature of the surface. Today, the presumably universal Hofmeister ranking makes way for a whole spectrum of direct, altered and reversed series. For example, the cationic and anionic series depend on the sign of the surface charge. On relatively acid oxides like SiO_2 or TiO_2 at low pH the cationic sequence is direct [14, 73, 130] but indirect on relatively basic oxides like Al_2O_3 at high pH [131]. Similarly, the solubility of negatively charged

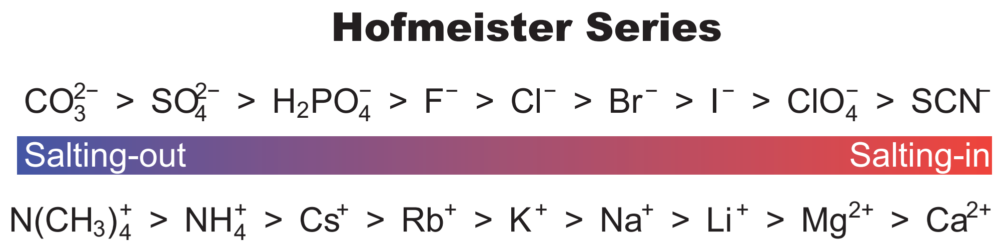

Figure 3.1.: Typical ordering of anions and cations in a Hofmeister series based on macroscopic properties like surface tension, solubility of hydrocarbons, protein stability and denaturation [9, 31]. We refer to this order as direct in the following.

proteins follows the direct order [132, 133] while the solubility and crystallization of positively charged lysozyme follows the reversed order [21, 59, 69]. Moreover, the reversed cationic order is observed for the adsorption of lysozyme to solid silica surfaces [134]. In colloidal systems the order is reversed for monovalent cations and anions when the sign of the surface charge is changed from negative to positive for hydrophobic colloids [71, 72, 74]. In contrast, the cationic order on the hydrophilic surface is not reversed when changing the sign of the surface charge [74]. Therefore, negatively charged hydrophobic and hydrophilic colloids show the same cationic sequence while reversal is observed when going from positively charged hydrophobic to hydrophilic colloids. This contrasts the double reversal observed for anions (chapter 2).

3.1.2. Outline

In this chapter we extend the approach of chapter 2 to more complex systems consisting of heterogeneous polar and nonpolar surface groups. Single ion interfacial potentials of mean force (PMFs) are obtained using all atom explicit water molecular dynamics (MD) simulations for halide and alkali ions at hydrophobic CH_3-terminated self-assembled monolayers (SAMs) and a hydrophilic OH-terminated SAMs. Importing these PMFs into extended Poisson-Boltzmann (PB) theory (two-step approach described in detail in chapter 2) allows to calculate ionic density profiles, interfacial increments as well as complete Hofmeister phase diagrams based on long-ranged stabilizing forces between solutes in electrolyte solutions.

We use two different approaches to model surfaces of varying hydrophobicity. These models for heterogeneous surfaces allow to extend our approach to more realistic surfaces consisting of hydrophobic and hydrophilic surface patches similar to proteins [47]. The generalized PB approach is validated by explicit MD simulations at salt concentration of $c_0 = 1$M yielding satisfactory agreement for the density profiles. Moreover, our results at hydrophobic and hydrophilic surfaces quantitatively match experimental surface tension increments for 1 molar sodium halides and alkali chlorides. Larger ions show less repulsion from the hydrophobic surface and thus a weaker increase of interfacial tension. This transpires when comparing NaI to NaF or NaCl to CsCl (Fig. 3.7) in agreement with previous simulation results [66, 135, 136]. Surprisingly, lithium is less repelled from the hydrophobic surface than sodium. We demonstrate that this alteration in the Hofmeister series occurs due to the strong binding of the first solvation shell of water molecules, which makes Li^+ appear larger.

At the hydrophobic surface the Hofmeister cation phase diagram resembles that of anions. We obtain the direct order on negatively charged surfaces. Reversal takes place when changing the sign of the surface charge from negative to positive in agreement with experimental results [21, 71–74, 134]. The asymmetry in stabilizing efficiency and ion size between cations and anions obtained on negatively charged surfaces (shown in Fig. 3.2) is explained by the preferred adsorption of large ions in combination with the opposite charge of anions and cations.

The adsorption at the hydrophilic surface shows a complex interplay of ion and surface hydration, surface geometry and ion size which does not fit into a simple adsorption/repulsion behavior scheme. The resulting Hofmeister order is in agreement with experimental trends for colloids [74]. As a consequence of the complex cation-surface interaction at the hydrophilic surface, we obtain a multiplicity of alterations depending on surface charge and salt concentration. There, small differences between different cations lead to a weaker pronounced order compared to the anions.

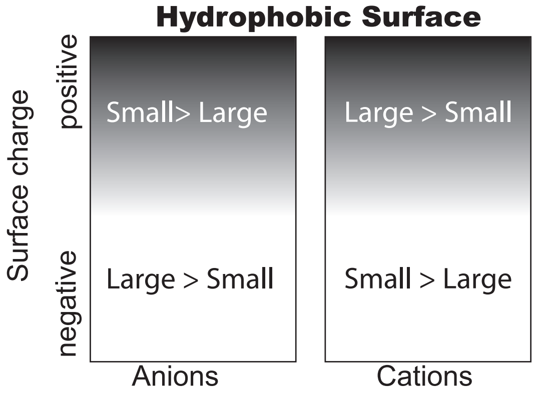

Figure 3.2.: Schematic Hofmeister order according to effectiveness in stabilizing negatively or positively charged solutes related to the size of the ions based on experimental results [21, 71–74, 134]. On negatively charged surfaces the direct order (white region) is observed and reversal (black region) takes place when changing the sign of the surface charge. For intermediate values of the surface charge partial alterations occur (gray region). Anions and cations display an asymmetry in the relation between ion size (small/large) and and effectiveness in stabilization.

3.2. Methods

3.2.1. Simulation Details

The two-scale modeling approach used here has been described in detail in chapter 2. The force field parameters used for anions and cations were previously optimized to reproduce thermodynamic solvation properties [68]. From the three different cation parameter sets given in [68] we have used parameter set 2 for all cations in our calculations. This parameter set yields accurate ion pairing properties as judged by comparison with experimental osmotic coefficient data [109]. All force field parameters for the ions and surfaces are listed in the appendix A (table A.5). A single ion is placed into the water phase and its PMF is calculated by umbrella sampling [112] with a window spacing of 0.025 nm and 3 ns simulation time discarding the first 1 ns using a time step of 2 fs and the weighted histogram analysis method [113]. To ensure converged PMFs the equilibration at the hydrophobic and hydrophilic surface is analyzed in detail (appendix A, Fig. A.1).

In every simulation the ion-oxygen radial distribution function (RDF) $g_{\mathrm{I}W}(r)$ is obtained. The coordination number is then calculated from

$$n_C(r) = \int_0^r 4\pi r^2 g_{\mathrm{I}W}(r')\mathrm{d}r'. \tag{3.1}$$

The average number of water molecules in the first hydration shell of the ions is denoted as $n^1 = n_C(r^1)$, where r^1 is the position of the first minimum of the RDF and is assumed to be independent of the ion-surface separation. The density profile for 1M NaCl at the hydrophobic and hydrophilic SAM surfaces is obtained from a 100 ns simulations. All simulations are performed with the Gromacs 3.3.1 simulation package [114].

3.2.2. Poisson-Boltzmann Approach for Heterogeneous Surfaces

Typical protein surfaces consist of a mixture of polar/nonpolar groups or patches. Generally, the surface of a protein contains 1/3 hydrophobic and 2/3 hydrophilic patches, while the interior of a protein contains only about 1/3 hydrophilic groups associated with the backbone [47]. Since the ion specific effects of a large variety of functional groups on oligo-peptides have been found experimentally to be additive, the adsorption of ions on polar and nonpolar surface groups can to first approximation be viewed as the superposition of both separate processes [124].

In the following we describe two approaches which allow to model heterogeneous surfaces consisting of hydrophobic and hydrophilic surface patches. The two approaches are illustrated in Fig. 3.3.

The first ansatz, which we refer to as nano-scale approach, assumes that the ion interacts with the superimposed potential of hydrophobic and hydrophilic surface groups. In this case the modified PB equation for a planar surface reads

$$\epsilon\epsilon_0 \frac{d^2}{dz^2}\Phi(z) = -\sum_i q_i c_0 e^{-\left(\xi V_i^{\mathrm{phob}}(z)+(1-\xi)V_i^{\mathrm{phil}}(z)+q_i\Phi(z)\right)/k_BT}. \tag{3.2}$$

Here, z is the distance perpendicular to the surface, q_i is the charge of ions of type i, c_0 is the bulk salt concentration, ϵ_0 is the dielectric constant of vacuum, ϵ is the relative dielectric constant of water, $V_i^{\mathrm{phob}}(z)$ is the PMF at the hydrophobic CH_3-terminated surface as obtained in the MD simulations, $V_i^{\mathrm{phil}}(z)$ is the PMF at the hydrophilic OH-terminated surface, and $\Phi(z)$ is the electrostatic potential.

The second ansatz, which we refer to as meso-scale approach, assumes that each ion

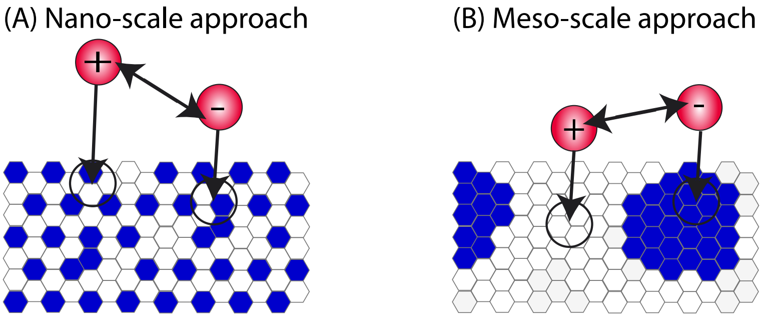

Figure 3.3.: Illustration of the two approaches to model heterogeneous surfaces consisting of hydrophobic and hydrophilic surface patches. (A) Nano-scale approach: ion interacts with the superimposed potential of hydrophobic and hydrophilic surface groups. (B) Meso-scale approach: Ion interacts either with a hydrophobic or a hydrophilic surface patches. The ionic densities are additive, but the coulomb interactions lead to a non-linear coupling.

interacts either with a hydrophobic or a hydrophilic surface group. The ionic densities are assumed to be additive, but the long ranged coulomb interactions lead to a non-linear coupling. In this case the PB equation reads

$$\epsilon\epsilon_0 \frac{d^2}{dz^2}\Phi(z) = -\sum_i q_i c_0 \xi e^{-\left(V_i^{\text{phob}}(z)+q_i\Phi(z)\right)/k_BT} - \sum_i q_i c_0 (1-\xi) e^{-\left(V_i^{\text{phil}}(z)+q_i\Phi(z)\right)/k_BT}. \tag{3.3}$$

The parameter ξ corresponds to surface hydrophobicity, i.e. the fraction of nonpolar CH_3-groups compared to polar OH-groups where $\xi = 1$ corresponds to a pure hydrophobic surface and $\xi = 0$ to a hydrophilic surface. The PMFs are fitted by heuristic fit functions which are given explicitly in the appendix A (table A.2). Eq. 3.2 and Eq. 3.3 are solved numerically on a one dimensional grid with a lattice constant of 1 pm satisfying the boundary conditions (i) $\Phi(z) = 0$ in bulk water ($z \to \infty$) and (ii) $\Phi(z) = \text{const}$ for $z \to -\infty$. An external surface charge is modeled by the modified boundary condition

$$\epsilon\epsilon_0 \frac{d\Phi(z)}{dz}\Big|_{z=0} = -\sigma_{\text{surf}} \tag{3.4}$$

at the surface defined by the mean position of the terminal C and O surface atoms for the hydrophobic and hydrophilic surfaces, respectively.

3.3. Results and Discussion

3.3.1. Cation-surface Interaction Potentials

We study ions at two different surfaces, both formed from SAMs of end-functionalized alkane chains. Fig. 3.4A, B display the main simulation result, i.e. the cation-surface interaction potential at the hydrophobic CH_3-terminated and the OH-terminated hydrophilic surface. The cation adsorption behavior at the hydrophobic surface is quite similar to the air/water interface [38, 65, 105] and correlates with the ion size similar to the halide anions: The largest cation Cs^+ adsorbs strongest, K^+ is weakly repelled while Na^+ is most strongly repelled. The adsorption behavior of Li^+ is more complex due to the strong hydration. The maximum in the PMF of Li^+ at $z = 0.7$ nm is related to the hydration shell consisting of two water layers (shown in Fig. 3.4C) where stripping off the outer layer provides a repulsive barrier upon approaching the surface. The snapshots in Fig. 3.4D (all taken at the distance $z = 0.75$ nm where the Cs^+ PMF has a minimum) show that the first hydration layer of all cations is intact in contrast to the adsorption behavior of large anions like I^- which partially strip off their hydration shell (chapter 2 Fig. 2.2A). This is in line with the observation that the transfer of cations from bulk to the air/water interface is independent of the cost of partial dehydration [128].

In contrast the PMFs at the hydrophilic surface do not show a simple adsorption/repulsion behavior and a ranking of the ions according to their surface affinity on the single ion level is unfeasible. The detailed structure of the ion-surface interaction is related to (i) the size of the ions, (ii) the detailed geometry of the surface and (iii) the water structure

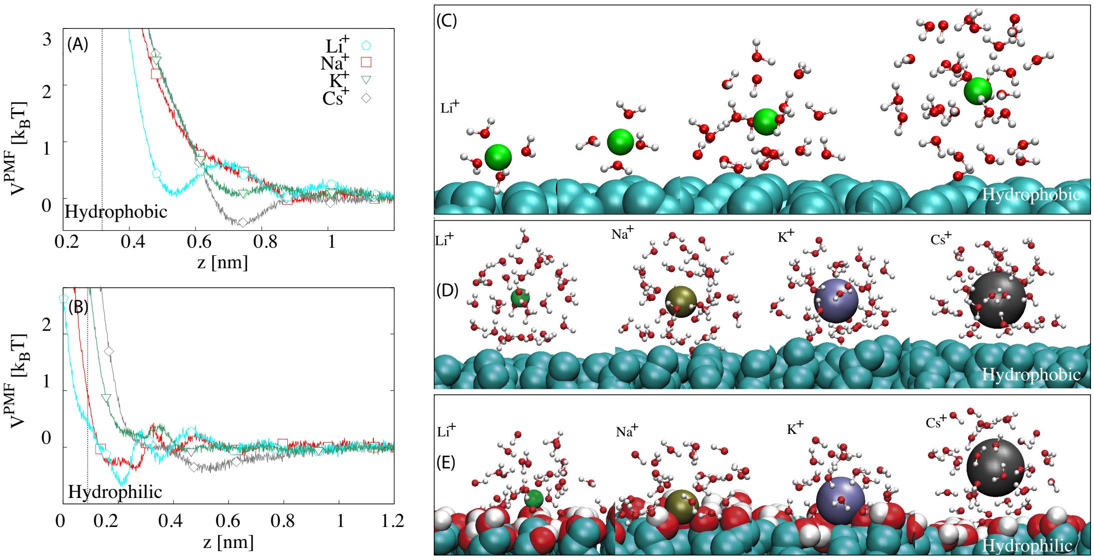

Figure 3.4.: Potentials of mean force (PMFs) for cations at the hydrophobic CH_3-terminated SAM (A) and at the hydrophilic OH-terminated SAM (B). Vertical dotted lines denote the position of the Gibbs dividing surface z_{GDS}. (C) Simulation snapshots of Li^+ at different surface separations: From left to right the ion-surface separation is $z = 0.3$ nm, $z = 0.525$ nm, $z = 0.7$ nm and $z = 0.875$. For small separations the first hydration shell containing 4 water molecules is shown. For larger separations water molecules within 5.5 Å or 6.5 Å of the ion are shown. Simulation snapshots of the cations at the hydrophobic SAM (D) are taken at the position of the minimum in the PMF of Cs^+ at $z = 0.75$ nm. Snapshots of Li^+, Na^+ and K^+ at the hydrophilic SAM (E) are taken at the position of the minimum in the PMF of Li^+ at $z = 0.2$ nm and for Cs^+ at the position of the minimum in the PMF of Cs^+ at $z = 0.55$ nm. Water molecules within 6 Å of the ions are shown. The size of the ions corresponds to their Pauling radii.

at the surface and around the ion. For example, the snapshots of the different cations at the hydrophilic surface reveal that at the minimum ion-surface interaction of Li^+ ($z = 0.2$ nm) the smallest ion has stripped off the water molecules facing the surface and forms one close contact with one oxygen atom of the surface. The larger ions Na^+ and K^+ form contacts with two oxygen atoms whereas contact formation of the larger K^+ ion requires bending of one alkane chain leading to enlarged repulsion. The minimum ion-surface interaction of Cs^+ occurs at larger separations ($z = 0.55$ nm) where the ion has an intact hydration shell.

3.3.2. Hofmeister Ordering according to Surface Tension

Fig. 3.5A, B show the surface tension increment $\Delta\gamma$ as a function of the bulk salt concentration c_0 for the neutral nonpolar and polar surface calculated from Eq. 2.6. The interfacial tension increments exhibit a linear dependence on the salt concentration, in agreement with experimental results at the air/water interface [137]. The slope of the interfacial tension increment at the nonpolar surface correlates with the single ion adsorption displayed in Fig. 3.4A, B. The less repulsive the PMFs are, the smaller the slope of the interfacial tension becomes. The tension increment is positive for all ion pairs, meaning that the repulsion is dominant. Based on the Setschenow equation 2.18 salting-out decreases as the charge density of the ion decreases corresponding to the reversed Hofmeister order: $Na^+ > K^+ > Li^+ > Cs^+$ in agreement with experimental salting-out data of nonpolar solutes [16, 126]. Note, that the Li^+ ion does not fit into this scheme if one considers the bare ionic radius only.

At the hydrophilic surface the oder is altered. Surprisingly, despite the complex ion-surface interaction the tension increment increases linearly with increasing bulk salt concentration. Due to the geometry of the surface the smallest and the largest cations are least repelled while the strongest repulsion and therefore the most efficient salting-out effect is predicted for K^+. Hofmeister ranking with a maximum around the 'neutral cations' K^+ have been observed for the catalytic efficiency of enzymes, where the optimum efficiency depends strongly on the active site of the enzyme [138].

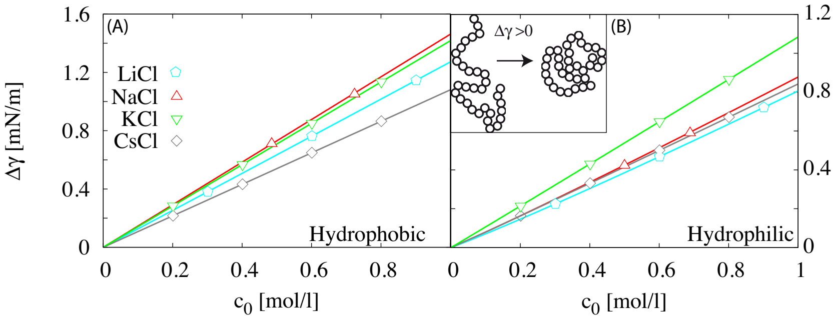

Figure 3.5.: Surface tension increment $\Delta\gamma$ obtained from thermodynamic integration as a function of the bulk salt concentration c_0 for different cations at the hydrophobic (A) and at the hydrophilic surface (B). Schematics of protein folding driven by a positive $\Delta\gamma$ (inset).

Fig. 3.6A, B show the RDF g_{IW} of anions and cations in bulk water. In the order F^-, Cl^-, I^- or Li^+, Na^+, K^+, Cs^+ the first peak in the RDF decreases and broadens meaning that small ions have a tighter bound first hydration shell than larger ions. The unexpected behavior of Li^+ at the nonpolar surface is related to its strongly bound first hydration shell. In order to quantify this further, we calculate the number of water molecules in the first hydration shell n^1 for all cations as a function of the ion-surface separation z from Eq. 3.1. The large cations Na^+, K^+ and Cs^+ partially strip away their hydration shell facing the surface and the coordination number decreases gradually as the cations approach the surface (Fig. 3.6C). In contrast the first hydration shell of the small Li^+ ion remains intact for all separations from the surface. Thus, the PMF of Li^+ corresponds to the interaction of a fully hydrated ion which has an effectively larger radius. For the larger cations the PMF takes partial dehydration into account as the ions approaches the surface. Therefore, the continuum model presented below, which is based on a dielectric sphere corresponding to the bare ionic radius, breaks down for the

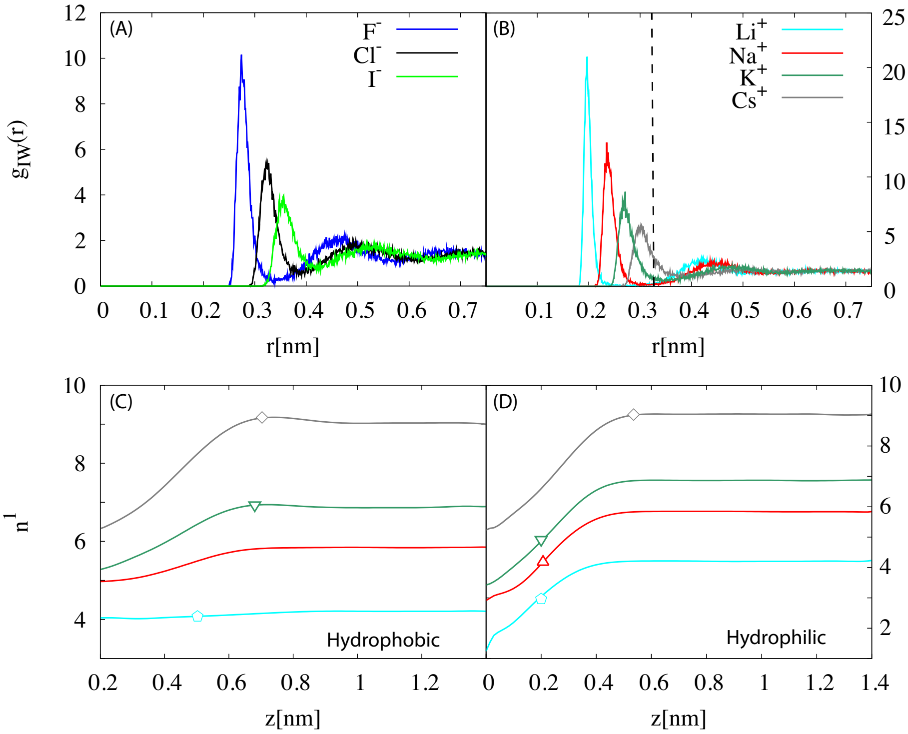

Figure 3.6.: Radial distribution function $g_{IW}(r)$ of the anions F^-, Cl^- and I^- (A) and the cations Li^+, Na^+, K^+ and Cs^+ (B) in bulk. For comparison the dashed line denotes the first maximum in the radial distribution function of Cl^-. Cation coordination number in the first solvation shell n^1 as a function of the distance z from the CH_3-surface (C) and the OH-surface (D). n^1 decreases for Cs^+, K^+, Na^+ as the ions approach the hydrophobic surface indicating reduced ion hydration. In contrast, the hydration shell of Li^+ remains intact. At the hydrophilic surface all ions loose part of their first hydration shell. The open symbols denote the position of the minimum in the ion-surface interaction potential (Fig. 3.4A, B).

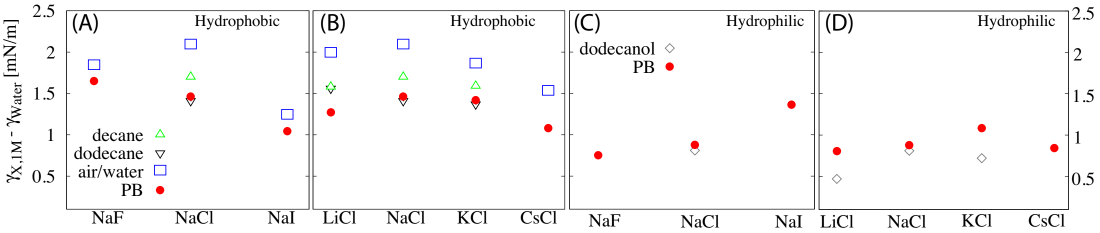

Figure 3.7.: Interfacial tension increment of sodium halide solutions (A) and of alkali chloride solutions (B) at concentration 1M at the hydrophobic CH_3-terminated SAM obtained by Poisson-Boltzmann modeling (filled circles) and at the hydrophilic OH-terminated SAM for sodium halide solutions (C) and alkali chloride solutions (D). Open symbols denote experimental data for decane and dodecane from [122], experimental data for dodecanol from and [123] and experimental data for the air/water interface from [137]. The interfacial tension increment is similar on the different hydrophobic surfaces. Especially the anomaly of Li^+ in the experimental results at the air/electrolyte interface and the decane/electrolyte interface is also predicted for the hydrophobic SAM/electrolyte interface from our modeling results.

cations. This observed behavior of lithium at the hydrophobic SAM is identical to the air/water interface [66] suggesting that the underlying adsorption mechanism is similar. On the other hand, the situation changes on the hydrophilic surface. All ions strip off their hydration shell and bind to the negatively charged oxygen atoms of the surface (Fig. 3.6D).

To quantitatively relate to experiments, we compare in Fig. 3.7 our PB predictions for the interfacial tension increment at $c_0 = 1$ M bulk salt concentration for sodium halide solutions and alkali chloride solutions with experimental data. The results at the hydrophobic surface are compared with experimental data at the decane/-, dodecane/electrolyte interface [122] and the air/water interface [137]. The results at the hydrophilic surface are compared to the dodecanol/electrolyte interface [123]. The overall good agreement between the experimental data and our PB predictions gives confidence in the choice of optimized ionic force fields and confirms that force fields optimized for bulk can be trans-

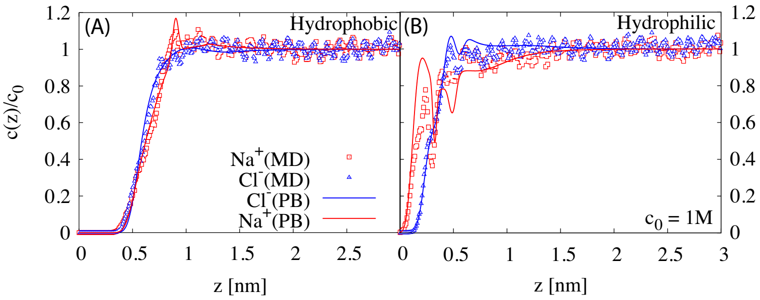

Figure 3.8.: Ion concentration profile of NaCl obtained by PB modeling (solid lines) compared to explicit finite-concentration 100ns MD simulations (open symbols) at the hydrophobic surface (A) and at the hydrophilic surface (B) for 1 M bulk salt concentration. The PB predictions and the results from explicit simulations are in good agreement.

fered to interfacial situations. Even the anomaly of lithium chloride, which has a smaller increment than sodium chloride in the experimental data for the air/water interface and the dodecane water interface, is captured. The shifted values toward a stronger exclusion of cations at the air/water interface compared to a solid surface observed here, has been reported previously [139].

The PB formalism makes some drastic approximations. The neglect of correlation and excluded-volume interaction is known to cause failure of the mean-field approach at high salt concentrations [121]. To validate the results we compare in Fig. 3.8 ion concentration profiles of 1 M NaCl obtained by MD simulations and the PB formalism. The density profiles agree well and validate our two-step approach.

3.3.3. Hydrophobic Solvation at Nonpolar Surfaces

In order to understand the mechanism responsible for the higher surface affinity of the large anions like iodide (chapter 2, Fig. 2.2A), we use a simple theory for the solvation free energy of a hydrophobic cavity. This basic approach is mainly motivated by its successful application to describe the ion specific part of anion adsorption at the air/water interface [66]. Furthermore, this theory is a generalization of the information theory approach, in which the solvation free energy of a hard sphere is proportional to the probability of the spontaneous formation of a cavity matching the hard sphere [140]. For the radii of interest the solvation free energy of SPC/E water can be described by $\mu_{\text{ex}} = \xi 4\pi R^3/3$. The prefactor for SPC/E water is given by $\xi = 0.195$ kJ/MolÅ^3 [66].

The solvation free energy is assumed to be proportional to the fraction of the sphere's volume that partially penetrates the interface. For a sharp interface located at $z = 0$ the solvation free energy in dependence of the distance from the interface z reads [66, 141]

$$V^0_{\text{cav}}(z)/\xi = \begin{cases} -\frac{4\pi}{3}R^3 & z < -R, \\ -\frac{2\pi}{3}R^3 + \pi R^2 z - \frac{\pi}{3}z^3 & -R < z < R, \\ 0 & z > R \end{cases} \tag{3.5}$$

where R is the radius of the cavity. However, the interface is not sharp but both the SAM/water and the cavity/water interfaces are rough. This leads to a smeared out density profile which can be extracted from MD simulations (see chapter 2). The solvation free energy at a broadened interface is given by the convolution

$$V_{\text{cav}}(z) = \int_{-\infty}^{\infty} V^0_{\text{cav}}(z')\rho'(z - z' - \Delta z)/\rho_0 dz' \tag{3.6}$$

where Δz is the shift due to the depletion of water at the hydrophobic surface and the deformation of the interface due to the presence of the ion, $\rho'(z)$ is the derivative of the density profile $\rho'(z) = d\rho(z)/dz$ and ρ_0 is the bulk density of water. Since we are only interested in the penetration of a sphere into the interface, we only take into account the density profile up to the first peak at $z = 0.46$ nm. The water density profile at the hydrophobic surface is shown in Fig. 2.2A in chapter 2. The radii of the cavity are taken from the first maximum in the ion-oxygen RDF shown in Fig. 3.6A.

In Fig. 3.9A the PMF differentials $\Delta V^{\mathrm{PMF}}(x,F) = V^{\mathrm{PMF}}(x) - V^{\mathrm{PMF}}(F)$ for $x =$ Cl, I are shown. Since F$^-$ is most strongly repelled from the hydrophobic surface, $\Delta V^{\mathrm{PMF}}(x,F)$ is more negative for I$^-$ than for Cl$^-$. The corresponding differentials of the theoretical prediction forecast the PMF differences quite well. Considering only the difference between different anions singles out the ion specific part of the ion-surface interaction. Therefore, the ion-specific part of the PMF of the halide anions at the hydrophobic solid/liquid interface is well described by standard hydrophobic solvation theory which is adapted to the interfacial geometry. We conclude from this that (i) the interfacial affinities of anions at our solid/liquid interface are similar to those at the air/water interface since at both surfaces the differences can be explained by the same mechanism and that (ii) polarizability effects only have a minor influence on the interfacial activity of the ions and are not the main driving force for ion specific adsorption.

In Fig. 3.9B the cation PMF differentials $\Delta V^{\mathrm{PMF}}(x,Cs) = V^{\mathrm{PMF}}(x) - V^{\mathrm{PMF}}(Cs)$ for $x =$ Li, Na, K are shown. In the case of the cations the theoretical predictions fail. Using the cavity radii from the position of the first peak in the ion-water radial distribution function shown in Fig. 3.6B, the theory predicts $\Delta V^{\mathrm{PMF}}(x,Cs)$ to be positive. By contrast we observe that the differentials are negative since Cs$^+$ is most strongly repelled at small separations. Moreover, the PMF differentials show additional maxima and minima which cannot be explained by simple solvation theory. The reason for the failure is that the cations are strongly hydrated. The larger effective radius of hydrated ions and the energetic cost of partial dehydration are not included in the theory.

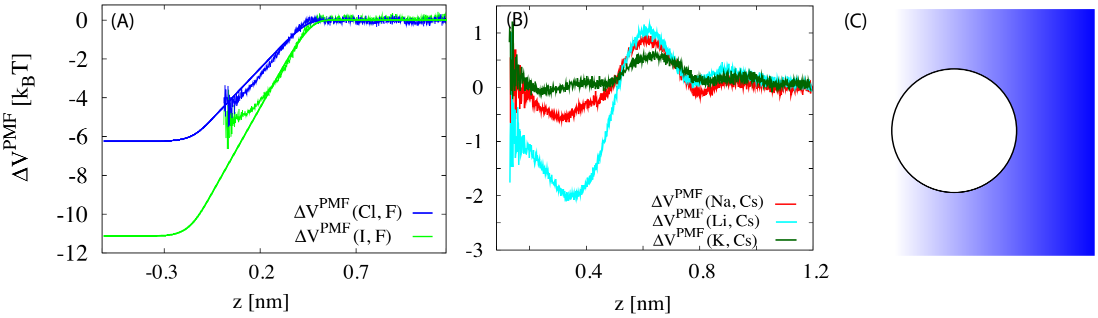

Figure 3.9.: (A) Difference in potential of mean force at the hydrophobic SAM/water interface, $\Delta V^{\mathrm{PMF}}(x,F) = V^{\mathrm{PMF}}(x) - V^{\mathrm{PMF}}(F)$, of chloride and fluoride (blue) and iodide and fluoride (green). The two noisy curves are the differences obtained from the MD simulations. The smooth curves are the differences according to the hydrophobic solvation theory. The cavity radii are taken from the position of the first peak in the ion-water radial distribution function shown in Fig. 3.6, R_F= 0.274 nm, R_{Cl}= 0.325 nm, R_I= 0.356 nm and $\Delta z = 0.35$ nm for Cl$^-$ and $\Delta z = 0.4$ nm for I$^-$. (B) Difference in potential of mean force at the hydrophobic SAM/water interface, $\Delta V^{\mathrm{PMF}}(x,Cs) = V^{\mathrm{PMF}}(x) - V^{\mathrm{PMF}}(Cs)$, of lithium and cesium (light blue), sodium and cesium (red) and potassium and cesium (green). (C) Schematic representation of the solvation of a hydrophobic sphere which permeates an interface: Air (white), water (blue) and cavity (sphere).

3.3.4. Complete Hofmeister Phase Diagram for Anions

Fig. 3.10A, B show the complete Hofmeister phase diagrams for the anions at the hydrophilic and the hydrophobic surface based on the magnitude of the effective surface charge. For each point in the parameter space of external surface charge and bulk salt concentration the PB equation is solved numerically, yielding the electrostatic potential and via Eq. 2.9 and Eq. 2.10 the effective surface charge.

The phase diagrams show four disconnected regions in which the ions are ranked according to their effectiveness in stabilizing hydrophobic or hydrophilic solutes against precipitation according to the magnitude of effective charge σ_{DH}. Short-ranged forces, which are dominant at distances smaller than the ion-surface interaction range, are not included. These short-ranged effects are important for the equilibrium configuration and will be discussed in chapter 5.

Fig. 3.10C shows the complete Hofmeister phase diagram for surfaces of varying surface charge σ_{surf} and surface hydrophilicity ξ for constant bulk salt concentration $c_0 = 200$ mM using the nano-scale approach (Eq. 3.2). The ordering is in perfect agreement with recent experimental classification of colloids and proteins [21, 69, 71, 72, 74]. Furthermore, it matches the schematic diagram in chapter 2 (Fig. 2.1). The phase diagram shows direct (white) and reversed (black) order as well as 4 different alterations. The phase diagram is completely asymmetric due to the double reversal of the anion sequence when changing the sign of the surface charge or the surface hydrophobicity. For three ions the complete spectrum of $3! = 6$ possible series is only obtained when heterogeneous surfaces consisting of hydrophobic and hydrophilic patches are considered.

The reversal of the sequence in dependence of the surface hydrophobicity is a direct consequence of the different surface affinities of the anions at the hydrophobic and the hydrophilic surface. However, this reversal occurs only at large OH-surface concentrations ($\xi < 0.01$). The reversal of the ordering when changing the sign of the surface charge originates from the compensation of the external charge and specific ion adsorption. This reversal is directly related to the surface affinity of the ions: Strongly adsorbing anions like iodide increase a negative surface charge further and lead therefore to the highest stabilization. In contrast, at positively charged surfaces strongly adsorbing anions lead to the most efficient charge compensation and therefore to the weakest stabilization.

Fig. 3.10D shows the complete Hofmeister phase diagram for heterogeneous surfaces using the meso-scale approach (Eq. 3.3). The results from the two models, where the ion is assumed to interact either with a superimposed potential of hydrophobic and hydrophilic surface groups (nano-scale approach) or where the ion is assumed to interact either with a hydrophobic or a hydrophilic surface group (meso-scale approach) are very similar.

In the following we will focus on the nano-scale approach. This choice is justified if the hydrophobic and hydrophilic surface patches are well mixed.

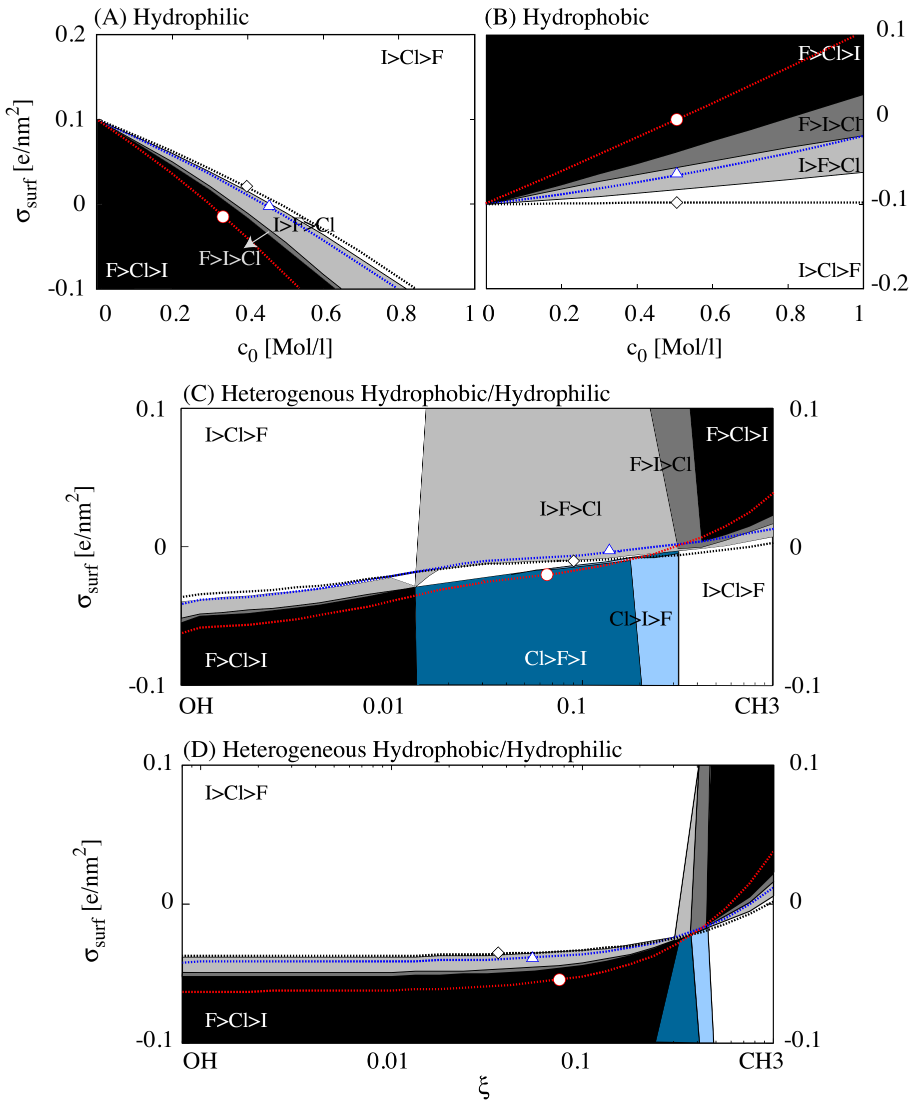

Figure 3.10.: Hofmeister phase diagrams for anions at the hydrophilic OH-terminated SAM (A) and at the hydrophobic CH_3-terminated SAM (B) in dependence of the external surface charge σ_{surf} and the bulk salt concentration c_0 with Na^+ as counterion. (C) Hofmeister phase diagram for heterogeneous hydrophobic/hydrophilic surfaces according to the nano-scale approach (Eq. 3.2) in dependence of σ_{surf} and the surface hydrophobicity ξ for constant bulk salt concentration $c_0 = 200$ mM. (D) Hofmeister phase diagram for heterogeneous hydrophobic/hydrophilic surfaces according to the meso-scale (Eq. 3.3). Colored areas denote regions featuring direct order (white), reversed order (black) and four different alterations. The ordering of the ions corresponds to their efficiency in stabilizing solutes against precipitation based on the magnitude of effective surface charge $|\sigma_{\mathrm{DH}}|$. The dashed lines are the instability lines for NaI (red), NaCl (blue) and NaF (black) on which the long range repulsion vanishes since the bare surface charge σ_{surf} is exactly canceled by specific ion adsorption ($\sigma_{\mathrm{DH}} = 0$).

3.3.5. Stabilization in Dependence of Salt Concentration and Surface Charge

We now return to the cations and start the discussion with Cs^+, K^+ and Na^+ to offer a clearer description. Before discussing the full phase diagrams we analyze the relation between the long-ranged forces and the external surface charge and salt concentration. Long-ranged forces between two surfaces are calculated from the Debye Hückel (DH) potential Φ_{DH} (Eq. 2.9) which is at the same time a measure of the effective surface charge (according to Eq. 2.10). Thus, the DH potential allows to predict the effectiveness of different salt solutions in stabilizing solutes against precipitation (Eq. 2.12).

The dependence of Φ_{DH} on the bulk salt concentration is shown in Fig. 3.11A, B for the hydrophobic and the hydrophilic surface. At the hydrophobic surface the increasing surface affinity with increasing size of the cations is clearly recognized: The large Cs^+ ion adsorbs stronger than Cl^- leading to a positive potential while for the smaller cations the potential is negative due to stronger Cl^- adsorption. The surface affinity follows the series: $Cs^+ > K^+ > Na^+$ in agreement with cation adsorption at silica surfaces [118]. However, the effectiveness in stabilization depends only on the magnitude of the effective surface charge since the pressure p is proportional to σ_{DH}^2 (Eq. 2.12). Therefore, the direct Hofmeister series is obtained for the uncharged hydrophobic surface where Cs^+ is

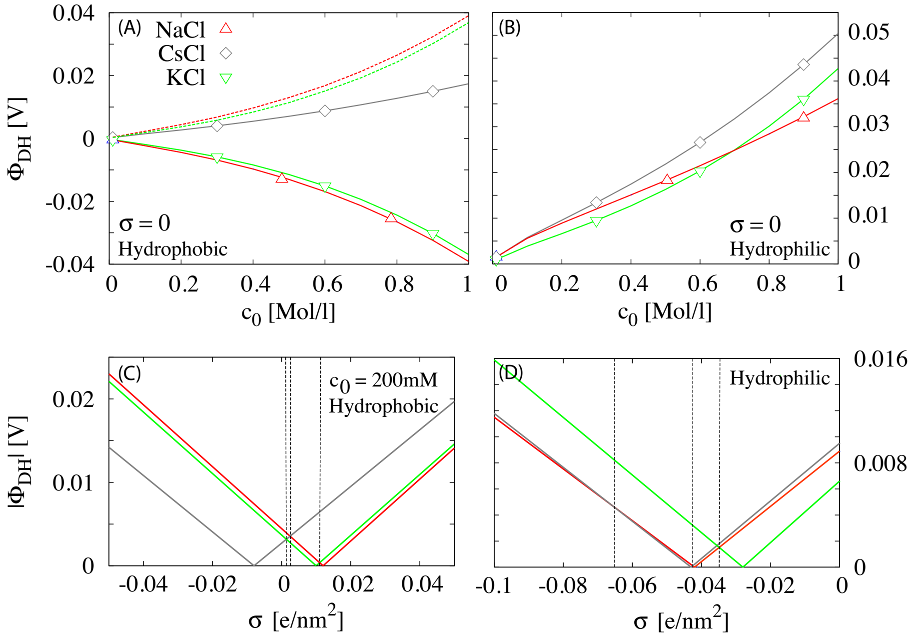

Figure 3.11.: DH potential Φ_{DH} in dependence of the bulk salt concentration c_0 at uncharged hydrophobic surface (A) and at uncharged hydrophilic surface (B). The dashed lines denote the absolute values of the potentials which determine the stabilization efficiency. Absolute value of the DH potential $|\Phi_{\mathrm{DH}}|$ for constant bulk salt concentration $c_0 = 200$ mM in dependence of the external surface charge σ_{surf} at the hydrophobic (C) and the hydrophilic surface (D). Dashed vertical lines mark the points at with two ions exchange their position in the Hofmeister order.

most destabilizing.

In contrast, at the hydrophilic uncharged surface the series is exactly opposite at large salt concentrations. At intermediate salt concentrations the lines for K^+ and Na^+ cross, which means that the two ions exchange their position in the series. This corresponds to a concentration dependent reversal of the Hofmeister order discussed in the previous chapter for anions and confirmed experimentally for the solubility proteins [69, 75].

Fig. 3.11C, D show the dependence of the magnitude of the DH potential $|\Phi_{\mathrm{DH}}|$ on the external charge σ_{surf} for a constant bulk salt concentration $c_0 = 200$ mM. At the hydrophobic surface, Φ_{DH} increases linearly with increasing surface charge. For negative surface charges one obtains the direct order since the strong adsorption of Cs^+ compensates the external charge most efficiently and leads to the highest destabilization. The situation is reversed for positive surface charges where the strong adsorption of Cs^+ leads to the highest effective charge and therewith to the highest stabilization. In between two alterations occur. An alteration of two ions occurs when their DH potentials $|\Phi_{\mathrm{DH}}|$ are equal. In Fig. 3.11C, D this corresponds to the crossing of two lines. At the hydrophobic surface (Fig. 3.11C) the DH potentials Φ_{DH} of different ions in dependence of the external charge do not cross. Therefore, the ion of intermediate adsorption (K^+) can never be most stabilizing (green line of K^+ in Fig. 3.11C is never at the top) and we observe only two different alterations. These partial alterations have to occur at values of the surface charge in between two instability points. Thereby, an instability points is defined as the external charge, the so called critical charge σ_{crit}, for which at a given bulk salt concentration the long range repulsion vanishes since the external charge is exactly canceled by specific adsorption ($\Phi_{\mathrm{DH}} = 0$). At the same time, at this point the effective surface charge changes its sign.

The situation gets more complicated at the hydrophilic surface. Here, we also observe a linear relation between the DH potential and the external surface charge. However, we observe additional alterations due to the intersection point of the DH potentials Φ_{DH} of Cs^+ and Na^+. This results from the complex ion-surface interaction potential at the hydrophilic surface which goes beyond a simple adsorption repulsion behavior. Therefore, at the hydrophilic surface we observe an unexpected sequence of alterations. Moreover, the ordering is not entirely reversed when changing the sign of the surface charge.

3.3.6. Complete Hofmeister Phase Diagram for Cations

Fig. 3.12A, B show the Hofmeister phase diagram in dependence of external charge and bulk salt concentration for the cations at the hydrophilic and the hydrophobic surface. At the hydrophilic surface the phase diagram shows 6 disconnected regions in which the cations are ordered into 4 different series according to their stabilizing ability based on the magnitude of the effective surface charge. The indirect order in which Cs^+ is most stabilizing and Na^+ is most destabilizing occurs only at large salt concentrations or large positive surface charges. The direct order is never observed. The critical charge σ_{crit} is always negative, meaning that the surface affinity of all cations is larger than that of Cl^-. The order according to the critical charge σ_{crit} (K^+) $>$ σ_{crit} (Na^+) $>$ σ_{crit} (Cs^+) $>$ σ_{crit} (Li^+) reflects the minimum adsorption of K^+ at the hydrophilic surface which is

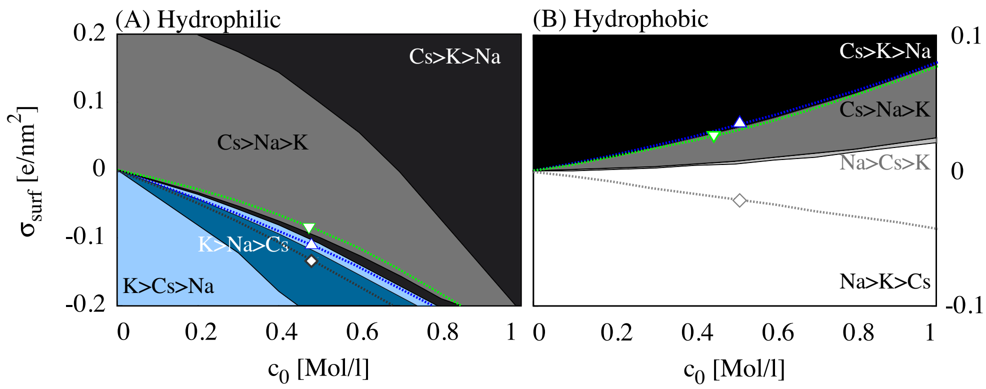

Figure 3.12.: Hofmeister phase diagrams for the cations Cs^+, K^+ and Na^+ at the hydrophilic OH-terminated SAM (A) and at the hydrophobic CH_3-terminated SAM (B) in dependence of the external surface charge σ_{surf} and the bulk salt concentration c_0 with Cl as counterion. Colored areas denote regions featuring direct series (white), reversed series (black) and four different alterations. The ordering of the ions corresponds to their efficiency in stabilizing solutes against precipitation based on the magnitude of effective surface charge $|\sigma_{\text{DH}}|$. The dashed lines are the instability lines for CsCl (gray), NaCl (blue) and KCl (green) on which the long range repulsion vanishes.

also visible in the bell-shape of the surface tension in Fig. 3.7 (data for Li^+ is presented in Fig. 3.13A). Due to the complex ion-surface interaction at the hydrophilic surface a multitude of alterations occur in addition to the previously observed alterations due to charge reversal.

At the hydrophobic surface the phase diagram is similar as for the halide anions: On negatively charged surfaces the series is direct. With increasing surface charge it undergoes two partial alterations related to charge reversal. Finally, at large positive charges one ends up with the inverse order. The critical charge is negative for Cs^+ since the large cation has a higher surface affinity than Cl^- while the critical charge is positive for Na^+ and K^+ due to the larger surface affinity of Cl^-. The order according to the critical charge therefore decreases with increasing size of the cations considering an enlarger size of Li^+ due to its strongly bound first hydration shell: σ_{crit} (Na^+) $\gtrsim$ σ_{crit} (K^+) $>$ σ_{crit} (Li^+) $>$ σ_{crit} (Cs^+) (data for Li^+ is presented in Fig. 3.13B). The difference between Na^+ and K^+ is small in agreement with the weak changes in solubility of e.g. carboxy-hemoglobin when exchanging these ions [132]. Concentration dependent alterations are predicted for intermediate positive surface charges such as for anions.

Fig. 3.13A shows the phase diagrams for LiCl, NaCl, and CsCl at the polar surface and the nonpolar surface. The diagram for the polar surface shows 5 regions of direct order and 4 different alterations. Striking is, that at this surface no alterations in the ordering occur if the sign of the surface charge is changed at large salt concentrations in agreement with experimental results for hydrophilic colloids [74].

In contrast to the non monotonic order for the polar surface, the situation at the hydrophobic surface is as expected (Fig. 3.13B): The cation with the largest surface affinity (Cs^+) is most destabilizing at negatively charged surfaces since it compensates the surface charge most efficiently. With increasing surface charge the most destabilizing ion reaches its instability line on which the external charge is exactly canceled by cation adsorption. With further increasing external charge, charge reversal occurs and the effective surface charge increases again. Eventually, Cs^+ exchanges its position with Li^+. The same situation repeats itself until at large positive charges the series is completely reversed. At the nonpolar surface we do not predict the usual direct Hofmeister series according to Fig. 3.1 due to the unusual behavior of the strongly hydrated Li^+ which has its position on the other side of Na^+ due to its tight hydration shell.

Fig. 3.13C shows the complete Hofmeister phase diagram for surfaces of varying surface

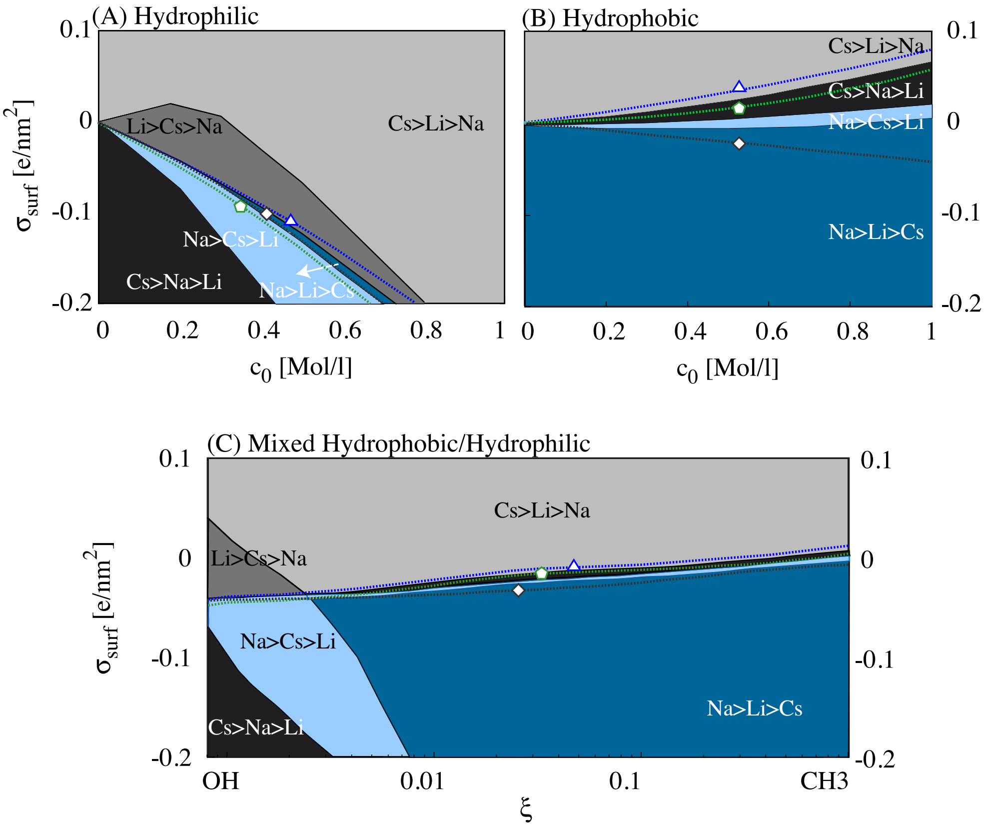

Figure 3.13.: Hofmeister phase diagrams for cations at the hydrophilic OH-terminated SAM (A) and at the hydrophobic CH_3-terminated SAM (B) in dependence of the external surface charge σ_{surf} and the bulk salt concentration c_0 with Cl as counterion. (C) Hofmeister phase diagram for mixed hydrophobic/hydrophilic surfaces in dependence of σ_{surf} and the surface hydrophobicity ξ for constant bulk salt concentration $c_0 = 200\mathrm{mM}$. Colored areas denote regions featuring indirect series (black) and four different alterations. The direct Hofmeister order is not observed due to the unusual behavior of Li^+ at the hydrophobic surface and Cs^+ at the hydrophilic surface. The ordering of the ions corresponds to their efficiency in stabilizing solutes against precipitation based on the magnitude of effective surface charge $|\sigma_{\mathrm{DH}}|$. The dashed lines are the instability lines for CsCl (gray), NaCl (blue) and LiCl (green) on which the long range repulsion vanishes.

charge σ_{surf} and surface hydrophilicity ξ for constant bulk salt concentration $c_0 = 200$ mM. The phase diagram for cations is more complex compared to the completely asymmetric diagram for anions. The reason is that (i) Li^+ remains hydrated for all ion-surface separations and (ii) the complex adsorption behavior of the cations at the polar surface leads to additional alterations in dependence of external charge and salt concentration. For positive surface charges the series is quite robust and no alterations occur when changing the surface hydrophobicity while two partial alterations occur on negatively charges surfaces. Still, these alterations occurs only at large OH-surface concentrations ($\xi < 0.01$).

3.4. Conclusion

Theories for prediction or explaining the Hofmeister series have appeared in the literature. Yet, non of the proposed theoretical frameworks accounts for the full spectrum of direct, reversed and altered sequences. In order to reliably predict macroscopic properties like surface tension, critical coagulation concentration or long-ranged pressure, we need a detailed microscopic understanding of all contributing terms of ions, surface and water. In our approach to gain microscopic understanding we use explicit water MD simulations in combination with PB theory thereby calculating realistic ion-surface potentials. These potentials specifically include (i) direct ion-surface interaction at atomistically resolved surfaces and (ii) hydration effects of ion and surface. The resulting interfacial tension increments agree quantitatively with experimental data, capture the Hofmeister trend, especially the anomaly of lithium, and justify our choice of ionic force fields. In addition the excellent agreement of the PB predictions with finite concentration MD simulations further justifies our approach. The ion specific part of the anion-surface interaction can be explained by interface-adapted hydrophobic solvation theory. The solvation theory breaks down for cations at the hydrophobic surface. The cation-surface interaction is more complex since (i) at the minimal ion-surface interaction all cations are completely hydrated and (ii) large cations strip off a part of their hydration shell upon further approaching the surface. Only Li^+ retains its strongly bound hydration shell.

At the hydrophilic surface, the cation-surface interaction goes beyond a simple adsorption/ repulsion behavior. The ion-surface interaction is dominated by coupled contributions due to (i) the hydration of the ions, (ii) the hydration of the surface and (iii) the geometry of the surface. This leads to a non monotonic, bell-shaped relation between ion size and macroscopic properties like interfacial tension.

The asymmetry in the relation between ion size and effectiveness in destabilization between cations and anions, shown in Fig. 3.2, originates from the preferred adsorption of large ions at hydrophobic surfaces in combination with the opposite charge of anions and cations. Large anions like iodide have a high surface affinity and increase the effective charge on negatively charged surfaces further leading to the highest stabilization. In contrast, large cations like cesium also have a large surface affinity thereby compensating an external charge most efficiently.

The capability of the anions and cations in stabilization is measured by long-ranged forces based on effective charges and their salting-out properties are measured by surface tension increments. On hydrophobic surfaces these macroscopic quantities do not show a significant difference in magnitude when comparing different anions and different cations in agreement with recent experimental measurements [129]. Therefore, the Hofmeister series is not in general weaker for cations compared to anions as often assumed. Still, small differences between ions can occur if the all contributing terms of ions, surface and water are similar or if the opposing contributions cancel out e.g. for sodium and potassium at the hydrophobic surface. On the hydrophilic surface the single cation adsorption behavior is complex. This complexity leads to small differences in macroscopic quantities and to a multiplicity of alterations in dependence of surface charge and bulk salt concentration. With so many specificities even for simple model systems presented here, it is clear that there is not only one parameter for one type of ion that describes its Hofmeister trend under all circumstances. In the following we point out directions of further research:

In our approach we obtain ion-surface interactions from simulations of uncharged surfaces, while a net surface charge is accounted for in the PB approach which treats surface charges as smeared out. In reality surfaces show varying degrees of charge localization around charged groups like negatively charged carboxyl or positively charged amide groups on protein surfaces. Explicit surface charges are discussed in detail in chapter 4.

Predicting salting-out and salting-in effects including denaturation by just knowing the amino acid residue that is exposed to water is the ultimate goal of a general Hofmeister theory. A first step toward identifying the dominant contributions is to create a map of ion-surface interaction with all biological relevant functional groups to predict ion specificity in dependence of salt concentration, surface charge and environment.

The PB level neglects non-electrostatic ion-ion interactions, which might become important at higher salt concentrations. An extended approach that includes ion-ion PMFs from explicit-solvent MD simulations is intended to be used in the future.

Chapter 4

Specific Ion Binding to Charged Surface Groups

4.1. Introduction

4.1.1. Motivation

Understanding and identifying the mechanism by which ions are attracted to or repelled from biological interfaces is highly complex. The mechanism results from balanced ion-surface and ion-water interactions [16]. For simple planar nonpolar surfaces like the air/water interface or the hydrophobic SAM/water interface the strong propensity of large anions like iodide to adsorb can be explained by interfacial adapted hydrophobic solvation theory (chapter 3). Still, a general theory for small cations or for ion-surface interactions at hydrophilic surfaces is missing, due to the complex interdependence of the three contributions of water, surface and ions. But, these interdependencies can be calculated from MD simulations [1, 65, 136]. Attraction or repulsion of anions and cations at biological surfaces is affected by the multitude of ionic interactions with the nonpolar, polar and charged groups on macromolecules [64, 67, 142]. Fig. 4.1 illustrates four different surface regions that influence specific ion interactions: (i) nonpolar surface patches, where ion-surface interactions are similar to the air-water interface, (ii) polar surface patches, where ion-surface affinity can be reversed (iii) evenly distributed charges which influence solubility or precipitation of macromolecules and (iv) localized charged surface groups to which ions can bind specifically.

A core property which has frequently been used to explain Hofmeister effects, and which we have not discussed to far, is the pairing of simple ions with charged groups of macromolecules (or respectively the pairing of ions in water if bulk properties are considered). Explaining a large variety of experimentally observed Hofmeister series, Collins introduced the qualitative rule of matching water affinities, a special case of the general rule

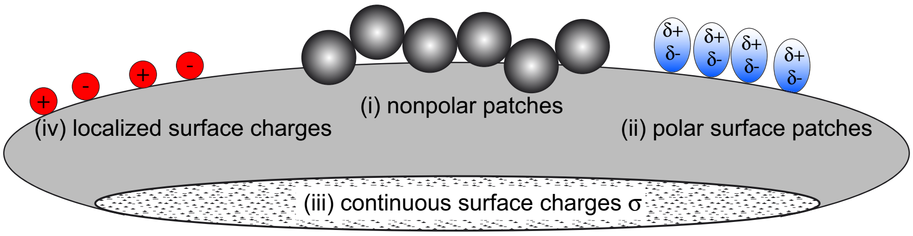

Figure 4.1.: Different surface regions of biological interfaces which influence ion specific interactions: (i) nonpolar and (ii) polar surface patches, (iii) delocalized charges and (iv) localized charged surface groups.

in chemistry 'like seeks like' [20, 48, 49]. According to Collins' rule, the relative affinity of ions depends on the matching of their hydration energies. Assuming that the latter is proportional to the surface charge density of the ions, this translates into matching size of monovalent ions. This empirical law predicts that monovalent anions and cations form stable contact ion pairs (CIPs) if their size matches e.g. lithium and fluoride. In a CIP no solvent molecules intervene between the two ions that are in close contact. In contrast, if the water affinities of two ions mismatch no CIP is formed and the ions are separated by bulk solvent, e.g. lithium and iodide. Although Collin's concept is qualitatively predictive and reasonable if no further information is available, it cannot be more than a rule of thumb since it cannot predict the strength of ion binding. Another drawback of the concept is that solvent shared ion pairs (SIPs) cannot be predicted from it [98]. In a SIP the ion pair is separated by the thickness of only one solvent molecule. The two ions have their own primary solvation shell. These, however, interpenetrate each other.

The interaction of ions with the carboxylate groups of a protein are of special interest since they affect protein association and enzymatic activity [26, 143]. Recent experimental [35, 36] and theoretical studies [98, 144] have addressed pairing of the cations K^+ and Na^+ with carboxylate anions in electrolyte solutions and with carboxylate groups at protein surfaces. The consistent result is a preferred binding of Na^+ over K^+ with carboxylate groups. The estimated difference in the adsorption free energy is 3 to 4 k_BT in favor of Na^+ [144] . The binding strength of cations with carboxylate in water decreases with increasing ion size in the sequence $Na^+ > Li^+ > K^+ > NH_4^+$ [35]. This corresponds, with the exception of Li^+, to the inverse Hofmeister series and matches Collin's rule since the carboxylate group is considered to be hard (i.e. small) [9]. The biological consequences of this behavior are large: Small ions with a high surface charge density like Na^+, Mg^{2+} or Ca^{2+} need to be pumped out the cell despite the energetically high cost. Strong binding of Na^+ to major intracellular anions like phosphates and carboxylates can weaken or even hinder the function of proteins in the cell [49]. Moreover, binding of sodium to carboxylates and backbone carbonyls shifts the equilibrium from the folded to the unfolded state [145]. This might explain why the sodium concentration is more than ten times lower inside than outside cells. The concentration difference across cell membranes creates an electrochemical gradient known as the membrane potential. This membrane potential is maintained by ion pumps, especially the sodium/potassium-

ATPase pumps. Their activity is estimated to account for 20%-40% of the metabolic rate at rest of a typical adult [146]. The large proportion of energy dedicated to maintaining sodium/potassium concentration gradients emphasizes the importance of this function in sustaining life. Moreover, tight control of cell membrane potential is crucial for nerve impulse transmission, muscle contraction and heart function [146, 147].

4.1.2. Outline

So far, scientific work focused on ion pairing of cations with carboxylate anions or the binding of cations to carboxylate groups at surfaces. Here, we expand the existing results and investigate ion pairing at surfaces as function of varying degree of dissociation. The motivation is that the carboxyl groups, present on the surface of many intra- and extracellular proteins, are not necessarily always dissociated. The degree of effectively charged carboxylate groups depends on the pH of the solution and the logarithmic acidic dissociation constant $\mathrm{pK_a}$ of the ionizable group. In addition, the degree of dissociation depends on the surrounding, e.g. the $\mathrm{pK_a}$ shifts to a higher value at a surface compared to bulk [148].

In this chapter, we calculate the ion-surface interaction between both the protonated and the deprotonated form of carboxyl groups. If the carboxyl group is deprotonated, we predict preferred binding of sodium compared to cesium in agreement with previous results. The strong adsorption of sodium gives rise to salting-in behavior and to denaturation of folded proteins. Two different models are proposed to model surface charges: In the first model, charges are evenly distributed over the surface. Such a delocalized, uniform charge distribution can be realized using back-gated semiconductors or self-assembled monolayers [77]. In the second model, the charges are localized. The ion-surface interaction and the surface charge are adapted to the degree of dissociation of ionizable groups. This corresponds to the situation where ionizable groups dissociate as function of pH leading to localized charges. Examples for such localized charges are amino acids like glutamic acid or aspartic acid which are frequently present on protein surfaces.

The Hofmeister phase diagrams based on long-ranged forces between solutes in electrolyte solutions are presented. At low salt concentrations and small surface charges the ranking of anions and cations in a series according to their effectiveness in stabilization is independent of the nature of the charge distribution. This situation is experimentally relevant at low pH. At high salt concentrations and high pH the ranking depends on the nature of the charge distribution since the different ion-surface interaction at uncharged COOH-groups and charged $\mathrm{COO^-}$-groups becomes increasingly important.

4.2. Methods

4.2.1. Simulation Details

In the simulations the surface is a 3.5 × 3.464 $\mathrm{nm^2}$ self-assembled monolayer (SAM) consisting of 56 $\mathrm{C_{20}H_{41}}$ chains with terminal COOH-groups for the uncharged surface.

For the charged surface one COOH-group is replaced by a terminal COO$^-$-group. The chain lattice spacing corresponds to a gold (111) substrate. The lower 6 C-atoms of each chain are restrained by harmonic potentials with spring constant $k = 5 \times 10^5$ kJ/(mol nm^2). A tilt angle of 30° is fixed by the restrained atoms close to experimental values. The simulation box has an extension of 9 nm in the z-direction and is filled with about 2,700 SPC/E water molecules. The SAM is modeled with the GROMOS96 force field [107]. The Lennard Jones parameters and partial charges of the functional groups are listed in the appendix A in table A.5. The force field parameters used for anions and cations are the same as in the previous chapters and are listed in the appendix A in table A.5. The simulations are done at a temperature of 300 K and a pressure of 1 bar maintained by anisotropic pressure coupling (NAP$_\mathrm{z}$T simulation). Periodic boundary conditions are applied, long range Coulomb forces are calculated using the particle-mesh Ewald summation [111] and for the van-der-Waals interactions a cutoff radius of 1.2 nm is used. A single ion is placed into the water phase and its potential of mean force (PMF) is calculated by umbrella sampling [112] with a window spacing of 0.025 nm and 3 ns simulation time discarding the first 1 ns for equilibration. A time step of 2 fs and the weighted histogram analysis method [113] with force constant $k_z = 1000$ kJ/(mol nm^2) is used. For the charged surface we use two additional harmonic potentials with force constant $k_x = k_y = 1000$ kJ/(mol nm^2) to confine the ions within a cylinder above the charged group. All simulations are performed with the Gromacs 3.3.1 simulation package [114]. Even though potassium is of high biological importance, especially in the context of sodium/potassium pumps, we focus on the cations Li$^+$, Na$^+$ and Cs$^+$. The reason is that ion specific effects are clearly visible for these ions at hydrophilic surfaces (chapter 3). By contrast, the differences between Na$^+$ and K$^+$ are tiny since the sizes of these cations are similar. Therefore, we restrict the discussion to cations for which considerable effects are expected. Nevertheless, additional simulations for K$^+$ will be performed in the future. At the charged COO$^-$-terminated surface, umbrella sampling for the small Li$^+$ ion fails to provide a meaningful PMF due to the strong electrostatic interaction. Therefore, the results are excluded from the following discussion. Modified sampling techniques are planed for the future in order to provide ion-surface interaction potentials for small cations as well.

4.2.2. Poisson-Boltzmann Modeling

In the second step of our approach the PMFs obtained by MD simulations are imported into Poisson-Boltzmann theory. To account for surfaces of varying degree of dissociation, we use the nano-scale approach for the ion-surface interaction introduced in chapter 3. Thereby, we assume that the ion interacts with the superimposed potential of uncharged COOH-groups and charged COO$^-$-groups. The PB equation including the ion specific PMFs of anions and cations at the COOH-terminated SAM, $V_i^{\mathrm{COOH}}(z)$, and at the charged COO$^-$-terminated surface, $V_i^{\mathrm{COO^-}}(z)$, then reads

$$\epsilon\epsilon_0 \frac{d^2}{dz^2}\Phi(z) = -\sum_{\pm} q_i c_0 e^{-\left((1-\xi)V_i^{\mathrm{COOH}}(z)+\xi V_i^{\mathrm{COO^-}}(z)+q_i\Phi(z)\right)/k_B T}. \tag{4.1}$$

Here, z is the distance perpendicular to the surface, q_i is the charge of ions of type i, c_0 is the bulk salt concentration, ϵ is the dielectric constant of vacuum, ϵ is the relative dielectric constant of water, and $\Phi(z)$ is the electrostatic potential. The parameter ξ is the degree of dissociation. Thus, ξ corresponds to the fraction of charged COO$^-$-groups on the surface. $\xi = 0$ corresponds to the interaction of the ion with an uncharged COOH-terminated surface and $\xi = 1$ corresponds to the interaction of the ion with a fully charged COO$^-$-surface group. The PMFs obtained by simulations are fitted by heuristic fit functions which are given explicitly in the appendix A (table A.4 and table A.3). Eq. 4.1 is solved numerically on a one dimensional grid with a lattice constant of 1 pm. The potential satisfies the boundary conditions that the electrostatic potential vanishes in bulk ($\Phi(z) = 0$). In addition, we use the constant charge boundary condition

$$\left.\frac{d\Phi}{dz}\right|_{z=0} = -\frac{\sigma_{\text{surf}}}{\epsilon_0\epsilon} \tag{4.2}$$

at the surface. The surface is always defined by the last layer of heavy atoms which form a closed surface. The position is calculated from the mean position of the oxygen atoms.

Models for Surface Charges

In the following we use two different models for the surface charge:

- Delocalized charges: For smeared out charges we set the degree of dissociation to zero ($\xi = 0$). The surface charge σ_{surf} is exclusively included via the constant charge boundary condition.
- Localized charges: For localized charges $\xi \neq 0$ and corresponds to the fraction of dissociated groups. The constant surface charge boundary condition depends on ξ

  $$\frac{d\Phi}{dz} = -\xi\frac{q_{\text{COO}}}{a_0\epsilon_0\epsilon} = -\xi\frac{\sigma_{\text{COO}}}{\epsilon_0\epsilon} \tag{4.3}$$

  where $q_{\text{COO}} = -e$ is the charge of the COO$^-$-surface group, $a_0 = 3.5 \times 3.464\ \text{nm}^2$ is the surface area in the simulation box and $\sigma_{\text{COO}} = -0.0825\text{e/nm}^2$ corresponds to the surface charge density of the COO$^-$-terminated surface.

The Gibbs dividing surface (GDS) is calculated from the requirement that the surface excess for water vanishes $\Gamma_w = \int_{-\infty}^{z_{\text{GDS}}} \rho(z)\text{d}z + \int_{z_{\text{GDS}}}^{\infty} (\rho(z) - \rho_0)\,\text{d}z = 0$. At the uncharged COOH-terminated SAM ($\xi = 0$) $z_{\text{GDS}} = 0.0974$ nm and at the charged COO$^-$-terminated SAM ($\xi = 1$) $z_{\text{GDS}} = 0.21$ nm. The surface tension increment is calculated from the Gibbs adsorption equation

$$\Delta\gamma(c_0, \sigma_{\text{surf}}) = -k_BT\sum_i \int_0^{c_0} \text{d}c_0' \frac{\Gamma_i(c_0, \sigma_{\text{surf}})}{c_0'} + \sigma_{\text{surf}}\Phi(z = 0, c_0, \sigma_{\text{surf}}) \tag{4.4}$$

valid for nearly ideal solutions with the activities replaced by concentrations. $\Gamma_i(c_0, \sigma_{\text{surf}})$ denotes the surface excess of ionic species i for surface charge σ_{surf} and $\Phi(z = 0, c_0, \sigma_{\text{surf}})$

is the surface potential. Note that Eq. 4.4 and Eq. 2.6 are equivalent. However, using Eq. 4.4 is more convenient since it does not involve the integration over different surface charges σ_{surf}.

4.3. Results and Discussion

4.3.1. Ion-surface Interaction Potentials

Fig. 4.2 displays the ionic PMF at the uncharged COOH-terminated SAM and at the charged COO$^-$ SAM. Note that the pictured PMFs at the charge surface do not contain the electrostatic interaction. The ion-surface interaction potential $V_{\text{Coul}}^{\text{PMF}}(z)$ obtained by umbrella sampling includes Coulomb forces calculated by particle-mesh Ewald summation [111]. This leads to a $1/z$-repulsion or attraction for anions or cations at large separations from the surface. The ionic PMFs $V^{\text{PMF}}(z)$ are calculated from the requirement that the PMF vanishes at large ion-surface separations

$$\lim_{z \gg 0} \frac{V^{\text{PMF}}(z)}{k_B T} = \lim_{z \gg 0} \left[\frac{V_{\text{Coul}}^{\text{PMF}}(z)}{k_B T} - \frac{\alpha}{z} \right] = 0. \tag{4.5}$$

The parameter α is fitted to the long-ranged decay of the ion-surface potential $V_{\text{Coul}}^{\text{PMF}}(z)$ at large separations (inset of Fig. 4.2C). The appropriate values are given in the appendix A (table A.4). This approach allows a consistent treatment of the ion-surface interaction within our two-step approach.

The anion-surface affinity increases with decreasing ion size at the polar COOH-terminated SAM (Fig. 4.2A) and follows the reversed Hofmeister order F$^-$ > Cl$^-$ > I$^-$. The small fluoride ion shows a large adsorption minimum of about 6 k$_B$T. The order is exactly opposite compared to the nonpolar CH$_3$-terminated SAM and matches the result at the polar OH-terminated SAM (chapter 2) as expected. Surprisingly, the surface affinity of the cations at the COOH-terminated SAM (Fig. 4.2B) increases with increasing ion size Cs$^+$ > Na$^+$ > Li$^+$ in contrast to the anions. The order is direct as observed at the nonpolar surface in chapter 2. The reason for this unexpected behavior is the preferred interaction of the anions with the hydrogen atom of the COOH-group (Fig. 4.3A, B). Cations mainly interact with the oxygen atoms (Fig. 4.3C, D). This size reversed binding affinity of cations and anions is similar to the work by Garcia-Celma [29]. There, specific binding of anions and cations to lipid membranes is investigated. There, large anions bind more strongly than small anions. By contrast, it is just the other way around for cations. The lipid membrane contains cationic choline headgroups as well as anionic phosphate headgroups. Therefore, a simplified qualitative explanation can be given in terms of Collin's like seeks like rule if the choline is considered to be soft (i.e. large) and phosphate to be hard (i.e. small). Note, that the binding affinities in that work is exactly opposite to our observation. Still, the underlying mechanism of size reversed binding affinity of cations and anions due to different binding sites of anions and cations is the same.

Fig. 4.3A, B show simulation snapshots of F$^-$ and I$^-$ at the COOH-terminated SAM.

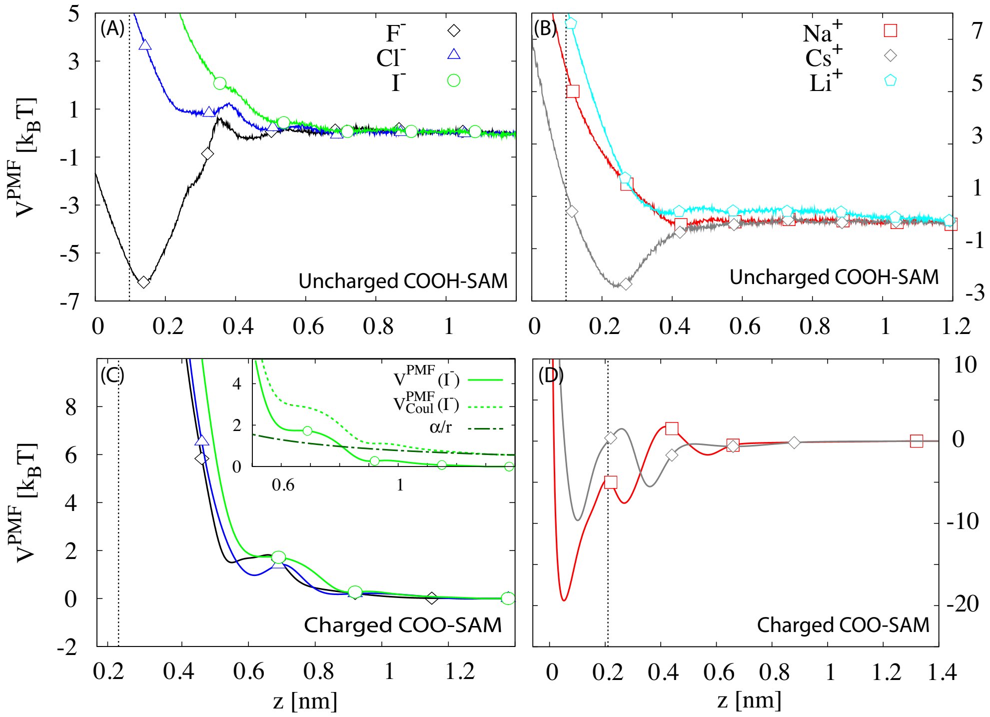

Figure 4.2.: Potentials of mean force for anions and cations at the uncharged COOH-terminated SAM (A, B) and at the charged COO$^-$-terminated SAM (C, D). For the charged surface the Coulomb interaction between the ion and surface is subtracted by fitting the long-range electrostatic repulsion/attraction. The inset in (C) displays the PMF of iodide without electrostatic interaction $V^{\mathrm{PMF}}(z)$ (solid line), with electrostatic interaction $V^{\mathrm{PMF}}_{\mathrm{Coul}}(z)$ (dotted line) and the fit to the long-ranged repulsion α/r (dashed dotted line). Vertical dotted lines denote the position of the Gibbs dividing surface z_{GDS}.

At the position of the minimum in the PMF of F$^-$, the small ion is trapped between three hydrogen atoms. This stable configuration leads to the large minimum in the ion-surface interaction. It is clearly energetically favorable for F$^-$ to level off the hydration shell facing the surface and to form contact ion pairs with three positively charged hydrogen atoms. In contrast, the large iodide ion is partially buried in the surface. Large separations between I$^-$ and the surface are energetically favorable where both the surface and the ion are completely hydrated.
Fig. 4.3C, D show simulation snapshots of Na$^+$ and Cs$^+$ at the COOH-terminated SAM. At the minimum in the PMF of Cs$^+$, this cation forms 2-3 contacts with oxygen atoms. Contact formation is observed for both parts of the functional group, the carbonyl (C=O) and the hydroxyl (C-OH) part. At the same distance Na$^+$ can form 1-3 contacts with the oxygen atoms of the terminal group. Still the smaller Na$^+$ ion is repelled and the configuration where ion and surface are hydrated is preferred.

At the charged COO$^-$-terminated SAM the surface affinity decreases with increasing ion size F$^-$ > Cl$^-$ > I$^-$ (Fig. 4.2C) as for the uncharged surface. For the cations we observe preferred binding of Na^+ compared to Cs^+ (Fig. 4.2D) in agreement with previous results [35]. The first minimum in the PMF corresponds to the CIP, the second minimum is the SIP. The alkali cations are observed to take the middle position between two carboxylate oxygens (Fig. 4.3E, F) in agreement with x-ray adsorption spectroscopy measurements and ab initio calculations [35]. Both ions strip off their hydration shell facing the surface and form a CIP with the charged carboxylate. At the minimum of the PMF of Na^+ ($z = 0.025$ nm), the Cs^+-surface interaction is larger since the large cesium ion bends the alkane chain (Fig. 4.3F). The adsorption behavior at the two surfaces is in qualitative consistence with the law of matching water affinities: deprotonating the COOH-surface group increases the charge density. Therefore, the hydration energy matches the small ions fluoride and sodium.

Due to the large adsorption of F^- at the uncharged surface and the strong adsorption of the cations at the charged COO^--surface group, we will limit the following discussion to small salt concentration and low surface charges and low fractions of charged carboxylate groups, respectively. In order to treat large bulk salt concentration, which cause high surface concentration, corrections to the PB theory are required, e.g. excluded volume corrections [149]. A review can be found in [121].

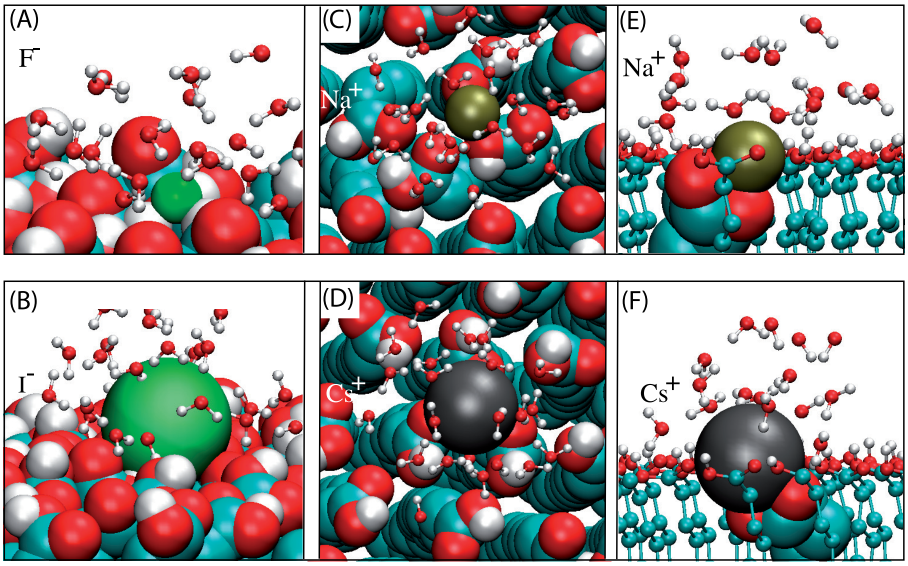

Figure 4.3.: Simulation snapshots of the configuration of F^- and I^- at the position of the PMF minimum of F^- ($z = 0.15$ nm) at the uncharged COOH-terminated SAM (A, B). Simulation snapshots (C, D) show the configuration of Na^+ and Cs^+ at the position of the minimum of Cs^+ ($z = 0.275$ nm) at the COOH-terminated SAM (top view). Simulation snapshots (E, F) show the configuration of Na^+ and Cs^+ at the charged COO^--terminated SAM at the position of the PMF minimum of Na^+ ($z = 0.025$ nm). Water molecules within 6 Å of the ion are shown. The radius of the ions corresponds to their Pauling radii.

4.3.2. Hofmeister Ordering according to Surface Tension

Fig. 4.4A, B show the surface tension increment $\Delta\gamma$ as a function of the bulk salt concentration c_0 at the uncharged COOH-terminated surface calculated from Eq. 4.4 with $\sigma_{\text{surf}} = 0$. The tension increment is positive for NaCl, NaI and LiCl since the repulsion dominates. Based on the Setschenow equation 2.18 these salts increase salting-out (decrease solubility with increasing salt concentration). Due to the strong adsorption of F^- and Cs^+ the tension increment is negative leading to salting-in (increase solubility with increasing salt concentration) in NaF and CsCl solutions. The solubility decreases with increasing ion size NaF $\gg$ NaCl $>$ NaI, the reversed Hofmeister order. In biological systems a negative tension increment in addition gives rise to partial unfolding since the molecules maximize their solvent exposed surface area [16, 19]. For the cations the solubility is highest in CsCl solutions and decreases with decreasing size CsCl $\gg$ NaCl $>$ LiCl, the direct series.

At the charged COO^--terminated SAM cation adsorption is stronger than anion repulsion. The surface tension increment is therefore always negative (Fig. 4.4C, D). Among the anions iodide is most strongly repelled. The surface tension increment is therefore largest in NaI solutions and the solubility decreases with with increasing ion size NaF $\gtrsim$ NaCl $>$ NaI, the reversed Hofmeister order that is also observed for the uncharged surface. For the cations the surface tension increment is significantly smaller for NaCl than CsCl (Fig. 4.4D). As already apparent from the single ion-surface interactions, binding

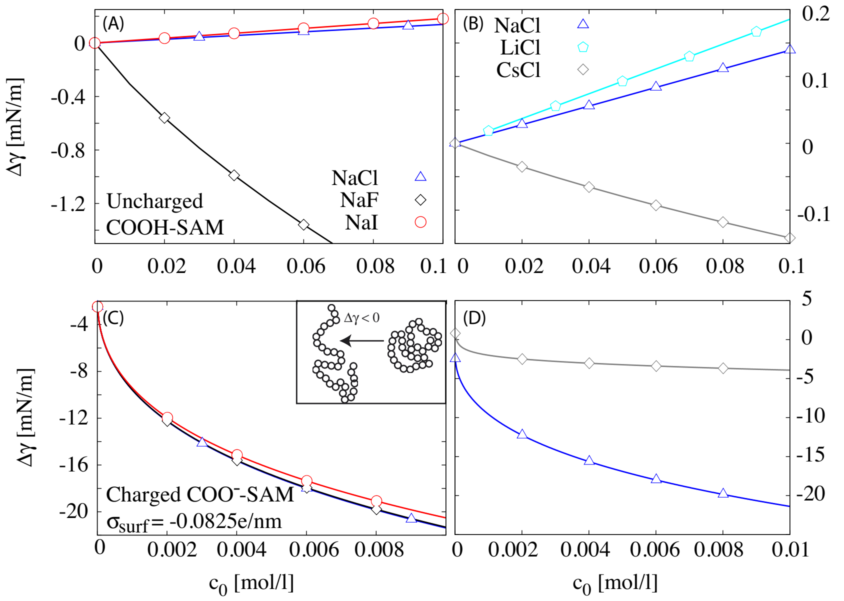

Figure 4.4.: Surface tension increment $\Delta\gamma$ obtained from thermodynamic integration as a function of the bulk salt concentration c_0 for different anions (A) and for cations (B) at the uncharged COOH-terminated SAM and for anions (C) and for cations (D) at the charged COO^--terminated SAM. The inset in (C) illustrated the schematics of protein unfolding driven by a negative $\Delta\gamma$.

of the small Na^+ ion is preferred over the large Cs^+ ion in agreement with previous results [35, 36, 98, 144]. Due to the large negative increment of NaCl, strong unfolding of macromolecules with charged carboxylate groups on their surfaces is expected in Na^+ solutions.

4.3.3. Hofmeister Phase Diagram for Continuous Charge Distributions

In the following we compare the two different approaches to model charged surfaces. In the first approach we use the ion-surface interaction at the uncharged COOH-terminated SAM and a net surface charge is accounted for in the PB approach using a constant surface charge boundary condition. This approach corresponds to the situation where charges are evenly distributed over the surface. This situation becomes experimentally relevant at low pH where ionizable groups are undissociated. In the second approach we use a combination of the ion-surface interaction at the uncharged COOH-terminated SAM and the charged COO^--surface groups. This approach corresponds to the situation where ionizable groups dissociate as function of pH leading to localized charges.

We start our discussion with the first model in which the charges are delocalized. Fig. 4.5 shows the complete Hofmeister phase diagrams for the anions and cations at the COOH-terminated SAM based on the magnitude of the effective surface charge. For each point in the parameter space of external surface charge σ_{surf} and bulk salt concentration c_0 the PB equation is solved numerically, yielding the electrostatic potential $\Phi(z)$. The

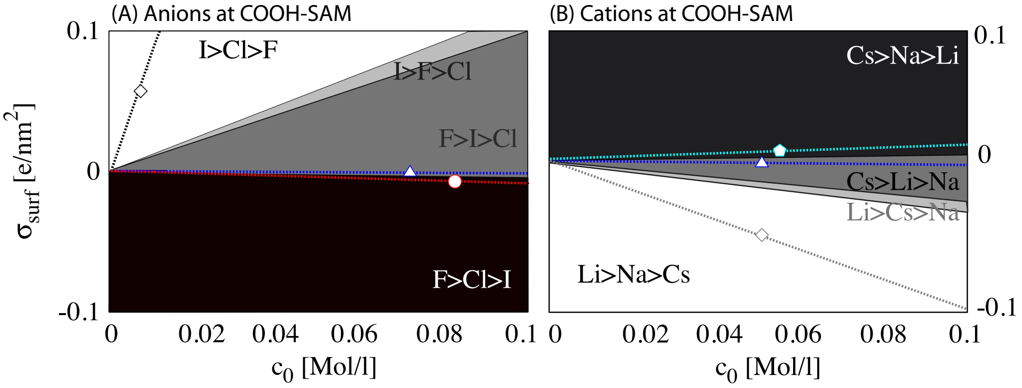

Figure 4.5.: Hofmeister phase diagrams for anions (A) and cations (B) at the COOH-terminated SAM in dependence of the external evenly distributed surface charge σ_{surf} (modeled with the constant charge boundary condition) and the bulk salt concentration c_0. Na^+ is used as counterion in case of the different anions and Cl^- in case of the different cations. Colored areas denote regions featuring direct series (white), reversed series (black) and two different alterations (gray). The ordering of the ions corresponds to their efficiency in stabilizing solutes against precipitation based on the magnitude of effective surface charge $|\sigma_{\text{DH}}|$. The dashed lines in (A) are the instability lines for NaI (red), NaCl (blue) and NaF (black) on which the long range repulsion vanishes since the bare surface charge is exactly canceled by specific ion adsorption ($\sigma_{\text{DH}} = 0$). The dashed lines in (B) are the instability lines for NaCl (blue), CsCl (gray) and LiCl (light blue).

DH potential Φ_{DH} and the effective surface charge σ_{DH} are calculated from

$$\Phi_{\mathrm{DH}} = \lim_{z \gg b} \left(\Phi(z) \mathrm{e}^{\kappa z}\right), \quad \sigma_{\mathrm{DH}} = \lim_{z \gg b} \left(\epsilon \epsilon_0 \kappa \Phi(z) \mathrm{e}^{\kappa z}\right) \tag{4.6}$$

where b is the range of the ion-surface interaction. The phase diagrams show four disconnected regions in which the ions are ranked according to their effectiveness in stabilizing solutes against precipitation based on $|\sigma_{\mathrm{DH}}|$. On negatively charged surfaces the inverse Hofmeister series is obtained for anions (Fig. 4.5A). The strong adsorption of the small fluoride ion leads to the highest effective charge and the highest stabilization. With increasing external charge two alterations occur. The direct order where fluoride is most destabilizing is only observed for high positive surface charges.

For the cations the phase diagram is exactly opposite (Fig. 4.5B). Here, the direct order is obtained at negatively charged surfaces. The largest cation cesium is most destabilizing since it compensates the external charge most efficiently. Therefore, the relation between anion/cations size and effectiveness in stabilization is *symmetric*: On the polar uniformly negatively charged COOH-terminated surface large anions and large cations are most destabilizing. This contrasts the results at the nonpolar CH_3-terminated SAM discussed in the previous chapter 3 (Fig. 3.2). The microscopic explanation is that at the nonpolar surface large ions have a higher surface affinity in agreement with hydrophobic solvation theory. At the polar COOH-terminated surface the adsorption behavior of anions and cations is opposite regarding their size: Small anions like fluoride have a high surface affinity since they form contact pairs with several hydrogen atoms. In contrast large cations like cesium have a higher surface affinity since their size matches the surface geometry of the oxygen atoms best. The combination of reversed surface affinities and opposite charge therefore leads to the symmetric relation. Note that this is not a general feature of polar surfaces since the adsorption depends, among other contribution, on the geometry of the surface and the charge distribution of the functional groups. For example, at the polar OH-terminated SAM the cation-surface affinity does not depend linearly on the ion size but a bell-shaped relation is observed as discussed in chapter 3.

4.3.4. Long-ranged Forces for Localized Charges

We now turn to the model in which the charges are localized. In this model, the heterogeneous surface consists of protonated and deprotonated carboxyl groups. We assumes that the ion interacts with the superimposed potential of uncharged COOH-surface groups and charged COO^--surface groups (nano-scale approach). The surface charge is adjusted to the number of charged carboxylate groups on the surface $\sigma_{\mathrm{surf}} = \xi \sigma_{\mathrm{COO}}$. In the following we explain the dependence of the long-ranged forces, measured by the DH potential Φ_{DH}, on the bulk salt concentration and the number of negatively charged carboxylate groups. The negative surface charge can be partially canceled or enhanced by specific ion adsorption or repulsion. The resulting effective surface charge σ_{DH} and thus the long-ranged forces between two surfaces is measured by the DH potential (Eq. 4.6). Fig. 4.6A, B show the DH potential Φ_{DH} in dependence of the fraction of negatively charged carboxylate groups ξ for two constant bulk salt concentration. At small salt concentrations $c_0 = 0.01$ M and small ξ the partially reversed order according to stabilizing efficiency $|\Phi_{\mathrm{DH}}(\mathrm{NaF})| > |\Phi_{\mathrm{DH}}(\mathrm{NaI})| > |\Phi_{\mathrm{DH}}(\mathrm{NaCl})|$ is observed (Fig. 4.6A, solid lines). With increasing negative charge i.e. for an increased number of carboxylate groups the difference between the different coions diminishes. At larger salt concentrations $c_0 = 0.1$ M reversal of the effective surface charge is observed for NaCl and NaI due to excess adsorbed Na^+ (Fig. 4.6B). For a small fraction of negatively charged carboxylate groups ξ the order is the same as before $|\Phi_{\mathrm{DH}}(\mathrm{NaF})| > |\Phi_{\mathrm{DH}}(\mathrm{NaI})| > |\Phi_{\mathrm{DH}}(\mathrm{NaCl})|$ and reflects the adsorption behavior of the anions: The strong adsorption of fluoride at uncharged COOH-surface groups leads to the largest negative DH potential (Fig. 4.6B, dashed black line). With increasing ξ, $|\Phi_{\mathrm{DH}}(\mathrm{NaF})|$ crosses the other potential lines corresponding to two partial alterations. At large fraction of charged COO^--groups the DH potential is primarily determined by the strong Na^+ adsorption. Φ_{DH} is positive and the positive contribution due to Na^+ adsorption is least compensated by the strongest repelled iodide ion and the direct order is observed.

For the cations the order in Φ_{DH} directly reflects the adsorption strength at the COOH-terminated SAM (low ξ) or at the COO^--terminated SAM (high ξ): For small salt concentrations $|\Phi_{\mathrm{DH}}(\mathrm{CsCl})| > |\Phi_{\mathrm{DH}}(\mathrm{NaCl})|$ for low ξ and reversal occurs for increasing ξ $|\Phi_{\mathrm{DH}}(\mathrm{NaCl})| > |\Phi_{\mathrm{DH}}(\mathrm{CsCl})|$ (Fig. 4.6C). At larger salt concentrations no reversal is observed and the order is always inverse $|\Phi_{\mathrm{DH}}(\mathrm{CsCl})| > |\Phi_{\mathrm{DH}}(\mathrm{NaCl})|$ (Fig. 4.6D). We estimate from our model that at moderate to high bulk salt concentration (0.1-1M) reversal occurs if the fraction of charged groups is larger than 50%. Note that this is only a rough estimate due to the limitations of our approach at high salt concentrations.

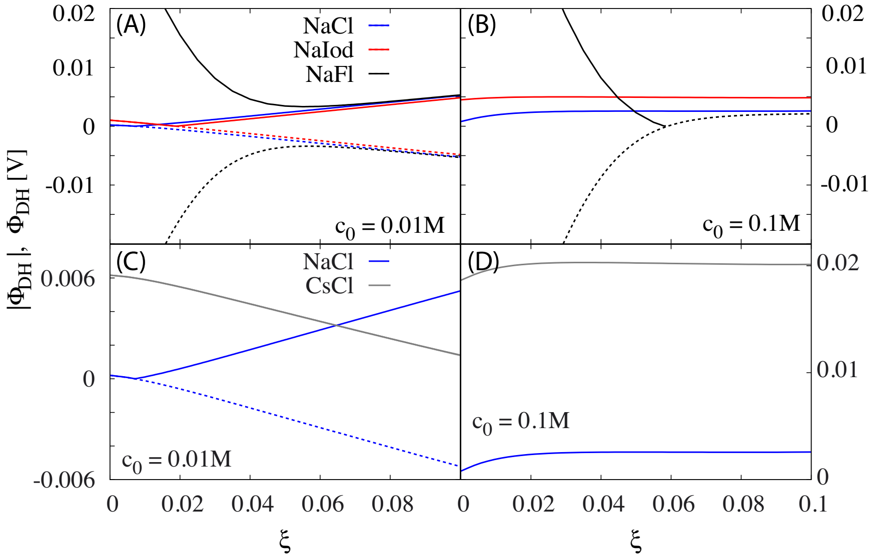

Figure 4.6.: Long range DH potential Φ_{DH} (dashed lines) and magnitude of the DH potential $|\Phi_{\mathrm{DH}}|$ (solid lines) as a function of the fraction of charged carboxylate groups ξ obtained for heterogeneous COOH-/COO^--terminated SAMs for constant bulk salt concentration $c_0 = 0.01$M (A, C) and $c_0 = 0.1$M (B, D) for anions (top) and cations (bottom). According to the original Hofmeister series $|\Phi_{\mathrm{DH}}|$ determines the efficiency of the different salts to stabilize solutes against precipitation.

4.3.5. Hofmeister Phase Diagram for Localized Charges

Fig. 4.7 shows the Hofmeister phase diagrams in dependence of the fraction of carboxylate groups ξ and the bulk salt concentration c_0. The phase diagram for anions (Fig. 4.7A) displays four regions of direct, reversed and partially altered order. At the uncharged surface (low pH) we observe a partially altered order $|\Phi_{\mathrm{DH}}(\mathrm{NaF})| > |\Phi_{\mathrm{DH}}(\mathrm{NaI})| > |\Phi_{\mathrm{DH}}(\mathrm{NaCl})|$. With increasing fraction of charged carboxylate groups ξ (moving down in the phase diagram by increasing the pH) the order is inverse and displays the surface affinity of the anions at small salt concentrations. At large salt concentrations cation binding overcompensates the negative charge of the carboxylate groups resulting in an effectively positive surface charge. The ordering of the anions is therefore a second order effect. The weakest repulsion observed for fluoride leads to the smallest effective charge and thus to the highest destabilization.

At low salt concentrations both models for localized and delocalized surface charges agree well. At large salt concentrations and high surface charges the two models differ since the different ion-surface interaction at uncharged COOH-groups and charged COO$^-$-groups becomes increasingly important. Fig. 4.7B shows the ranking of Na$^+$ and Cs$^+$ in dependence of the fraction of carboxylate groups ξ and the bulk salt concentration c_0. For the range of salt concentration and surface charges studied here, the phase diagram for localized charges matches the one for delocalized charges (Fig. 4.5).

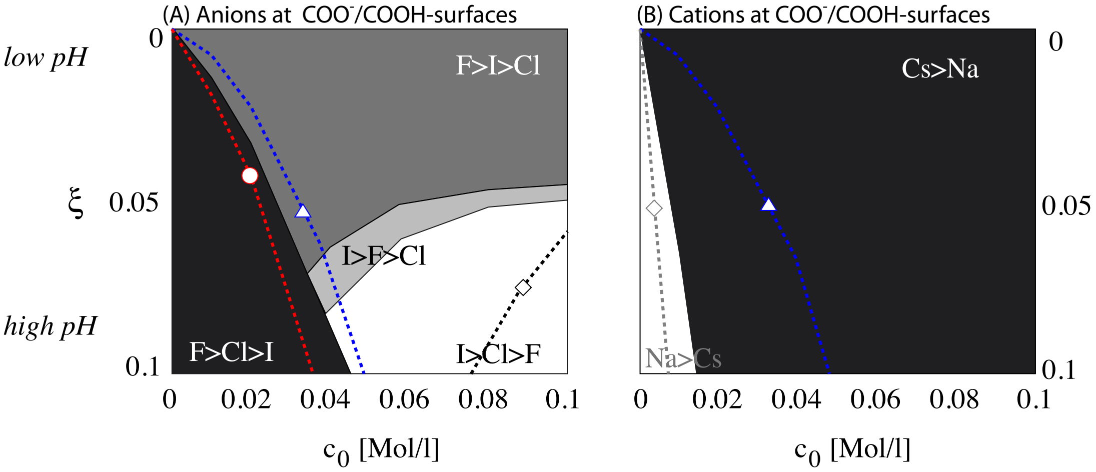

Figure 4.7.: Hofmeister phase diagram in dependence of the fraction of charged carboxylate groups ξ and bulk salt concentration c_0 at heterogeneous COO$^-$/COOH-terminated SAMs for different anions (A) and different cations (B). Na$^+$ is used as counterion in case of the different anions and Cl$^-$ in case of the different cations. Colored areas denote regions featuring direct series (white), reversed series (black) and two alterations (gray). The ordering of the ions corresponds to their efficiency in stabilizing solutes against precipitation based on the magnitude of effective surface charge $|\sigma_{\mathrm{DH}}|$. The dashed lines in (A) are the instability lines for NaI (red), NaCl (blue) and NaF (black) on which the long range repulsion vanishes since the bare surface charge is exactly canceled by specific ion adsorption. The dashed lines in (B) are the instability lines for NaCl (blue) and CsCl (gray).

4.4. Conclusion

One of the central mechanisms underlying ion specific effects is ion binding to charged surface groups [142]. Recent experimental and theoretical work [35, 36, 98, 144] has focused on the pairing of sodium and potassium with carboxylate anions in solution and carboxylate groups at protein surfaces. In this chapter, we extend the existing results and investigate ion pairing in dependence of the degree of dissociation. Using explicit-solvent MD simulations, we calculate the ion-surface interaction at SAMs with carboxyl or carboxylate as functional end groups. The single ion adsorption behavior depends strongly on whether the terminal group is dissociated or not. If the surface group is deprotonated (at high pH), the small sodium cation binds stronger to the charged carboxylate group than the large cesium ion in agreement with previous results. However, if the surface group is protonated (at low pH), the cation-surface affinity is reversed.

Due to the large negative surface tension increment of sodium salts, we predict strong unfolding of macromolecules with charged carboxylate groups on their surfaces in sodium solutions. This observation supports the explanation that sodium needs to be pumped out of the cell since strong binding of sodium to major intracellular anions like phosphates and carboxylates can weaken or even hinder the function of proteins in the cell [49].

We present two different models to describe either delocalized, uniform charge distributions at the surface or localized charges according to the number of dissociated ionizable groups at the surface. Complete Hofmeister phase diagrams display the efficiency of different anions and cations in stabilization in dependence of salt concentration and the sign of the delocalized surface charge or the degree of dissociated surface groups. For delocalized surface charges on hydrophilic COOH-terminated SAMs, we observe complete series reversal when changing the sign of the surface charge from negative to positive. At the COOH-terminated SAM small anions like fluoride and large cations adsorb strongest as a result of the different interaction sites of anions and cations. For negatively charged surfaces the anion (cation) with the highest surface affinity increases (decreases) a negative surface charge, leading to the highest (lowest) stabilization. This yields the inverse anionic and the direct cationic Hofmeister series.

For heterogeneous surfaces containing uncharged COOH- and localized, negatively charged COO^--groups, the ordering of the ions depends on the fraction of charged carboxylate groups and the salt concentration. The strong adsorption of sodium to the negatively charged carboxylate groups leads to reversal of the effective surface charge at high salt concentration due to excess adsorbed sodium causing effectively positively charged surfaces. In turn, this leads to reversal of the anion order in dependence of the bulk salt concentration. At surfaces containing carboxylate groups, sodium is a strong denaturant even at low salt concentrations. However, the efficiency in stabilization depends on the salt concentration and the fraction of charged carboxylate groups and is therefore sensitive to pH. At heterogeneous $COOH/COO^-$-surfaces ion specific stabilization is determined by the competition of ion binding to the charged carboxylate groups and the adsorption at uncharged surface patches.

4.5. Interdependency of Ionic and Surface Properties

A major difficulty that arises upon considering ion specific effects at complex interfaces is that it is impossible to decouple the effects of the various interactions. However, complex interfaces like that of a hydrated protein can to first approximation be viewed as composed of separate nonpolar, polar patches and charged surface groups [64, 67, 142]. In the previous chapters we have determined the interaction of halide anions and alkali cations with different model surfaces. The different model surfaces are designed by using different biological relevant surface groups ranging from methyl, hydroxyl, carboxyl to carboxylate groups. Our approach provides insight into the microscopic adsorption mechanism since all contributions of the ion-surface interaction are calculated explicitly by MD simulations. Using mean field Poisson-Boltzmann theory allows to calculate macroscopic properties like interfacial tension increments, long ranged-forces and critical coagulation concentrations. Thus, our bottom up approach provides a clear molecular understanding of possible ion-macromolecule interactions.

So how do ions interact with macromolecules and what is the origin of ion specific effects?

These central questions are highlighted in chapter 2-4 and we give a brief summary of the main results in the following.

Fig. 4.8 shows the interdependency of ionic and surface properties which, based on our results, determine ion specificity. Our results suggest that ion specificity is mainly

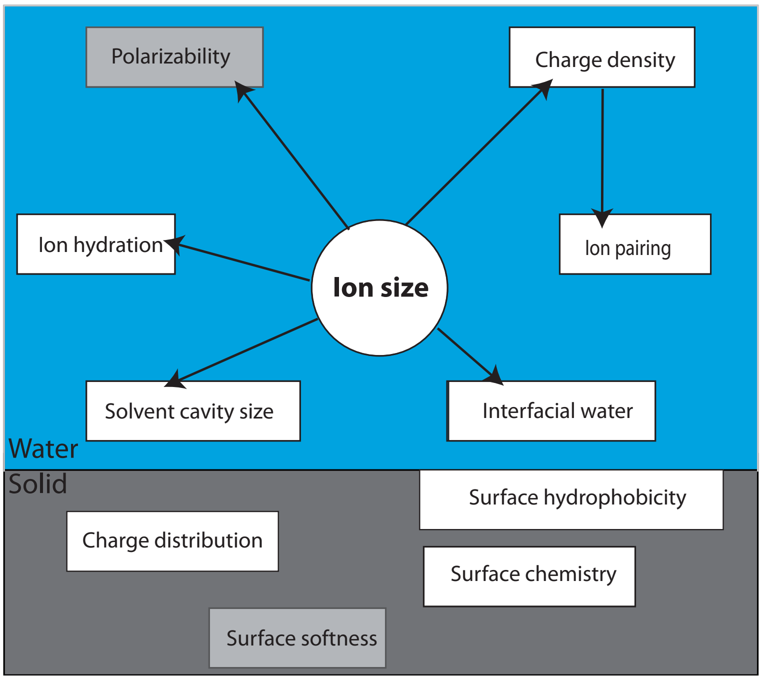

Figure 4.8.: Interdependence of ionic and surface properties which influence ion specific phenomena.

determined by the ion size and the nature of the surface. Firstly, for monovalent ions the size is equivalent to their charge density. The charge density determines the hydration of the ion in bulk and, even more important, the possible dehydration upon approaching a surface. For example, the large iodide ion is partially dehydrated at a hydrophobic surface while the strongly hydrated lithium ion retains its first hydration shell (chapter 2, 3). Secondly, the ion size determines the size of the solvent cavity. At hydrophobic surfaces, the anionic PMF differentials can be predicted by hydrophobic solvation theory based on the size of the cavity and interfacial geometry (chapter 3, [66]). Thirdly, according to Collins' rule ion size is the major property in ion pairing with charged surface groups [48, 49]. This qualitative rule agrees with the results of this chapter and recent computer simulations [144, 145]. Fourthly, the size of the ions determines their polarizability. In our present approach, we neglected ionic polarizability. The consistently optimized ionic force field without polarizability [68], which we used in our simulations, are already capable to quantitatively describe experimental surface tension increments at the air/water interface [66] and at the solid/electrolyte interface (chapter 3). Still, polarizability might become important in a situation of near-balanced forces [64, 65]. Therefore, the development and use of consistently optimized force fields including ionic polarizability will be desirable for the future.

Besides the ion size, the composition of the surface has an equally important effect on ion specificity. If the nature of the surface is changed from hydrophobic to hydrophilic, ion-surface affinities can be reversed (chapter 2). In general, large ions show a higher surface affinity at hydrophobic surfaces [1, 65, 66, 106, 136]. The anion-surface affinity is reversed on polar surfaces containing OH- or COOH-surface groups (chapter 2-4). However, this reversal is not a general feature. For example, cations at the OH-terminated surface show a bell-shaped relation between ion size and surface affinity (chapter 3) and cations at the polar COOH-terminated surface show the same affinity as on a hydrophobic surface. The type and the geometry of the functional group, the distribution of the partial charges and the distance between the functional groups, defined by the distance between the alkane chains in our model systems, influence the ion-surface interaction. For example, the surface affinity of cesium and sodium is reversed when the carboxyl group is deprotonated. Moreover, if the sign of an evenly distributed surface charge is changed or if the fraction of localized charged groups is increased (for instance by increasing the pH) the Hofmeister order according to macroscopic properties can be altered or even reversed (chapter 2-3). For the former, the reversal is a direct consequence of the competition between the external charge and the charge due to specific adsorption. For the latter, the reversal is a direct consequence of ion pairing with charged groups and adsorption at uncharged surface patches. Finally, at the solid surfaces investigated in this work, ions do not influence the conformation and do not penetrate into the surface. The conclusions extracted from the observations at solid densely packed surfaces cannot easily be transfered to quasi-gaseous or liquid-expanded systems in which ions and water can penetrate the interface. There, ions influence the structure at the interface and indirectly affect the equation of state. Determining the ion-surface interactions at such surfaces requires further simulation and development of existing theoretical models like the partitioning model [150, 151].

With all these interdependencies, we concur that there is not only one single parameter for one type of ion that describes its specific effect under all possible conditions [9]. But, our results provide a first step toward a clear molecular understanding of diverse and subtle interactions responsible for ion specific effects.

Chapter 5

Hofmeister Effects: A Global Mean-Field Analysis

5.1. Introduction

5.1.1. Motivation

Ions control almost all physicochemical processes. Even bulk salt solutions display ion-specificity, but for effects involving proteins and colloids ion-surface interactions are crucial [9]. As discussed in detail in the previous chapters the formerly presumably universal Hofmeister series is altered or even reversed when the surface charge of a protein, the surface polarity or the salt concentration is varied [1, 59, 69, 74]. Interfacial ion adsorption, evidently at the core of ion-modified aggregation effects, has been observed experimentally for different model systems [115, 152, 153].

The precise mechanism behind the pronounced surface affinity of certain ions, however, is debated due to the competition of dispersion [59], polarization [63, 65], dielectric saturation [58] as well as solvation effects [66]; theoretical modeling thus requires solvent-explicit simulations [1, 115, 154].

To obtain the effective ion specific interaction between surfaces in salt solutions, various theoretical approaches exist: i) solvent-explicit atomistic simulations of small objects in electrolyte solutions [155], here the computational bottleneck is keeping the water chemical potential constant [156], ii) solvent-implicit simulations of objects with ions subject to ion specific surface interactions derived from full simulations [142, 157], and finally iii) approximate theoretical approaches including simplified ion specific surface interactions [57, 59, 158]. Ion-surface contact potentials were introduced by Ninham and Parsegian to account for surface charge regulation within a mean-field Poisson-Boltzmann (PB) framework [159]. In subsequent ramifications, contact potential strengths were extracted from experimental affinity studies [47] and additional ion-ion interactions at the surface were accounted for [160]. In many scientific works, ion-surface potentials of finite range and different functional form were considered and ion distributions as well as effective interactions between charged surfaces were calculated by numerically solving the PB equation [59, 61, 115], in some cases effects beyond mean-field were taken into account [158].

Two main features emerge: For large separations between interacting objects, the preferential surface adsorption of one ionic species over the other gives rise to an effective surface charge and thus to an *effective repulsion* between two similar surfaces [104]. Note that fluctuation effects cause attraction even for symmetric adsorption i.e. zero net surface charge [161]. For small separations and for finite-range ion-surface interactions, on the other hand, the resulting behavior is more complex and one expects that ion-surface repulsion induces *effective attraction* between surfaces, analogous to the well-known steric depletion attraction between large objects in colloidal solutions.

5.1.2. Outline

In this chapter we derive interactions between two charged planar surfaces including finite-range ion-surface potentials. We treat the full coupling between long-ranged electrostatic and short-ranged entropic and depletion effects. The square-well ion-surface potentials in our model approximate the sum of dispersion, polarization and solvation effects. A recipe for relating realistic ion-surface interactions to our model parameters is presented. The motivation for using this simplified potential is that it makes our model tractable analytically on the PB level, and thus allows a global analysis in the complete parameter space of surface charge, salt concentration and ion-surface interaction strength. Our phase diagrams based on the equilibrium plate separation (relevant for small quickly equilibrating objects) display the salting-in/salting-out sequence characteristic for protein precipitation studies. Our pressure diagrams at large plate separation (relevant for coagulation kinetics of large colloidal objects) feature Hofmeister series reversal. We demonstrate that salting-out results both from ion-surface repulsion as well as from ion-surface adsorption, and always leads to a finite plate separation involving bound water. The case of vanishing ion-surface interactions is in fact instable with respect to plate binding.

This chapter is organized as follows: In section 5.2 we describe the details the analytical solution of the non-linear Poisson-Boltzmann equation as well as the solution in the Debye Hückel limit. In section 5.3 we present the main results for the effective interaction between ion-adsorbing plates including ion specific square-well potentials. We calculate the equilibrium salting-in/salting-out diagrams in the parameter space of salt concentration, surface charge and ion-surface affinity. Finally, the generic model is adjusted to realistic ion-surface interactions obtained from molecular dynamics simulations. The resulting Hofmeister phase diagram features direct and reversed order.

5.2. Global Mean-Field Approach

The electrostatics of an electrolyte solution between two charged plates is described by the 1D modified Poisson-Boltzmann (PB) equation [59, 115]

$$\frac{\epsilon\epsilon_0}{qc_0}\frac{d^2}{dz^2}\Phi(z) = a_-(z)e^{q\Phi(z)/k_BT} - a_+(z)e^{-q\Phi(z)/k_BT} \tag{5.1}$$

where z is the distance perpendicular to the surfaces, q the absolute ion charge, c_0 the bulk salt concentration, $\Phi(z)$ the electrostatic potential, ϵ_0 is the dielectric constant of vacuum, and ϵ the relative dielectric constant of water. Ion-specificity enters via the factors

$$a_-(z) = e^{-V^-(z)/k_BT} \quad \text{and} \quad a_+(z) = e^{-V^+(z)/k_BT} \tag{5.2}$$

which depend on the ion-surface potentials $V^\pm(z)$. To enable the analytic solution of Eq.5.1 we choose square-well potentials

$$V_S^\pm(z) = V_0^\pm\Theta(b^\pm - z) \tag{5.3}$$

of variable depth $V_0^\pm$ and range $b^\pm$, where $\Theta(z) = 1$ for $z > 0$ and $\Theta(z) = 0$ otherwise. For two surfaces at separation $2D$ we assume additivity of the interactions stemming from both surfaces and thus use

$$V^\pm(z) = V_S^\pm(z) + V_S^\pm(2D - z). \tag{5.4}$$

For symmetrically charged plates with surface charge density σ_{surf}, the boundary conditions read $d\Phi(z)/dz = -\sigma_{\text{surf}}/\epsilon_0\epsilon$ at $z = 0$ and $d\Phi(z)/dz = 0$ at $z = D$. The solution of Eq. 5.1 is described in detail in the next section.

5.2.1. Solution of the Poisson-Boltzmann Equation Including Square-well Potentials

Eq. 5.1 is solved separately in the two regions where the ion-surface potential is constant, referred to as region I and region II (see Fig. 5.1). In the following we assume identical potential ranges for cations and anions $b^+ = b^- = b$. Note that for potential overlap, $b = 2D - b_0$, where b_0 is the range of the interaction potential without overlap (Fig. 5.1C). Integrating Eq. 5.1 yields

$$\left(\frac{d\Phi(z)}{dz}\right)^2 = \frac{2qc_0k_BT}{\epsilon_0\epsilon q}(a_+e^{-q\Phi(z)/k_BT} + a_-e^{q\Phi(z)/k_BT} + C) \tag{5.5}$$

with integration constant C. Note that in bulk solution (far away from the surface where the ion-surface interaction is zero, i.e., $a_+ = a_- = 1$) the integration constant $C = -2$ and one obtains the Gouy-Chapman result which satisfies the boundary conditions $d\Phi/dz = 0$ and $\Phi = 0$.
The substitution $y = e^{q\Phi/k_BT}$ yields

$$\frac{dy}{dz} = \kappa\sqrt{y^2(a_+y^{-1} + a_-y + C)} \tag{5.6}$$

where $\kappa = \sqrt{\frac{2c_0 q^2}{\epsilon_0 \epsilon k_B T}}$ is the inverse Debye screening length. The right hand side can be factorized

$$\kappa dz = \frac{dy}{\sqrt{a_-(y-n_0)(y-n_1)(y-n_2)}} \tag{5.7}$$

where the n_i are the roots of the polynomial $y^2(a_+ y^{-1} + a_- y + C)$

$$\begin{aligned} n_0 &= 0 && (5.8) \\ n_1 &= \frac{-C - \sqrt{|C^2 - 4a_+ a_-|}}{2a_-} && (5.9) \\ n_2 &= \frac{-C + \sqrt{|C^2 - 4a_+ a_-|}}{2a_-}. && (5.10) \end{aligned}$$

Eq. 5.7 can be integrated if the location of the roots with respect to y is known [162], yielding the solutions $\Phi_I(z)$ and $\Phi_{II}(z)$ in region I and II which have to satisfy the following boundary conditions (BC)

$$\begin{aligned} \text{(i)} \quad \left.\frac{d\Phi_I(z)}{dz}\right|_{z=0} &= -\frac{\sigma_{\text{surf}}}{\epsilon\epsilon_0} && (5.11) \\ \text{(ii)} \quad \left.\frac{d\Phi_{II}(z)}{dz}\right|_{z=\infty} &= \Phi_{II}(z)|_{z=\infty} = 0 && (5.12) \\ \text{(iii)} \quad \left.\frac{d\Phi_{II}(z)}{dz}\right|_{z=D} &= 0 && (5.13) \\ \text{(iv)} \quad \left.\frac{d\Phi_I(z)}{dz}\right|_{z=b} &= \left.\frac{d\Phi_{II}(z)}{dz}\right|_{z=b} && (5.14) \\ \text{(v)} \quad \Phi_I(z)|_{z=b} &= \Phi_{II}(z)|_{z=b} && (5.15) \end{aligned}$$

with the external surface charge σ_{surf} and the position of the mid-plane D. Boundary condition (ii) is used in case of a single surface and (iii) is used in case of two parallel plates. The matching conditions (iv) and (v) are used to provide a continuous, differentiable potential at b.

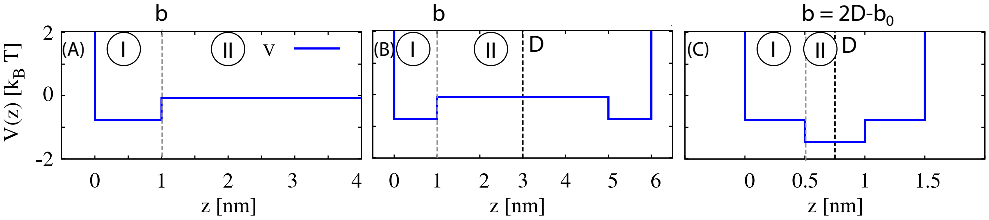

Figure 5.1.: Ion-surface interaction potential $V(z)$ (A) for a single plate, (B) for parallel plates at distance $2D = 6$ without potential overlap, (C) parallel plates at distance $2D = 1.5$ with partial potential overlap. I, II refer to the regions where the ion-surface interaction potential is constant.

The possible locations of the roots with respect to y are

- L$_1$: $y > n_2 > n_1 > 0$
- L$_2$: $n_2 > y > n_1 > 0$
- L$_3$: $n_2 > n_1 > y > 0$.

Note that at the root the derivative $\frac{\mathrm{d}y}{\mathrm{d}z} = 0$ according to Eq. 5.6. The second integration yields for the two regions $i = I, II$

$$\int_{z_i^0}^{z} \kappa \mathrm{d}z' = \int_{y(z^0)}^{y(z)} \frac{\mathrm{d}y'}{\sqrt{f(y')}} = \int_{y(z^0)}^{n^*} \frac{\mathrm{d}y'}{\sqrt{f(y')}} + \int_{n^*}^{y(z)} \frac{\mathrm{d}y'}{\sqrt{f(y')}}$$
$$= \begin{cases} \frac{2}{\sqrt{a_{-i}n_{2i}}} \left(-F(\mu(y(z_i^0)), q) + F(\mu(y(z)), q)\right) & \text{for } L1, n^* = n_2; \\ \frac{2}{\sqrt{a_{-i}n_{2i}}} \left(-F(\chi(y(z_i^0)), p) + F(\chi(y(z)), p)\right) & \text{for } L2, n^* = n_1; \\ \frac{2}{\sqrt{a_{-i}n_{2i}}} \left(F(\delta(y(z_i^0)), q) - F(\delta(y(z)), q)\right) & \text{for } L3, n^* = n_1; \end{cases} \tag{5.16}$$

where $F(\phi, k)$ is an Elliptic Integral of the first kind (we use the definition of [163]) with

$$\mu(y) = \arcsin\sqrt{\frac{y - n_{2i}}{y - n_{1i}}}; \quad q = \sqrt{\frac{n_{1i}}{n_{2i}}} \tag{5.17}$$

$$\chi(y) = \arcsin\sqrt{\frac{n_{2i}(y - n_{1i})}{(n_{2i} - n_{1i})y}}; \quad p = \sqrt{\frac{n_{2i} - n_{1i}}{n_{2i}}} \tag{5.18}$$

$$\delta(y) = \arcsin\sqrt{\frac{n_{2i}(n_{1i} - y)}{n_{1i}(n_{2i} - y)}}; \quad q = \sqrt{\frac{n_{1i}}{n_{2i}}} \tag{5.19}$$

$$\tag{5.20}$$

and $z_I^0 = b$ and $z_{II}^0 = D$.

Since the derivative of the potential vanishes at the mid-plane D (BC (iii)), $y(z^0 = D) = n_{jII}$ for j=1,2 and the first Elliptic Integrals in dependence of z^0 in the sum in Eq. 5.16 vanish. Using the definition of the Jacobi Elliptic Functions yields the expression of the potential in dependence of the location of the roots with respect to y

$$\Phi_i(z) = \frac{k_B T}{q} \begin{cases} \ln\left(\frac{n_{2i} - n_{1i}(\mathrm{sn}(0.5\sqrt{a_{-i}n_{2i}}(-\kappa z_i^0 + F(\mu(y(z_i^0)), q) + \kappa z, q^2)))^2}{1 - (\mathrm{sn}(0.5\sqrt{a_{-i}n_{2i}}\kappa z, q^2))^2}\right) & \text{for L1;} \\ \ln\left(\frac{n_{1i}n_{2i}}{n_{2i} + (n_{1i} - n_{2i})(\mathrm{sn}(0.5\sqrt{a_{-i}n_{2i}}(-\kappa z_i^0 + F(\chi(y(z_i^0)), p) + \kappa z, p^2)))^2}\right) & \text{for L2;} \\ \ln\left(-\frac{n_{1i} - n_{1i}(\mathrm{sn}(0.5\sqrt{a_{-i}n_{2i}}(\kappa z_i^0 + F(\delta(y(z_i^0)), q) - \kappa z, q^2)))^2}{-1 + \frac{n_{1i}}{n_{2i}}(\mathrm{sn}(0.5\sqrt{a_{-i}n_{2i}}(z_i^0 - F(\delta(y(z_i^0)), q) - z, q^2)))^2}\right) & \text{for L3;} \end{cases} \tag{5.21}$$

and the derivative

$$\frac{\mathrm{d}\Phi_i(z)}{\mathrm{d}z} = \frac{k_BT}{q}\begin{cases} \frac{\kappa\sqrt{a_{-i}n_{2i}}\mathrm{sn}(\tilde{z},q^2))\mathrm{cn}(\tilde{z},q^2)\mathrm{dn}(\tilde{z},q^2)(n_{1i}-n_{2i}))}{n_{2i}-n_{1i}(\mathrm{sn}(\tilde{z},q^2))^2(1-(\mathrm{sn}(\tilde{z},q^2)))} & \text{for L1} \\ \frac{\kappa\sqrt{a_{-i}n_{2i}}\mathrm{sn}(\tilde{z},p^2)\mathrm{cn}(\tilde{z},p^2)\mathrm{dn}(\tilde{z},p^2)(n_{1i}-n_{2i})}{n_{2i}-(n_{2i}-n_{1i})(\mathrm{sn}(\tilde{z},p^2))^2} & \text{for L2} \\ -\frac{\kappa\sqrt{a_{-i}n_{2i}}\mathrm{sn}(\tilde{z},q^2)\mathrm{cn}(\tilde{z},q^2)\mathrm{dn}(\tilde{z},q^2)(n_{1i}-n_{2i})}{n_{2i}-n_{2i}(\mathrm{sn}(\tilde{z},q^2))^2-n_{1i}(\mathrm{sn}(\tilde{z},q^2))^2+n_{1i}(\mathrm{sn}(\tilde{z},q^2))^4} & \text{for L3} \end{cases} \tag{5.22}$$

where

$$\tilde{z} = \begin{cases} 0.5\sqrt{a_{-i}n_{2i}}(-\kappa z_i^0 + F(\mu(y(z_i^0)), q) + \kappa z) & \text{for L1} \\ 0.5\sqrt{a_{-i}n_{2i}}(-\kappa z_i^0 + F(\chi(y(z_i^0)), p) + \kappa z) & \text{for L2} \\ 0.5\sqrt{a_{-i}n_{2i}}(+\kappa z_i^0 + F(\delta(y(z_i^0)), q) - \kappa z) & \text{for L3} \end{cases}$$

For a single plate one obtains in region II the usual Gouy-Chapman result

$$\Phi_{II}(z) = \frac{2k_BT}{q}\ln\left(\frac{e^{qC_{II}^{\mathrm{GC}}/2k_BT} + (e^{qC_{II}^{\mathrm{GC}}/2k_BT} - 1)e^{-\kappa z} + 1}{e^{qC_{II}^{\mathrm{GC}}/2k_BT} - (e^{qC_{II}^{\mathrm{GC}}/2k_BT} - 1)e^{-\kappa z} + 1}\right) \tag{5.23}$$

where the constant C_{II}^{GC} is related to the value of the potential Φ_b at $z = b$ (or any other arbitrary value) via

$$C_{II}^{\mathrm{GC}} = \frac{2k_BT}{q}\ln\left(\frac{e^{q\Phi_b/2k_BT} + e^{q\Phi_b/2k_BT}e^{-\kappa b} - 1 + e^{-\kappa b}}{-e^{q\Phi_b/2k_BT} + e^{q\Phi_b/2k_BT}e^{-\kappa b} + 1 + e^{-\kappa b}}\right). \tag{5.24}$$

To determine the free parameters C_I, C_{II} and C_{II}^{GC} we choose a value for the potential at the mid-plane $\Phi(z = D)$ for two parallel plates or at b in the case of a single plate. For a single plate C_{II}^{GC} is obtained directly from Eq. 5.24. For parallel plates the derivative vanishes at D (BC (iii)) and Eq. 5.6 yields C_{II}. Therewith, the value of the roots and the potential in region II is determined. Using the value of the potential and the derivative at b yields due to BC (iv) and (v) the remaining parameter C_I via Eq. 5.6. Therewith, the roots and the solution in region I is determined. The derivative of the potential at the surface yields the surface charge (BC (i)).

Fig. 5.2 shows a comparison of the analytical solution and the numerical solution of the PB equation for an uncharged and a charged plate. Both results are in perfect agreement.

Overall Constant Ion-surface Interaction Potential

For an overall constant adsorption potential, i.e. for completely overlapping ion-surface interaction potentials or for contact of two adsorption wells and zero external charge, the derivative of the electrostatic potential has to vanish everywhere. Therefore, the roots have to be equal, $n_1 = n_2$, according to Eq. 5.22. This is realized for the integration constant $C = 2\sqrt{a_-a_+}$, yielding $n_1 = n_2 = \sqrt{a_+/a_-}$. Then, the electrostatic potential has the constant value $\Phi = \frac{k_BT}{q}\ln\sqrt{a_+/a_-}$ and the concentrations of anions and cations are equal, $c_+ = c_- = c_0\sqrt{a_-a_+}$.

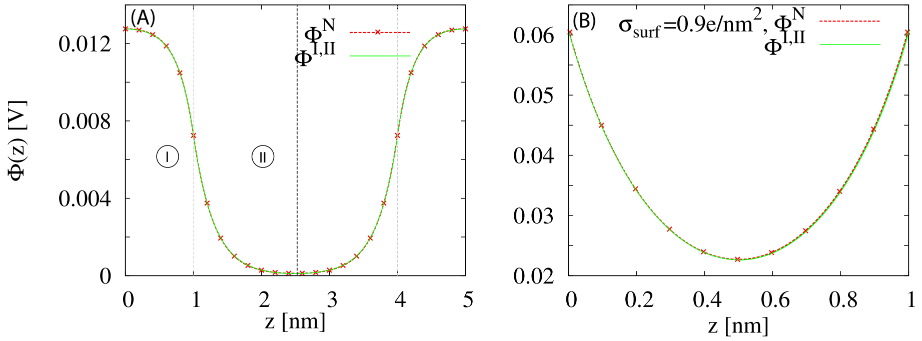

Figure 5.2.: Comparison of the analytical result (green line) and the numerical solution (red dashed line): (A) Electrostatic potential $\Phi(z)$ as a function of the distance z from the surface for uncharged plates and ion-surface potentials $V_0^+ = -1k_BT$, $V_0^- = 0$, interaction range $b = 1$ nm, plate separation $2D = 5$ nm and salt concentration $c_0 = 1$M. (B) Electrostatic potential for charged plates with an external charge $\sigma_{\text{surf}} = 0.9$ e/nm^2 for $2D = 1$ nm and $c_0 = 100$mM.

5.2.2. Solution in the Debye-Hückel Limit

In order to verify our results and to obtain the limiting value of the surface potential for zero salt concentration we solve the PB equation in the Debye-Hückel (DH) limit. For $q\Phi \ll k_BT$ the modified PB equation can be linearized using $e^{-q\Phi/k_BT} \approx 1 - q\Phi/k_BT$

$$\frac{d^2\Phi}{dz^2} = -\sum_{\pm} \frac{q^{\pm}c_0 a_{\pm}}{\epsilon\epsilon_0}\left(1 - \frac{q^{\pm}\Phi}{k_BT}\right) = \kappa'^2\Phi - J \tag{5.25}$$

with the modified inverse Debye screening length κ'

$$\kappa'^2 = \frac{q^2c_0}{\epsilon\epsilon_0 k_BT}(a_+(z) + a_-(z)) = \begin{cases} \kappa_I^2 = \frac{q^2c_0}{\epsilon\epsilon_0 k_BT}(a_{+I} + a_{-I}) & ; z < b \\ \kappa_{II}^2 = \frac{q^2c_0}{\epsilon\epsilon_0 k_BT}(a_{+II} + a_{-II}) & ; z > b \end{cases} \tag{5.26}$$

and the parameter J defined as

$$J(z) = \frac{qc}{\epsilon\epsilon_0}(a_+(z) - a_-(z)) = \begin{cases} J_I & ; z < b \\ J_{II} & ; z > b. \end{cases} \tag{5.27}$$

Eq. 5.25 can be integrated twice yielding

$$\frac{1}{\kappa'}\left(\ln(2(-J + \kappa'^2\Phi + \kappa'\sqrt{C_1 - 2J\Phi + \kappa'^2\Phi^2} + K_2)\right) = z \tag{5.28}$$

where C_1 and K_2 are the integration constants. Therefore, the electrostatic potential reads

$$\Phi(z) = \frac{1}{4\kappa'}(-4C_1\kappa'^2C_2^{-1}e^{-\kappa z} + 4J^2C_2^{-1}e^{-\kappa' z} + 4J + C_2e^{\kappa' z}) \tag{5.29}$$

with $C_2 = e^{\kappa' K_2}$. C_1 and C_2 are determined by the boundary conditions as follows: Using BC (i) and (iii) yields for the integration constants in region I

$$C_{1I} = -\frac{-4J_I^2 + C_{2I}^2 - 4\Sigma C_{2I}\kappa_I}{4\kappa_I^2} \tag{5.30}$$

and in region II

$$C_{1II} = -\frac{-4J_{II}^2 e^{-\kappa_{II}D} + C_{2II}e^{\kappa_{II}D}}{\kappa_{II}^2 e^{-\kappa D}}. \tag{5.31}$$

Therewith, the electrostatic potential reads

$$\Phi_I(z) = \frac{1}{4\kappa_I^2}\left(C_{2I}e^{-\kappa_I z} - 4e^{-\kappa_I z}\Sigma\kappa_I + 4J_I + C_{2I}e^{\kappa_I z}\right) \tag{5.32}$$

$$\Phi_{II} = \frac{(e^{\kappa_{II}(2D-z)}C_{2II} + 4J_{II} + C_{2II}e^{\kappa_{II}z})}{4\kappa_{II}^2}. \tag{5.33}$$

For a single plate the solution in region II is the DH limit of Eq. 5.23

$$\Phi_{II}(z) = C_{II}^{DH}e^{-\kappa z}. \tag{5.34}$$

Using the matching conditions BC (iv) and (v) determines the integration constants C_{2I} and C_{2II} for two parallel plates and C_{II}^s and C_{II}^{DH} for a singe plate:

$$C_{2I} = -\frac{-4\kappa_{II}^2 e^{-\kappa_I b}\Sigma\kappa_I + 4\kappa_{II}^2 J_I - \kappa_I^2 e^{-\kappa_{II}(-2D+b)}C_{2II} - 4\kappa_I^2 J_{II} - \kappa_I^2 C_{2II}e^{\kappa_{II}b}}{\kappa_{II}^2(e^{-\kappa_I b} + e^{\kappa_I b})} \tag{5.35}$$

$$C_{2II} = \frac{4(\kappa_{II}^2 e^{-\kappa_I b}J_I - e^{-\kappa_I b}\kappa_I^2 J_{II} + 2\kappa_{II}^2 e^{-\kappa_I b}\Sigma\kappa_I e^{\kappa_I b} - e^{\kappa_I b}\kappa_{II}^2 J_I + e^{\kappa_I b}\kappa_I^2 J_{II})}{\kappa_I((\kappa_I - \kappa_{II})e^{\Delta_1} - (\kappa_I\kappa_{II})e^{\Delta_2} + (\kappa_I + \kappa_{II})e^{-b(\kappa_I - \kappa_{II})} - (\kappa_I - \kappa_{II})e^{b(\kappa_{II}+\kappa_I)})} \tag{5.36}$$

$$C_{2I}^s = -\frac{4(-\kappa_{II}e^{-\kappa_I z}\Sigma\kappa_I + \kappa_{II}J_I + e^{\kappa_{II}b}e^{-\kappa_{II}z}\kappa_I^2 e^{-\kappa_I b}\Sigma)}{\kappa_{II}e^{-\kappa_I z} + \kappa_{II}e^{\kappa_I z} - e^{\kappa_{II}b}e^{-\kappa_I z}\kappa_I e^{-\kappa_I b} + e^{\kappa_{II}b}e^{-\kappa_{II}z}\kappa_I e^{\kappa_I b}} \tag{5.37}$$

$$C_{II}^{DH} = \frac{(e^{-\kappa_I b}C_{2I}^s - 4e^{-\kappa_I b}\Sigma\kappa_I - C_{2I}^s e^{\kappa_I b})e^{\kappa_{II}b}}{4\kappa_{II}\kappa_I}. \tag{5.38}$$

with $\Delta_1 = 2\kappa_{II}D - \kappa_{II}b - \kappa_I b$ and $\Delta_2 = 2\kappa_{II}D - \kappa_{II}b + \kappa_I b$.

Zero Concentration Limit

In the limit $c_0 \to 0$ the potential in region I has a removable singularity. The potential for uncharged parallel plates is constant and has the value

$$\lim_{c_0\to 0}\Phi(z=0) = \frac{t_I b + t_{II}D - t_{II}b}{k_I^2 b - k_{II}^2 b + k_{II}^2 D} \tag{5.39}$$

with

$$t_i = \frac{q}{\epsilon\epsilon_0}(a_{+i} - a_{-i}) \tag{5.40}$$

and

$$k_i = \sqrt{\frac{q^2}{\epsilon\epsilon_0 k_B T}(a_{+i} + a_{-i})} \tag{5.41}$$

for $i = I, II$.

However, for a single plate or in the limit $D \to \infty$ the potential is zero in the limit of vanishing salt concentration.

$$\lim_{c_0 \to 0} \Phi(z = 0) = 0. \tag{5.42}$$

Comparison of DH Limit and Full Analytical Solution

In order to verify our analytical solution of the PB equation, we compare the surface potential Φ_0 as a function of the electrolyte concentration c_0 obtained from the full solution with the result in the DH limit in Fig. 5.3. If the overall potential is small, both results are in perfect agreement (Fig. 5.3B).

The effect of salt addition depends on the plate separation: At large distances between the surfaces the surface potential increases with increasing salt concentration since more anions adsorb at the surface while at small plate separations the surface potential decreases and the density of anions around the mid-plane increases due to higher screening. For finite distances between the two surfaces the surface potential does not vanish in the limit of zero concentration but the potential has a constant value determined by the strength of ionic adsorption $V_0^{\pm}$ and the plate separation $2D$ (Eq. 5.39) and vanishes as the plate separation goes to infinity (Eq. 5.42).

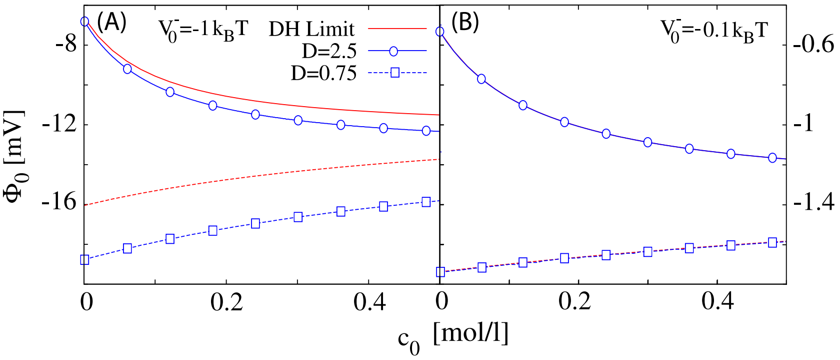

Figure 5.3.: Comparison of the surface potential Φ_0 in dependence of the bulk salt concentration c_0 obtained from the full non-linear solution (blue line) and in the DH limit (red line) for different values of the anion adsorption potential $V_0^- = -1k_B\mathrm{T}$ (A) and $V_0^- = -0.1k_B\mathrm{T}$ (B). The surface potential is shown for two different plate separations: $D = 2.5$ nm (open circles) and $D = 0.75$ nm (open squares). The interaction range $b = 1$ nm and the cation-surface interaction potential $V_0^+ = 0$. If the overall potential is small both methods are in perfect agreement (lines on top of each other in (B)).

5.2.3. Free Energy in the Poisson-Boltzmann Model

The free energy per area F within the PB model is a function of the ionic concentrations

$$c^{\pm}(z) = c_0 e^{-\left(V^{\pm}(z) + q^{\pm}\Phi(z)\right)/k_B T} \tag{5.43}$$

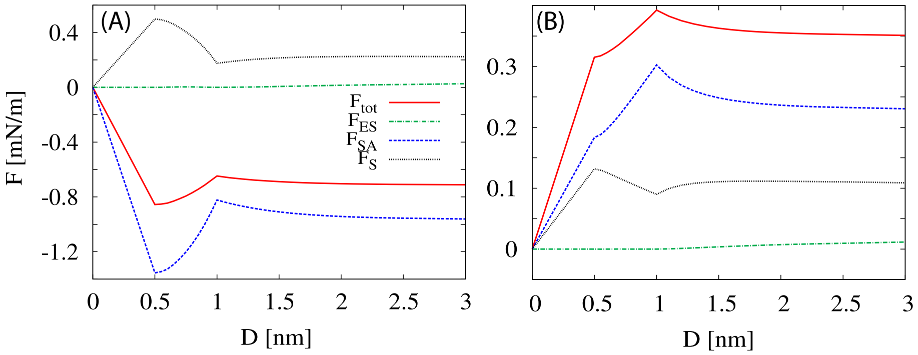

Figure 5.4.: Free energy per area F_{tot}, electrostatic contribution F_{ES}, mixing entropy F_{S} and specific adsorption contribution to the free energy F_{SA} (A) for anion adsorption $V_0^- = -1k_B\text{T}$ and (B) for anion repulsion $V_0^- = 1k_B\text{T}$ as a function of the plate separation $2D$ and $V_0^+ = 0$ for 100 mM salt concentration. The main contribution to the free energy is the contribution due to specific adsorption.

and the electrostatic potential $\Phi(z)$

$$\begin{aligned}
F(D) &= \int_0^{2D}\left[\frac{1}{2}(c^+(z)-c^-(z))q\Phi(z)\right]dz \\
&+ k_BT\int_0^{2D}\left[c^+(z)\ln\left(\frac{c^+(z)}{c_0}\right)+c^-(z)\ln\left(\frac{c^-(z)}{c_0}\right)-c^+(z)-c^-(z)+2c_0\right]dz \\
&+ \int_0^{2D}\left[V^+(z)c^+(z)+V^-(z)c^-(z)\right]dz \\
&+ \sigma_{\text{surf}}\Phi(z=0). \qquad (5.44)
\end{aligned}$$

The first integral is the electrostatic energy, while the second one represents the ideal mixing entropy of a dilute solution of anions and cations. The third integral takes into account the ion-surface interaction and the last term is the surface electrostatic energy which couples an external charge σ_{surf} with the value of the surface potential $\Phi(z=0)$.

Note that the free energy expression does not directly yield the relation between the electrostatic potential and the ion density via minimization since the two fields depend implicitly via the Poisson equation on each other.

Fig. 5.4A,B show the different contributions to the free energy in dependence of the plate separation for anion adsorption and anion repulsion.

5.2.4. Lines of Instability and Local Minima of the Free Energy

The long range repulsion between two plates vanishes if the external surface charge is exactly canceled by the charge due to specific ion adsorption. This corresponds to an instability since the long range repulsion vanishes. This point is described by the requirement that the free energy is independent of the plate separation i.e. the pressure $p = -dF/dD = 0$ and the potential has to vanish for $z \geq b$. Therefore, the roots in region II are equal $n_{2II} = n_{1II} = 1$ and the potential has the value $\Phi = \frac{k_B T}{q} \ln n_{1II} = 0$ for $z \geq b$.

However, the potential in region I is not constant and is determined by the matching conditions. Since the derivative $d\Phi(b)/dz = 0$ the Elliptic Integral in dependence of $z_I^0 = b$ vanishes $F(\mu(y(z_I^0)) = 0$.
Due to the matching condition $n_{2I} = 1$. Therefore, $C_I = -a_{1I} - a_{2I}$ and the critical charge can be calculated directly from

$$\sigma_{\text{surf}} = -\epsilon\epsilon_0 \left. \frac{d\Phi_I(z)}{dz} \right|_{z=0} . \tag{5.45}$$

The resulting lines of instability (labeled as σ_{crit}) are shown in Fig. 5.7 and Fig. 5.8 of the next section.

The position of the local minimum of the free energy in the region of partial overlap coincides with the requirement that the potential and therefore the salt concentration is constant for $z \geq b$. Therefore, the roots are equal

$$n_{2II} = n_{1II} = \sqrt{a_{+II}/a_{-II}} \tag{5.46}$$

for $z \geq b$. The dotted lines in Fig. 5.7 A, D show the local minimum of the free energy. With increasing charge the local minimum and therefore the transition from repulsion to attraction is shifted to larger plate separations.

5.3. Results and Discussion

After having demonstrated that the modified PB equation including square-well potential is solved piecewise by Jacobi elliptic functions ion density profiles $c^{\pm}(z)$ as well as pressure and free energy are derived. Assuming identical potential ranges for cations and anions, $b^{+} = b^{-} = b$, and rescaling the spatial coordinate or equivalently fixing $b = 1$ nm, we are left with only four parameters, namely σ_{surf}, $V_0^{\pm}$ and c_0. To simplify the following discussion, we set $V_0^{+} = 0$ and concentrate on the effect of the anion adsorption strength, see Fig. 5.5 for an illustration.

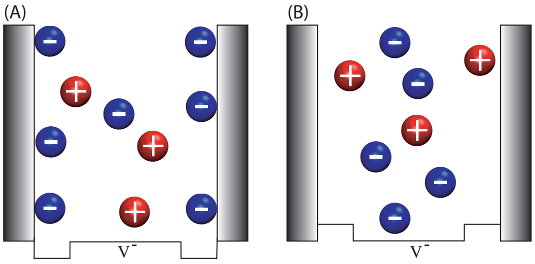

Figure 5.5.: Schematic ion distribution between two parallel plates for anion-surface attraction (A) and repulsion (B).

5.3.1. Ionic Distribution

Fig. 5.6 shows the electrostatic potential $\Phi(z)$ as well as the anion and cation density profiles $c^{\pm}(z)$ for three different plate separations $2D$ for neutral plates ($\sigma_{\mathrm{surf}} = 0$) and anion adsorption ($V_0^{-} = -1k_B$T). Due to anion adsorption, the electrostatic potential is

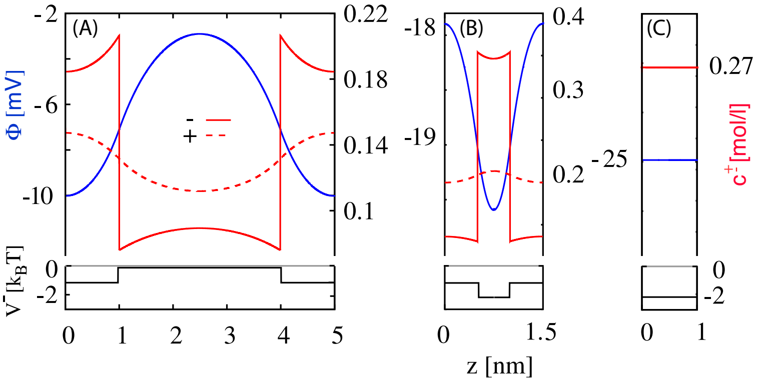

Figure 5.6.: Electrostatic potential $\Phi(z)$, ionic concentration profiles $c^{\pm}(z)$ and anion-surface potential $V^{-}(z)$ for $c_0 = 100$mM bulk salt concentration, interaction range $b = 1$ nm and interaction strength $V_0^{-} = -1k_B$T: (A) Large plate separation without potential overlap ($D = 2.5$ nm), (B) medium plate separation with partial potential overlap ($D = 0.75$ nm), and (C) small plate separation with complete potential overlap ($D = 0.5$ nm).

negative but exhibits different shapes for the cases where the surface-ion potentials do not overlap, $D > b$, and where they overlap partially, $D < b$. Accordingly, the anion density is maximal within the adsorption well in Fig. 5.6A but is maximal in the potential overlap region in the middle between the plates in Fig. 5.6B. Note that this feature is specific to our additivity assumption for the two surface potentials. For plate separations $2D < b$ in Fig. 5.6C, the potential and density profiles are constant.

5.3.2. Effective Interaction between Ion-adsorbing Plates

The free energy results from the competition of electrostatic interactions, ion entropy and specific adsorption effects and follows directly from $\Phi(z)$ using Eq. 5.44. We show the free energy per unit area F for fixed salt concentration $c_0 = 100$mM for anion adsorption $V_0^- = -1k_B$T in Fig. 5.7A,B and for anion repulsion $V_0^- = 1k_B$T in Fig. 5.7C, D for various σ_{surf} as a function of D.

We start the discussion with anion adsorption at uncharged plates (black curve) in Fig. 5.7A,B. As expected, the free energy is maximal at contact ($D = 0$) and decreases for

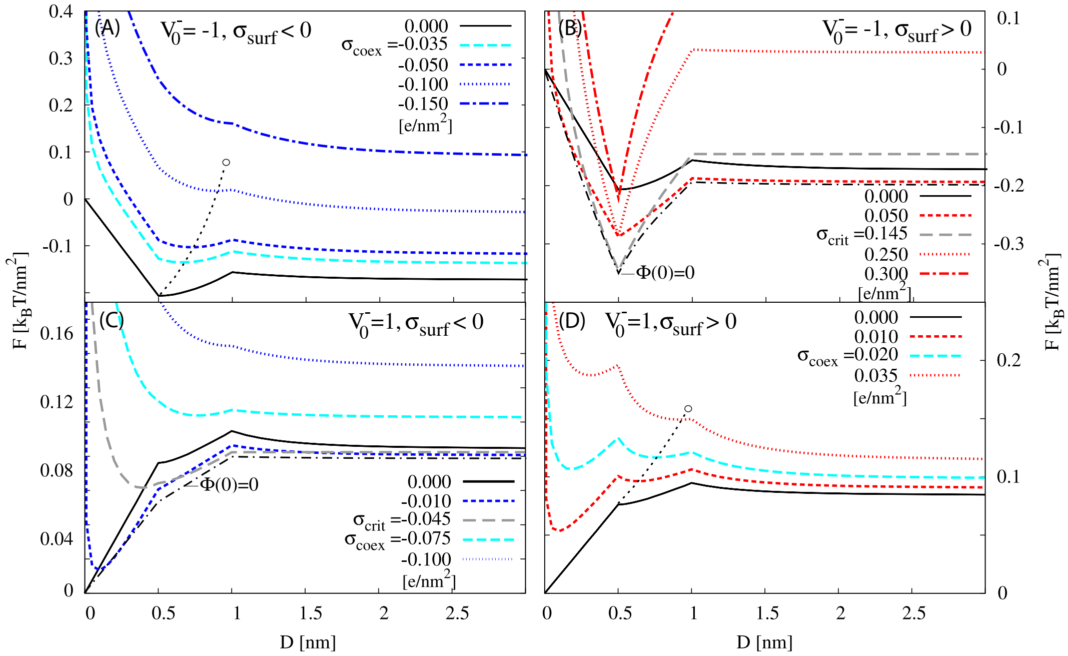

Figure 5.7.: Free energy per area in dependence of the plate separation $2D$ for anion adsorption $V_0^- = -1k_B$T (A, B) and repulsion $V_0^- = 1k_B$T (C, D) for different values of the bare plate charge σ_{surf} for $c_0 = 100$mM salt and interaction range $b = 1$ nm. σ_{crit} is the critical charge for which $\sigma_{\text{eff}} = 0$ and the long range plate repulsion vanishes (dashed gray lines). σ_{coex} denotes the charge of the salting-in/salting-out transition (dashed light blue lines). The minimal free energy is realized by the charge for which the surface potential vanishes $\Phi(0) = 0$ (black dashed dotted lines in (B, C)). The black dotted lines in (A, D) indicate the crossover from repulsion to attraction in the region of partial overlap of the ion-surface interaction potentials.

small D. The plates repel each other because the system tries to maximize the favorable interactions between plates and ions. However, the free energy minimum occurs at a finite separation ($2D = b$) where the additivity of the ion-surface potentials leads to the most favorable ion-surface interaction. Making the surface charge gradually more negative in Fig. 5.7A increases F and for $\sigma_{\mathrm{surf}} < \sigma_{\mathrm{coex}}$ = - 0.035 e/nm^2 the equilibrium plate separation is shifted to infinity. At the coexistence surface charge σ_{coex}, the system changes from salting-out to salting-in, i.e., the bound state (D finite) has the same free energy as the dissociated state (D infinite). The results are more complex for positive surface charge in Fig. 5.7B: For small values of σ_{surf} the free energy decreases. At a critical value $\sigma_{\mathrm{crit}} = 0.145$ e/nm^2 the surface charge compensates the anion adsorption, such that the electrostatic potential Φ vanishes for $D > b$ and the effective surface charge is zero. The effective surface charge resulting from specific ion adsorption and the external surface charge on the plates is defined as

$$\sigma_{\mathrm{eff}} = \epsilon\epsilon_0 \kappa \Phi(b) e^{\kappa b} \tag{5.47}$$

where the Debye screening length κ^{-1} is defined by $\kappa = \sqrt{2q^2 c_0 / \epsilon\epsilon_0 k_B T}$. For $\sigma_{\mathrm{surf}} > \sigma_{\mathrm{crit}}$ the free energy increases but the bound state is stabilized even further with respect to the unbound state.

We now turn to the case of anion repulsion, $V_0^- = +1 k_B$T. For uncharged surfaces (black curve) in Fig. 5.7C, D the free energy is minimal at contact ($D = 0$) as expected. Thus, the system free energy is minimized when the unfavorable ion-surface interaction is eliminated altogether. This minimum shifts to finite plate separation for arbitrarily small but finite surface charge due to the ionic osmotic pressure. This means that the bound state incorporates solvent as long as the surface charge is non-zero, a fact that is well known from protein crystallization studies [164]. Both for negative σ_{surf} in Fig. 5.7C and positive σ_{surf} in Fig. 5.7D the free energy minimum at finite plate separation is destabilized with growing surface charge until at σ_{coex} salting-in is initiated. The critical surface charge denoting the long-ranged instability is σ_{crit} = - 0.045 e/nm^2.

5.3.3. Salting-in/Salting-out Phase Diagrams

Fig. 5.8 shows the stability diagram, resulting from the free energy difference between the free energy minimum at finite and at infinite plate separation. Fig. 5.8A shows the stability diagram for constant salt concentration $c_0 = 100$ mM as a function of the anion-surface interaction strength V_0^- and surface charge σ_{surf}. Fig. 5.8B, C show the stability diagram for constant $V_0^- = -0.5$ k_BT or $V_0^- = +0.5$ k_BT in dependence of c_0 and σ_{surf}.

Salting-out, i.e. stably bound plates, are obtained for small surface charges whenever non-zero ion-surface interactions are present. Most surprisingly, plate binding occurs for both repulsive and attractive ion-surface interactions. The presence of additional van der Waals attraction between the plates increases the parameter range over which salting-out is seen (see below).

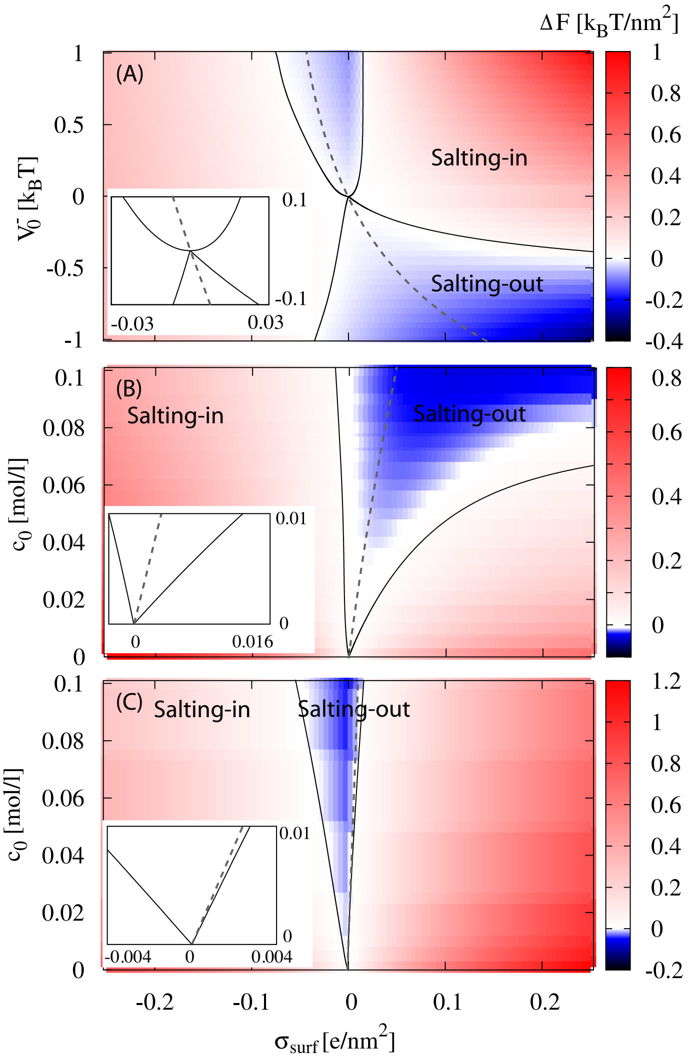

Figure 5.8.: Contour plot of the free energy difference of plate binding. (A) In dependence of the bare plate charge σ_{surf} and the anion-surface interaction strength V_0^- for $c_0 = 100$ mM salt. (B) In dependence of c_0 and σ_{surf} for $V_0^- = -0.5\ k_B$T and (C) $V_0^- = +0.5\ k_B$T; the interaction range is always $b = 1$nm. Solid black lines denote the coexistence surface charge σ_{coex} and correspond to the salting-in/salting-out transition. The dashed lines denote the critical surface charge σ_{crit} on which the effective surface charge σ_{eff} vanishes. The insets show the meeting of the transition lines around $V_0^- = 0$ using the DH approximation.

The salting-in/salting-out transitions (solid lines) merge in the degenerate point $V_0^- = c_0 = \sigma_{\text{surf}} = 0$. The insets show the transition lines in the vicinity of this point from closed-form expressions obtained within the Debye-Hückel approximation. Broken lines denote instability lines σ_{crit} on which $\sigma_{\text{eff}} = 0$ and the long-ranged inter-plate repulsion vanishes.

Van der Waals Attraction

The stability of charged solutes in electrolyte solutions results from a balance between double-layer repulsion and van der Waals attraction. In order to take an additional van der Waals attraction into account we introduce an additional term in the free energy

$$F_{\mathrm{tot}}(D) = F_{\mathrm{A}}(D) + F(D) \tag{5.48}$$

where $F_{\mathrm{A}}(D)$ is the attractive van der Waals interaction energy and $F(D)$ is the free energy according to Eq. 5.44. For two surfaces at separation $2D$ the van der Waals interaction energy is given by

$$F_{\mathrm{A}}(D) = -H/(12\pi(2D + 2a_0)^2) \tag{5.49}$$

where H is the Hamaker constant and a_0 is a contact parameter.

For the Hamaker constant, we take the value $H = 2.2 \times 10^{-21}$ J as appropriate for silica surfaces [118]. The result is shown in Fig. 5.9 for anion repulsion $V_0^- = 1k_B\mathrm{T}$ and interaction range $b = 1$ nm for different values of the contact parameter a_0. For $a_0 = 0$ the van der Waals interaction and therefore the total free energy diverges at $D = 0$. For small a_0 the parameter range over which salting-out is observed, is increased.

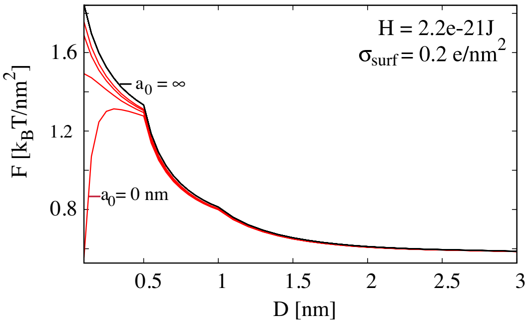

Figure 5.9.: Free energy per area for constant anion adsorption $V_0^- = 1\ k_B\mathrm{T}$, $V_0^+ = 0$ and interaction range $b = 1$ nm with an additional attractive van der Waals contribution for charged plates $\sigma_{\mathrm{surf}} = 0.2$ e/nm^2 and 100 mM salt concentration. The parameter a_0 is varied. The values are $a_0 = 0, 0.05, 0.1, 0.15$ nm from bottom to top. The black line denotes the limit of vanishing van der Waals attraction $a_0 \to \infty$.

5.3.4. From Square-wells to Hofmeister Order

We now focus on long-range inter-plate forces and show how direct, indirect and partially reversed Hofmeister series emerge from the model. In order to relate to real ions, we extract the depth $V_0^{\pm}$ and range $b_{\pm}$ of the surface-ion potential for F$^-$, Cl$^-$, I$^-$ and Na$^+$ from MD simulations at an uncharged hydrophobic self-assembled monolayer (chapter 2). The ion-surface interaction potentials at the hydrophobic surface are shown in Fig. 5.10. The range b of the ion-surface interaction potential for the different ions starts at the Gibbs dividing surface z_{GDS} and ends at the point where all ion-surface interaction

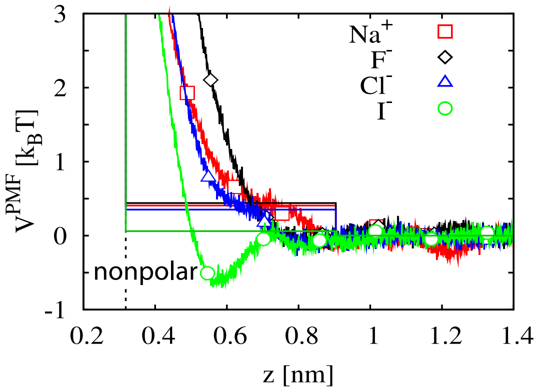

Figure 5.10.: Ion-surface interaction potential obtained by explicit-solvent molecular dynamics (MD) simulations at a hydrophobic CH_3-terminated self assembled monolayer (chapter 2, reference[1]). The Gibbs dividing surface is indicated by the black dashed line. Using Eq. 5.50 yields for the ion-surface interaction strength $V_0^-/k_BT = 0.061$, 0.352, 0.441, $V_0^+/k_BT = 0.407$ for I^-, Cl^-, F^-, and Na^+ shown as solid lines and the interaction range $b = 0.586$ nm.

potentials are smaller than 0.05 k_BT (arbitrary cutoff), yielding b =0.586 nm. The position of z_{GDS} is calculated from the water density profile ρ from simulations (chapter 2, Fig. 2.2A) using the requirement, that the surface excess for water $\Gamma_w = \int_{-\infty}^{z_{\text{GDS}}} \rho(z)\mathrm{d}z + \int_{z_{\text{GDS}}}^{\infty} (\rho(z) - \rho_0)\,\mathrm{d}z$ vanishes.

The interaction strength $V_0^\pm$ is calculated from the requirement that the ion excess Γ_I for the ion-surface interaction potential V^{PMF} obtained by the simulations, which is given by

$$\Gamma_I^{\text{PMF}} = \int_{-\infty}^{z_{\text{GDS}}} e^{-V^{\text{PMF}}(z)/k_BT}\mathrm{d}z + \int_{z_{\text{GDS}}}^{\infty} \left(e^{-V^{\text{PMF}}(z)/k_BT} - 1\right)\mathrm{d}z \tag{5.50}$$

is the same as the ion excess for the corresponding square-well potential

$$\Gamma_I^{\text{square}} = \int_{z_{\text{GDS}}}^{z_{\text{GDS}}+b} \left(e^{-V_0^\pm/k_BT} - 1\right)\mathrm{d}z. \tag{5.51}$$

From the requirement $\Gamma_I^{\text{PMF}} = \Gamma_I^{\text{square}}$ we obtain for the ion-surface interaction strengths $V_0^-/k_BT = 0.061$, 0.352, 0.441, $V_0^+/k_BT = 0.407$ for I^-, Cl^-, F^- and Na^+, which are shown as solid colored lines in Fig. 5.10. On the hydrophobic self-assembled monolayer the anionic surface affinity follows the series $I^- > Cl^- > F^-$, i.e. I^- is least repelled from the surface.

Fig. 5.11A shows in the σ_{surf}-c_0 plane the instability lines σ_{crit} defined by $\sigma_{\text{eff}} = 0$ for the three salt solutions NaI, NaCl, and NaF. Due to the larger surface affinity of iodide, the instability line for I^- occurs at a larger σ_{surf} compared to Cl^- or F^-. In the spirit of the original Hofmeister classification, the three salts can be ordered according to their efficiency in stabilizing charged objects by comparing the magnitude of the effective surface charge σ_{eff}. For large negative σ_{surf} (bottom area) we find $|\sigma_{\text{eff}}^I| > |\sigma_{\text{eff}}^{Cl}| > |\sigma_{\text{eff}}^F|$, the normal (or direct) Hofmeister series; in other words, iodide is the

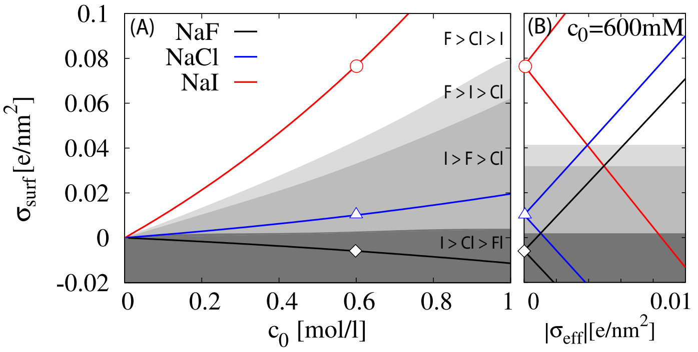

Figure 5.11.: Hofmeister series diagram using the adjusted square-well potentials for I^-, Cl^-, F^-, and Na^+. (A) Instability lines defined by $\sigma_{\text{eff}} = 0$ for NaI (red), NaCl (blue), NaF (black) in the σ_{surf}-c_0 plane. Shaded areas denote regions featuring direct, reversed and two partially reversed series, based on the ordering of $|\sigma_{\text{eff}}|$. (B) Lines denote $|\sigma_{\text{eff}}|$ for NaI, NaCl, NaF in dependence of σ_{surf} for constant $c_0 = 600\text{mM}$. Line intersections signal a change of the ordering in the ionic series.

most stabilizing ion in that situation. As σ_{surf} increases we encounter two intermediate partially reversed series (denoted by the shaded areas in Fig. 5.11) and for large positive σ_{surf} the fully reversed indirect series $|\sigma^F_{\text{eff}}| > |\sigma^{Cl}_{\text{eff}}| > |\sigma^I_{\text{eff}}|$ is obtained, in agreement with the experimental classification of proteins and colloids [69, 74] and previous modeling results (chapter 2, reference [1]). Fig. 5.11A suggests that a change in the ion ordering can be induced by a surface charge variation but also by a change in salt concentration, as indeed observed experimentally [69]. Fig. 5.11B displays the relation between σ_{surf} and σ_{eff} for $c_0 = 600\text{mM}$ and illustrates that a change in the ionic ordering corresponds to the crossing of $|\sigma_{\text{eff}}|$ for two different ions.

5.4. Conclusion

In the resent past, various theoretical models and simulations have been developed to predict the effective interaction between surfaces that specifically interact with ions, ranging from simple heuristic models to explicit water MD simulations. Due to the complexity of the necessary calculations all previous attempts are restricted to only a few parameter sets. Therefore, no deeper understanding of the mechanism underlying Hofmeister effects could be gained and the reversal of the series remained unexplained. In this chapter we introduced a simple and analytically solvable model for specific ion-surface interactions of finite range. Using a analytically solvable model allows to perform a global mean-field analysis for the interaction of two ion-adsorbing charged plates. We present stability diagrams of the equilibrium configuration relevant for small quickly equilibration objects like proteins. The large-distance inter-plate pressure, relevant for the coagulation kinetics of large colloidal objects, undergoes Hofmeister order.

The stability diagrams demonstrate the coupling of long-ranged electrostatic and short-ranged entropic and depletion effects. Salting-out occurs for infinitesimally small ion-plate repulsion and attraction with an equilibrium plate separation that is always finite for non-vanishing surface charge. Therefore, binding of charged surfaces involves finite surface separation including bound water, a result that is well known from numerous protein crystallization studies. The case of vanishing ion-surface potential is marginally unstable and corresponds in the phase diagram to the crossing of salting-in/salting-out transition lines.

By comparing the inter-plate pressure at large-separations of different ions, the direct and indirect Hofmeister series are reproduced in agreement with experiments. A simple mechanism for complete and partial series reversal induced by surface charge as well as salt concentration variation is demonstrated. Due to the generality of the results, finite-range square-well ion-plate potentials govern the mechanism by which ion-surface interactions induce ion specific phenomena.

Chapter 6

The Role of Surface Hydrophobicity in Bioadhesion

6.1. Introduction

6.1.1. Motivation

Protein-surface interactions are of high importance in fields ranging from bionanotechnology to biomedical engineering. Gaining control over nonspecific adsorption of proteins at surfaces is fundamental in technologies involving contact of synthetic surfaces with biological fluids. Examples include biosensors monitoring the adsorption of charged proteins [77], sensitive solid-phase immunoassays retaining selectivity even at large serum protein concentrations [78], solid-phase supports for the growth of adhered cells [79] or the initial stage of blood clotting involving adsorption of certain, large proteins to injured vessel walls [80]. Moreover, understanding how to prevent the adsorption of proteins to surfaces is the ultimate goal for designing biocompatible implants and non-fouling surfaces. Basic research can provide insight into the adhesion mechanism and help to develop a deeper understanding in order to determine surface properties that are able to inhibit the adsorption of fouling species or at least reduce the adsorption strength such that the organism can be removed easily by shear force [82].

Various surface properties have been investigated during the past years. An assortment of surface properties which were shown to be related to adsorption resistance include the type of hydrogen bonding at the surface where hydrogen-bond acceptors but not donors are adsorption resistant [83], physical properties such as the sign and density of surface charges [84] as well as the surface energy, commonly measured by water contact angles. The interfacial tension of water and a solid shows an influence on the adsorption of macromolecules which is related to the *Berg limit* [85]. The Berg limit [86] defines the transition from hydration repulsion to hydrophobic attraction at a contact angle of $\Theta \approx 65°$ where repulsive hydration forces are commonly explained by the structuring of water molecules at the surfaces [165, 166]. Above the Berg limit, i.e. for hydrophobic surfaces, the surface becomes attractive to adhesion while below, i.e. for hydrophilic surfaces, the interaction becomes negligible [85]. For example on densely packed self-assembled monolayers (SAMs) consisting of hexa(ethylene glycol)-containing alkanethiols the attachment/adsorption of cells and proteins increases with increasing contact angle for surfaces with contact angles larger than about 60° [167].

The adsorption resistance of ethylene glycol brushes is known and well explained by the steric repulsion theory [168, 169]. The most prominent examples for surface coatings providing an adsorption resistant environment that are used in the biomedical field are oligo- and poly(ethylene glycol) (OEG and PEG) functionalized surface films [81, 168, 170]. OEG and PEG are chemically inert, water soluble, non-toxic oligomers or polymers with the molecular formula $C_{2n}H_{4n+2}O_{n+1}$. The attachment of cells and proteins is independent of the end-group in the case of PEG but shows a dependence on the number of EG units and their configuration in the case of OEG [170, 171]. Adsorption resistance of these surfaces is attributed to the stability of the interfacial water preventing direct contact between the protein and the surface [171]. Similarly, the settling and attaching of bacteria and zoospores increases with increasing contact angle on mixed SAMs containing hydroxyl- and methyl-terminated alkanethiols [172, 173]. Experimentally measured adsorption free energy of peptides at different SAM surfaces show a similar trend, i.e. a linear correlation between the hydrophobicity of the surface measured by water contact angles and the adsorption free energy. The adsorption energy is largest on the most hydrophobic CH_3-terminated SAM and vanishes on the most hydrophilic OH-terminated SAM [174]. In contrast, experiments measuring the adsorption strength using shear flow show the opposite trend e.g. for the diatom Amphora, i.e. a stronger adhesion on hydrophilic OH-terminated SAMs [173]. The higher adsorption strength might be related to shear induces adsorption, which is well understood for the von Willebrand factor [80], or might be explained in the context of catch bonds [175].

6.1.2. Outline

The first step in a bottom-up approach to understand complex biomolecule-surface interactions is to focus on a simple model system consisting of the building blocks of proteins - the amino acids. A qualitative insight of peptide-surface interactions can be gained by using solvent-implicit MD simulations [176] while solvent-explicit MD simulations allow a quantitative understanding of peptide-surface interactions [87, 88] and enable an identification of the main contributions in the desorption process [89, 90]. However, to the best of our knowledge, no comprehensive study has been performed in the literature to investigate the adsorption behavior of a variety of peptides at different surfaces using MD simulations with explicit water.

In order to fill this gap, we investigate the desorption of 9 homopeptides, differing in their side-chain hydrophobicity, from hydrophobic CH_3-terminated and hydrophilic OH-terminated SAMs by using a combination of explicit-solvent MD simulations and experimental single-molecule force spectroscopy results. SAMs find increasing application in biofouling research since the surface properties including surface energy can be tailored in a well defined and reproducible fashion by using different functional end-groups. The analysis of the involved energetics shows that at hydrophobic surfaces not only water-structure effects and dispersion interactions contribute significantly to the desorption forces. The total desorption energy results from a mutual cancellation of individual contributions among water, peptide and surface. It follows that the free energy of adsorption increases with increasing hydrophobicity of the peptide in a non-monotonic fashion.

The results predict that the adsorption of each type of residue is energetically favorable on methyl-terminated surfaces. The adsorption is entropy dominated for very hydrophobic residues while it is energy dominated for mildly hydrophobic amino acids like glycine. In contrast, on the hydrophilic OH-terminated SAM the adsorption of peptides independent of their hydrophobicity is inhibited by strongly bound interfacial water, preventing direct peptide-surface interactions.

6.2. Methods

6.2.1. Simulation Details

Molecular dynamics simulations at fixed particle number N, constant ambient pressure $P = 1$ bar, and at constant temperature $T = 300$ K are performed by using the Gromacs simulation package [114]. The SAM consist of a 10 x 8 grid of $C_{20}H_{40}$ molecules with a lattice constant that represents the spacing on a gold (111) surface, yielding a 30° tilt angle of the alkane strands. For the hydrophobic surface we use a terminal CH_3-group while an OH-group is used for the hydrophilic surface. All atoms of the SAMs are kept stationary in the dynamics. The structure of the interfacial water in dependence of density, spatial distribution and angular orientation of the polar hydroxyl groups has been studied previously [177]. The terminal CH_3-group carries small partial charges (C -0.014e). The partial charges on the OH-group are (C, 0.286e; O, -0.734e; H, 0.408e) and are identical to the partial charges used in [1].

We use the homopolypeptides alanine (A), glycine (G), glutamic acid (E), lysine (K), proline (P), phenylalanine (F), asparagine (N), tyrosine (Y), valine (V) and the polypeptide $(GVGVP)_3$ consisting of 3 repeat units. All uncharged homopeptides consist of 12 amino acids and the charged peptides E and K consist of 11 alternating charged and uncharged variants of the residue. Note that even strong polyelectrolytes are only partially charged at low salt concentrations [178] and that charge regulation close to a low-dielectric constant substrate leads to a decrease of the fraction of charged monomers [179]. All amino acid termini are capped to mimic an infinite peptide chain and to prevent interactions of the charged amino- or carboxyl- moieties with the surface. The force field parameters for the peptide and the surface atoms are taken from the Gromos96 version 53A6 force field [107]. Initially, the peptide is placed in the simulation box above the surface before the cell is filled with SPC water. To equilibrate the system, we first perform an energy minimization of the system. In the second step the peptide is accelerated toward the surface by a constant acceleration of 1 nm/ps^2 for 200 ps. In the third step the acceleration is turned off and the system is relaxed by a 10-ps NVT simulation. In the fourth step simulations of 10 ns are done employing the Berendsen scheme with semi-isotropic pressure coupling [180] (NAP$_z$T simulation). The particle-mesh Ewald method is used for the periodic treatment of coulomb interactions, and bonds to hydrogen atoms are constrained by using LINCS [181]. During the NPT relaxation in step four, the peptide adsorbs readily onto the hydrophobic surface. In contrast, most peptides desorb spontaneously during the equilibration from the hydrophilic surface (details are given in the appendix B). For the non-adsorbing peptides we use the last surface adsorbed state from the equilibration as a start configuration for the subsequent pulling simulations. In the pulling simulations mimicking AFM experiments the peptide is pulled vertically away from the surface with constant pulling velocity. The setup is shown in Fig. 6.2D. To manipulate the peptide a harmonic restraint potential with spring constant k = 166 pN/nm is applied on the z-coordinate acting only on the first residue of the peptide and leaving the lateral coordinate unperturbed. The center of the restraint potential is moved with constant velocity v in the z-direction away from the surface. The zero point of the z-coordinate is defined by the position of the surface, i.e. the position of the C-atoms or the O-atoms of the CH_3-terminated SAM or the OH-terminated SAM. The pulling force F is calculated from the extension of the spring. The pulling is done until the peptide is completely desorbed from the surface. Every simulation is repeated at least once with a different starting conformation. Since the pulling velocity is much higher than in experiments we perform in addition to the dynamic simulations static simulations in which the restraining potential is kept at a fixed position for 20 ns. The starting configurations are obtained within the dynamic simulations at $v = 0.1$ m/s pulling rate. The static simulations are done for all elongations from the adsorbed to the desorbed state with a step size of 0.1 nm. The static pulling force is averaged over the last 15 ns in these static simulations discarding the first 5 ns for equilibration.

The internal energy and the different contributions are obtained as time average over the last 15 ns of the static simulations. The errors are determined by block averaging. The energy difference of the surface adsorbed state and the state where the peptide is brought into the stretched configuration is calculated from weighted least squares regression over the different surface separations. Fig. 6.1A, B show the result of the weighted least squares regression for alanine at the hydrophobic surface for the peptide-surface and the total internal energy. The desorption force is obtained as time average over the last 15 ns of the static simulations. The errors of the static force are determined by block averaging. The free energy is obtained by integrating the force along the pulling path

$$F = \int_{z_A}^{z_S} < F > dz \tag{6.1}$$

where z_A and z_S are the surface separations of the adsorbed state and the stretched state and $< F >$ is the weighted average desorption force. Fig. 6.1C shows the desorption force and the free energy A (gray area).

The different surfaces are characterized by calculating the wetting coefficient $\cos\Theta$. We determine the wetting coefficient $\cos\Theta$ from the interfacial tension of the solid-water (γ_{sl}),

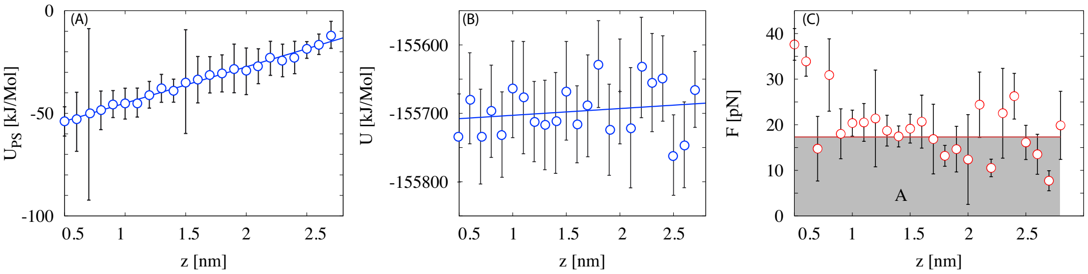

Figure 6.1.: Evaluation of the internal energy and the free energy for alanine at the hydrophobic surface: (A) Internal energy of the peptide-surface interaction and the total internal energy (B) in dependence of the surface separation z (open points) and result of the linear regression (blue line). (C) Mean desorption force obtained from 20 ns static simulations in dependence of the surface separation z. The free energy A is obtained from integration over the desorption path (gray area). The red line is the weighted average desorption force.

solid-vapor (γ_{sv}), and vapor-water (γ_{vl}) interfaces by the Young equation $\cos\Theta = (\gamma_{sv} - \gamma_{sl})/\gamma_{vl}$. The surface tensions are obtained from 5 ns simulations as the difference between the pressure tensor components normal and parallel to the interface. The simulations to determine the wetting coefficient were performed by Susanne Liese, a diploma student in the group of Professor Netz at the TUM.

6.2.2. Experimental Methods

All experiments were performed by Tobias Pirzer and Bizan N. Balzer in the group of Professor Hugel at TUM. In the following the experimental methods are briefly explained.

For SAM preparation the glass slides are sonicated for 15 min in a 2% Hellmanex (Hellma GmbH & Co. KG, Mühlheim, Germany) solution and then twice in ultrapure water. Dried glass slides are coated with a 10 nm chrome nickel layer and a 100 nm gold layer using a vacuum coater (Edwards GmbH, Kirchheim, Germany). After cleaning these slides with RCA solution (v:v:v 5:1:1 of water, 32% ammonia, 35% hydrogen peroxide) at 70 °C for 15 min, they are rinsed with ultrapure water and dried under a stream of nitrogen. Hydrophobic SAMs are prepared by immersing gold coated slides for 12 h in ethanol with 2 mM 1-dodecanethiol. By contrast, mixed SAMs are prepared by immersing gold-coated slides for 12 h in chloroform with 11-mercapto-1-undecanol and 1-dodecanethiol. After incubation, the SAM coated gold slides are rinsed with ethanol and chloroform, respectively, and subsequently rinsed with water. Finally, they are dried under a gentle stream of nitrogen[182].

For contact angle measurements we use a home-built goniometer equipped with a CCD-camera. Both angles of the drop are recorded and determined with the drop analysis plugin [183] for Java-based freeware ImageJ. For determination of the angles, a polynomial is fitted to the edge of the droplet. At the boundary point of the sample and the edge a tangent is fit to the polynomial. The angles are determined between the tangent and sample. The contact angles are determined at least five times at different positions of each sample, before as well as after the experiment.

AFM measurements are performed with a MFP-3D (Asylum Research, Santa Barbara, CA, USA) using silicon nitride cantilevers (MLCT-AUHW from Veeco, Camarillo, CA, USA). The measurements are done in a closed fluid cell at room temperature. During indentation of the functionalized tip (with a dwell time of 1 s) the polymer adsorbed on the surface. The tip is then retracted with a constant velocity of 0.5 μm/s. Force-extension traces are obtained from the deflection piezopath signal as described elsewhere [92]. The traces are taken at least at three different positions on the surfaces used. The measured plateaus represent a steady-state desorption process [89]. Force-extension traces are analyzed by self-written routines using Igor Pro (Wavemetrics). The height of a sigmoidal fit to the plateau region corresponds to the desorption force.

The AFM measurements are done for Poly-D-tyrosine (40-100 kDa), Poly-L-lysine (30-70 kDa) and Poly-L-glutamic acid (50-100 kDa, Sigma-Aldrich, Germany).

6.3. Results and Discussion

6.3.1. Equilibration of Polyalanine

Fig. 6.2A-C show force-extension curves for polyalanine at the hydrophobic SAM for three different pulling velocities v obtained by MD simulations. At large pulling velocities, the desorption is clearly under non-equilibrium conditions where different initial configurations or different pulling velocities result in different desorption forces (Fig. 6.2A). With decreasing pulling velocity friction effects diminish and the mean desorption force decreases. The results for the slowest pulling velocity (solid lines in Fig. 6.2C) are in good agreement with the results in the limit of vanishing pulling velocity (open points in Fig. 6.2C obtained by static simulations). Therefore, the dissipative contributions due to friction on the hydrophobic surface is small. Since peptide friction on the hydrophobic surface is small enough not to cause equilibration problems in the simulations, the results can be compared to atomic-force microscope (AFM) experiments even though the pulling rates in the simulations are five orders of magnitude larger. Note that the friction on a hydrophilic surface is orders of magnitude larger due to hydrogen bonding between the peptide and the surface [88]. However, in our simulations the peptides do not adsorb on the hydrophilic OH-terminated SAM and therefore do not cause any equilibration problems. The force-extension curves for all other peptides on the hydrophobic and the hydrophilic surface are shown in the appendix B (Fig. B.1 and Fig. B.2).

The only peptides which show a plateau force at the hydrophobic surface as obtained in the experiments are alanine and glycine. The stronger adsorption of more hydrophobic peptides causes force spikes in the force-extension curves. These fine structures correspond to the molecular fingerprint of the individual amino acids and are averaged out in the experiments. In the following, we focus on alanine due to its well defined plateau force when simulating different surface compositions. Since the plateau force is higher than for glycine, small changes become visible when changing the surface composition.

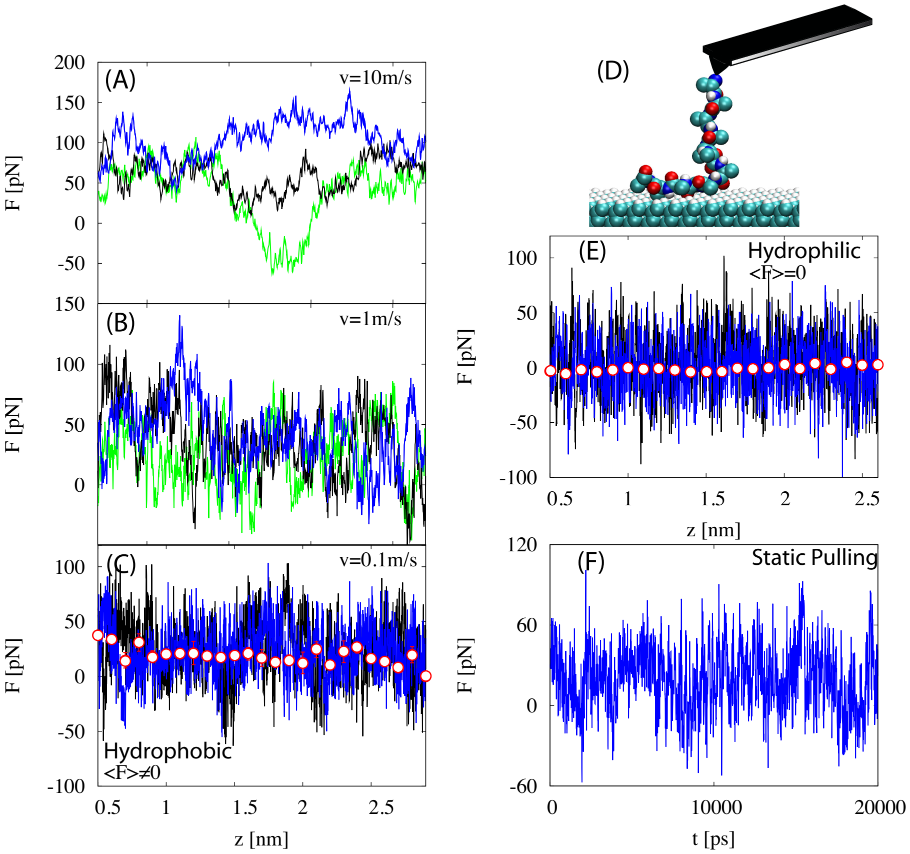

Figure 6.2.: Force-extension curves for polyalanine at the hydrophobic SAM using different initial configurations and different pulling velocities (A) v=10 m/s, (B) v=1 m/s, (C) v =0.1 m/s. Open circles in (C) denote the results from the static simulations. (D) Schematic setup: Simulation snapshot of polyalanine pulled by an attached cantilever away from a hydrophobic CH_3-terminated SAM. Water molecules are not shown for clarity. The simulation snapshot is taken from the static simulation for $z = 1.5$ nm tip separation at time $t = 18.63$ ns. (E) Desorption force of polyalanine for dynamic pulling with v=0.1 m/s at the hydrophilic surface (solid lines). The average desorption force from the static simulations (open circles) is zero. (F) Force as a function of time for the static simulation at the hydrophobic surface for $z = 1.5$ nm tip separation.

6.3.2. Force in Dependence of the Side-chain Hydrophobicity

After having demonstrated that the intrinsic timescale is small and equilibrium can be reached in the simulations, we compare the averaged desorption force from the hydrophobic SAM of the 10 different peptides in Fig. 6.3A. The peptides are ordered according their side-chain hydrophobicity taken from the hydrophobicity scale derived by Black and Mould [184]. This scale uses the hydrophobic fragmental constants from [185] to calculate the partition coefficient of the side-chain of the 20 standard amino acids. The partition coefficient is defined as the logarithm of the ration between the solute concentration in octanol c_{oct} and in water c_{water}. The coefficient can be written as the sum of the hydrophobic fragmental constant f_n and an the number of moieties of a certain species a_n [185]

$$\log(P) = \log(c_{\text{oct}}/c_{\text{water}}) = \sum_n a_n f_n. \tag{6.2}$$

The desorption force increases non-monotonically with increasing side-chain hydrophobicity. In contrast, on the hydrophilic surface (Fig. 6.3B) the desorption force drops to zero independent of the side-chain hydrophobicity. For the glutamic acid (E), we find that the desorption force at the hydrophilic OH-terminated SAM strongly depends on the initial configuration (details are given in the appendix B). Moreover, we find a weak peptide-surface interaction for the tyrosine (Y) leading to an adsorption force of about 4 pN. This weak adsorption force results from interactions of the polar side-chain with the surface. If the side-chain is mutated such that the OH-group is cut off, i.e. replacing tyrosine (Y) by phenylalanine (F), the adsorption vanishes.

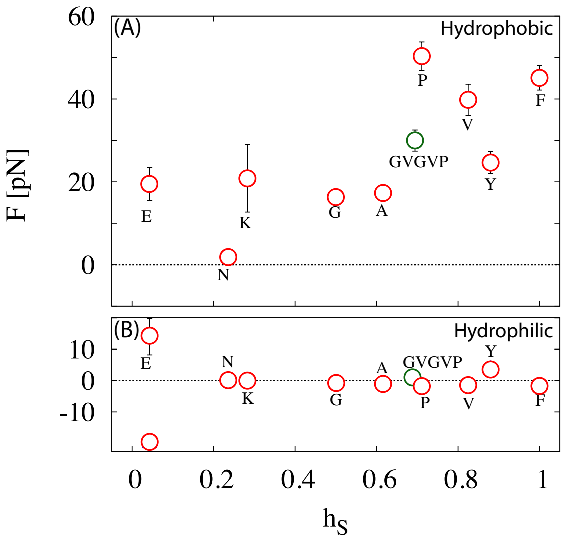

Figure 6.3.: Average desorption force in dependence of the side-chain hydrophobicity at the CH_3-terminated SAM (A) and at OH-terminated SAM (B). The hydrophobicity scale of homopeptides is taken from [184]. The hydrophobicity of GVGVP is the average of the single amino acids.

6.3.3. Additivity

Thermodynamic additivity principles are the foundations of chemistry where free energies consisting of van der Waal interactions, hydrogen bonding, ion-pairing, solvation and hydrophobic interactions for protein and RNA folding, enzyme kinetics or ligand binding are often modeled as sum based on group additivities [186]. However, the additivity assumption is only valid if the components are independent.

In the following, we apply the additivity assumption to the desorption force of more complicated polypeptides consisting of different amino acids and compare it to the sum of the desorption forces of the constituting homopeptides. Fig. 6.4 shows the averaged desorption force for the polypeptide GVGVP (F(GVGVP)) to the average force of the individual amino acids ($F = \frac{1}{5}(2{*}F(\mathrm{G})+2{*}F(\mathrm{V})+F(\mathrm{P}))$). Both results are in very good agreement. Therefore, the contributions of the single amino acids are independent and the results for homopeptides can be used to estimate the desorption forces for polypeptides. Similar results have been obtained for the adsorption of urea at polypeptides [187]. However, care should be taken due to the limitation of the additivity assumption to independent contributions and coupled contributions might become important for complex peptides or proteins e.g. as for structured proteins not all amino acids need to be in contact with the surface.

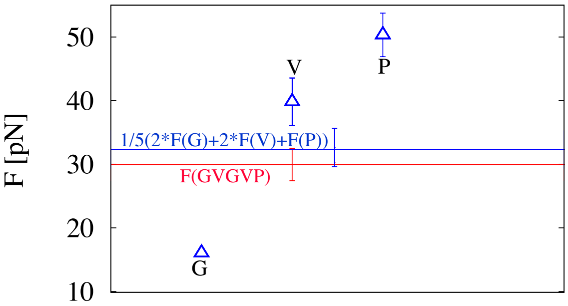

Figure 6.4.: Comparison of the average desorption forces obtained from the additivity assumption (blue line) and result from the simulation of the peptide GVGVP (red line). The average desorption forces of the single constituting peptides are shown as open triangles.

6.3.4. Energy Decomposition

In DLVO theory, the interactions between uncharged objects in solution are only due to van der Waal interactions. However, we now know that solvation effects play an even more important role [188, 189]. Moreover, the single contributions of surface, water and peptide largely cancel one another in the desorption process of spider silk from a hydrophobic diamond surface [89].

In order to gain microscopic insight into the hydrophobic attraction underlying the adsorption of different peptides at the hydrophobic surface, we calculate the different energetic contributions stemming from the interactions between peptide (P), surface (S) and water (W). The energetic contributions are calculated from the total internal energy U that is necessary to bring the peptide from the surface adsorbed configuration into the stretched configuration (see inset of Fig. 6.5) where $U = U_{\mathrm{PP}} + U_{\mathrm{WW}} + U_{\mathrm{PS}} + U_{\mathrm{SW}} + U_{\mathrm{PW}}$. This process closely mimics the AFM experiments.

Fig. 6.5A shows the energetic contributions stemming from the interaction between peptide, surface and water. The total internal energy U, the total free energy A and the entropic contribution $-TS$ are shown in Fig. 6.5B for the homopeptides which show the usual desorption behavior. The peptides E, N and K are excluded from the energy decomposition since they show an unusual desorption process for which the total internal energy is not well defined (details are given in the appendix B). The other peptides are ordered according to increasing side-chain hydrophobicity.

In agreement with previous simulation results [89], the peptide-peptide U_{PP}, water-water U_{WW} and peptide-surface U_{PS} contributions to the internal energy are positive and larger in magnitude than the resulting internal energy U. Therefore, direct van der Waals interactions between peptide and surface and solvation effects are important, as the often neglected peptide-peptide interaction. However, the positive contributions, pushing the peptides out of solutions, are largely canceled by the negative water-surface U_{SW} and the peptide-water U_{PW} contributions, which favor the stretched configuration. If we compare the single contributions of the different peptides, we find that the water-water interaction and the peptide-surface interaction increase with increasing side-chain hydrophobicity (or equivalent with the volume of the side-chain) as expected. In contrast, for the peptide-water interaction and the surface-water interaction one sees the opposite trend, i.e. a decrease with increasing hydrophobicity.

No clear trend for the resulting total internal energy is observed since the contributions show opposite trends and cancel one another and since the peptide-peptide interaction displays a nonlinear dependence on the side-chain hydrophobicity (Fig. 6.5B). Rather, the total energy shows a minimum as a function of the side-chain hydrophobicity that is also observed in the peptide-peptide interaction. Therefore, there is not a single mechanism responsible for the hydrophobic adsorption even though the sum of peptide-surface interaction and the water-surface interaction is roughly equal to the total energy. This means, that in contrast to the common explanations in terms of water structural effects

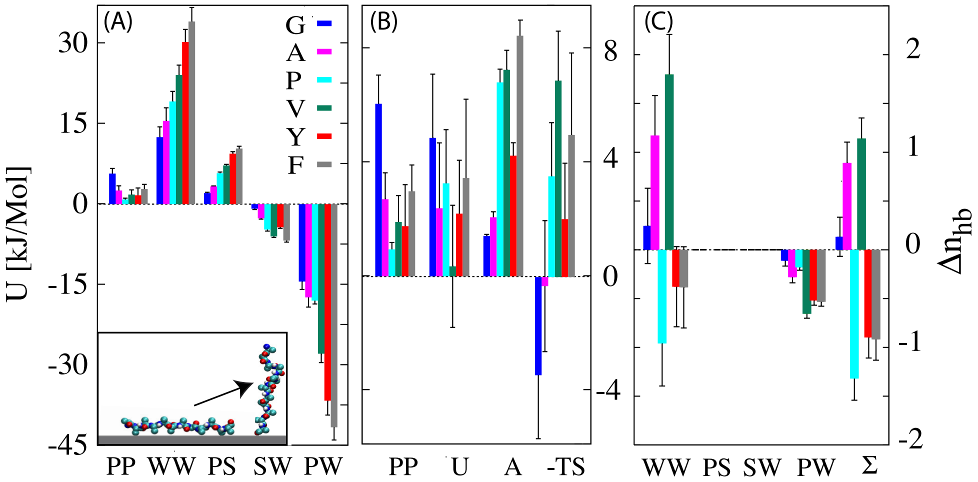

Figure 6.5.: (A) Decomposition of the total internal energy per monomer U of the different homopeptides divided into the single contributions of peptide (P), water (W) and surface (S). The inset shows a snapshot of the surface adsorbed configuration and the stretched configuration. The peptides are ordered according to increasing side-chain hydrophobicity from left to right. (B) Total internal energy per monomer U, free energy of desorption A and the entropic contribution $-TS$ of the desorption process. For a better comparison the peptide-peptide contribution to the internal energy is shown again. (C) Difference in the number of hydrogen bonds $\Delta n_{\mathrm{hb}} = n_{\mathrm{hb}}^{\mathrm{A}} - n_{\mathrm{hb}}^{\mathrm{B}}$ per monomer for the surface adsorbed configuration $n_{\mathrm{hb}}^{\mathrm{A}}$ and the bulk configuration $n_{\mathrm{hb}}^{\mathrm{B}}$.

and dispersion forces alone, all interactions have to be taken into account to quantitatively describe desorption. Moreover, no component can be tuned independently from the others in order to decrease or increase adsorption.

The resulting adsorption free energy for tyrosine $A(Y) = 4.08$ kJ/Mol, glycine $A(G) = 1.37$ kJ/Mol and phenylalanine $A(F) = 8.14$ kJ/Mol are quite close to the experimental values for the adsorption energy per monomer on polystyrene $A(Y) = 2.74$ kJ/Mol, $A(G) = 1.56$ kJ/Mol and $A(F) = 3.66$ kJ/Mol [190]. The reasons for the deviations, especially for phenylalanine, are due to the different surface composition and the additivity assumption underlying the experimental and the theoretical values. The entropy difference $S = (U - A)/T$ is positive for the least hydrophobic amino acids G and A and the system gains entropy in the desorption process, while the entropy is negative and the system loses entropy for the hydrophobic amino acids P, V, Y and F, in agreement with the solvent implicit model for V and F from [176]. The adsorption of each type of homopeptide is energetically favorable at the hydrophobic surface. The adsorption is entropy dominated for the hydrophobic residues while it is energy dominated for the mildly hydrophobic residues G and A.

Fig. 6.5C shows the difference in the number of hydrogen bonds $\Delta n_{\mathrm{hb}} = n_{\mathrm{hb}}^{\mathrm{A}} - n_{\mathrm{hb}}^{\mathrm{B}}$ per monomer for the surface adsorbed configuration $n_{\mathrm{hb}}^{\mathrm{A}}$ and the bulk configuration $n_{\mathrm{hb}}^{\mathrm{B}}$ for the different peptides. At the hydrophobic surface, the only possible contributions to the total difference of hydrogen bonds result from water-water and peptide-water hydrogen bonds. While the number of peptide-water hydrogen bonds is always larger in the bulk configuration, no clear trend is observed for the water-water and the total difference of hydrogen bonds. Adsorption at the hydrophobic is therefore not driven by a maximization of hydrogen bonds in general. In contrast, the maximization of hydrogen bonds is one of the mechanism underlying adsorption resistance, as will be discussed further below.

6.3.5. Why is the Hydrophilic Surface Adsorption Resistant?

The extraordinary strength of hydrogen bonds at the OH-SAM/water interface appears to be the main reason for the adsorption resistance of the hydrophilic surface, preventing the peptides from adsorption due to the stability of the first interfacial water layer, similar to OEG-terminated SAMs [170, 171].

In order to gain insight into the structure of the water molecules at the two surfaces, we show in Fig. 6.6A the water density profile at the CH_3-terminated and the OH-terminated SAM as well as snapshots of the water molecules close to the different surfaces (Fig. 6.6B, C). At the hydrophilic surface, a strongly bound first hydration layer is formed leading to a high density peak close to the surface. The water molecules within this first layer are strongly oriented due to hydrogen bonding with the OH-terminal groups at the surface (Fig. 6.6C). In contrast, a depletion layer of about 0.3 nm is observed at the hydrophobic surface.

At the OH-terminated SAM, we observe that the water molecules in the first hydration layer of the surface form two hydrogen bonds with the surface OH-groups of two neighboring alkane chains (inset of Fig. 6.6C) . The first hydrogen bond occurs between

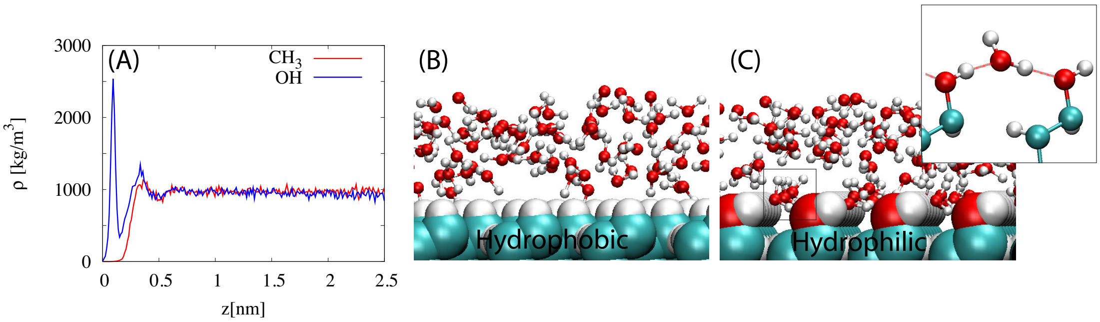

Figure 6.6.: (A) Water density profile at the hydrophobic (red) and the hydrophilic surface (blue). Simulation snapshots of water at the hydrophobic (B) and the hydrophilic surface (C). The inset of (C) shows an enlarged snapshot of one bifurcated hydrogen bond between a water molecule and two OH-surface groups.

the hydrogen of the surface hydroxyl group and the oxygen atom of water, the second one between the hydrogen atom of water and the oxygen atom of the surface hydroxyl group. These bifurcated hydrogen bonds lead to a strongly bound, highly oriented first hydration layer. Moreover, these bifurcated hydrogen bonds and the therefore strongly bound water molecules give rise to a repulsive barrier for the approaching peptides.

In order to probe this barrier, we perform constant force simulations. In these simulations, an additional constant external force $F_{\text{Ext}} = m_i a$, where m_i is the mass of each atom and a is the constant acceleration acting towards the surface, is applied to the peptide in $-z$-direction during a 20 ns NAP$_z$T simulation. For each simulation, the average separation $< z >$ of the peptide from the surface is calculated as mean value of the separation of all atoms, discarding the first 5 ns for equilibration. The free energy of this forced adsorption process is calculated via

$$A(< z >) = \int_{<z>}^{\infty} -F_{\text{Ext}}(< z' >) d < z' > . \tag{6.3}$$

Fig. 6.7A shows the free energy $-A$ per amino acid to bring the peptide from bulk to the surface according to Eq. 6.3 in dependence of the average position $< z >$. Fig. 6.7B shows the gain or loss of hydrogen bonds per amino acid $\Delta n_{\text{hb}} = n_{\text{hb}}^{\text{A}} - n_{\text{hb}}^{\text{B}}$ of the forced adsorbed configurations $n^{\text{A}}(< z >)$ relative to the bulk configuration n_{hb}^{B}. In order to bring the peptide close to the hydrophilic surface a high free energy is required. This process requires breaking of hydrogen bonds since more water-water and water-surface hydrogen bonds can form in the bulk configuration (a detailed comparison of all contributions is given in the appendix B and the single contributions to the hydrogen bond difference is shown in Fig. 6.8 for $< z >= 0.49$ and will be discussed in the next section).

Fig. 6.7C, D show simulation snapshots of alanine at the 100% OH-SAM for two different external forces. For low external forces ($F_{\text{Ext}} = 14.79$ pN) water molecules enter the gap between the peptide and the surface and form one strongly bound layer of hydration. For large external forces ($F_{\text{Ext}} = 739.69$ pN) all water molecules are depleted

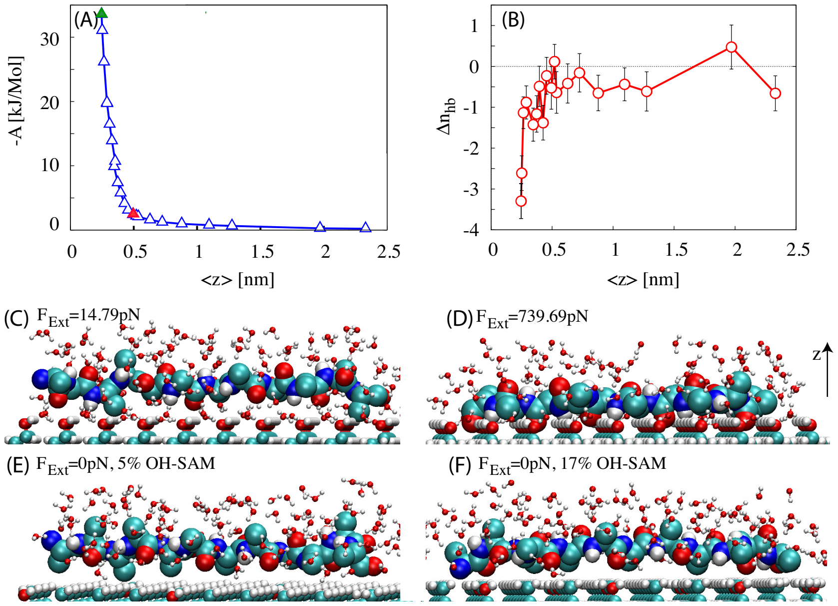

Figure 6.7.: (A) Free energy $-A$ per amino acid to bring the peptide from bulk to the surface according to Eq. 6.3 in dependence of the average position $< z >$. The red triangle indicates the average position using $F_{\mathrm{Ext}} = 14.79$ pN for which the peptide-surface separation is the same as for the peptide adsorbing surface compositions. The green triangle indicates the average position using $F_{\mathrm{Ext}} = 739.69$ pN. (B) Total difference of the number of hydrogen bonds per amino acid $\Delta n_{\mathrm{hb}} = n_{\mathrm{hb}}^{\mathrm{A}} - n_{\mathrm{hb}}^{\mathrm{B}}$ for the surface adsorbed configuration $n_{\mathrm{hb}}^{\mathrm{A}}$ and the bulk configuration $n_{\mathrm{hb}}^{\mathrm{B}}$ in dependence of the average position $< z >$. Simulation snapshot of alanine at the hydrophilic 100% OH-terminated SAM for two different external forces $F_{\mathrm{Ext}} = 14.79$ pN (C) and $F_{\mathrm{Ext}} = 739.69$ pN (D). For low external forces water molecules enter the gap between the peptide and the surface and form one strongly bound layer of hydration. For large external forces all water molecules are depleted from the surface. Simulation snapshots of the equilibrium configuration without external force of alanine at the 5% OH-SAM (E) and the 17% OH-SAM (F). The average peptide-surface separation is about 0.5 nm in (C), (E) and (F). Water molecules within 5 Å of the peptides are shown.

from the surface.

As will be discussed in detail in the subsequent section, peptide adsorption is favored for heterogeneous surface compositions with low OH-surface concentration. In order to compare the results at the adsorption resistant 100% OH-SAM to the other surfaces, we choose the external force $F_{\mathrm{Ext}} = 14.79$ pN. The reason is that for this force the average separation of the peptide from the surface $< z >= 0.49$ nm. This value is close to the values for the peptide adsorbing surface compositions

- 0% OH-SAM: $< z >= 0.48$ nm;
- 5% OH-SAM: $< z >= 0.52$ nm;
- 11% OH-SAM: $< z >= 0.51$ nm;
- 17% OH-SAM: $< z >= 0.49$ nm.

Fig. 6.7E, F show simulation snapshots of the equilibrium configuration without external force of alanine at the 5% OH-SAM and the 17% OH-SAM. Due to the depletion of water at the hydrophobic surface patches, no water molecules enter the gap between peptide and surface.

Using constant force simulations allows to decompose the internal energy at the non-adsorbing hydrophilic surfaces into the the single contributions of water, surface and peptide and to determine the gain or loss of hydrogen bonds in the desorption process. The detailed comparison of the involved energetics of adsorbing and adsorption resistant surfaces provides further insight into the molecular mechanism and will be discussed in the following.

6.3.6. Force in Dependence of the OH-surface Concentration

So far, we have shown that adsorption is favorable at the hydrophobic surface and unfavorable at the hydrophilic surface. We now turn to the dependence of the desorption force on the contact angle. In order to manipulate the water contact angle we use heterogeneous CH_3-/OH-terminated SAMs. In agreement with previous experiments and simulations [172, 177], the contact angle decreases with increasing OH-surface concentration Fig. 6.8A.

The average desorption force of polyalanine is shown in Fig. 6.8A in dependence of the wetting coefficient $\cos\Theta$ for six different OH-surface concentrations obtained by static and dynamic simulations (the force-extension curves are shown in the appendix B, Fig. B.4).

Fig. 6.9 shows the average desorption force of polyglutamic acid, polytyrosine and polylysine in dependence of the water contact angle obtained by AFM experiments. The desorption force for the different peptides decreases slightly upon decreasing the water contact angle (increasing the OH-concentration). Below a water contact angle of about 40°, the force plateau is no longer measurable experimentally, indicating that peptide adsorption is inhibited at large OH-concentrations in close agreement with the Berg limit [85, 86].

Similarly, the desorption force decreases and drops to zero and the surface becomes adsorption resistant in the simulations at OH-surface concentrations larger than 33% (Fig. 6.8A). The decomposition of the total internal energy into the single contributions reveals that the interactions among peptide, surface and water are largely unaffected upon small changes of the OH-surface concentration (Fig. 6.8B). In contrast, at 100% OH-surface concentration the water-water contribution changes sign. The total internal energy is positive for all surface compositions (Fig. 6.8C). The free energy is positive and adsorption is favored for low OH-surface concentrations. At 100% OH-surface concentration the free energy is negative and the surface is adsorption resistant. The repulsion at high OH-surface concentrations is driven by the large entropy gain of the system when the peptide is pushed away from the surface into bulk (Fig. 6.8C).

Fig. 6.8D shows the difference in the number of hydrogen bonds between the adsorbed and the bulk configuration for the different surface compositions. The number of hydrogen bonds between surface and water as well as between peptide and surface is negligible

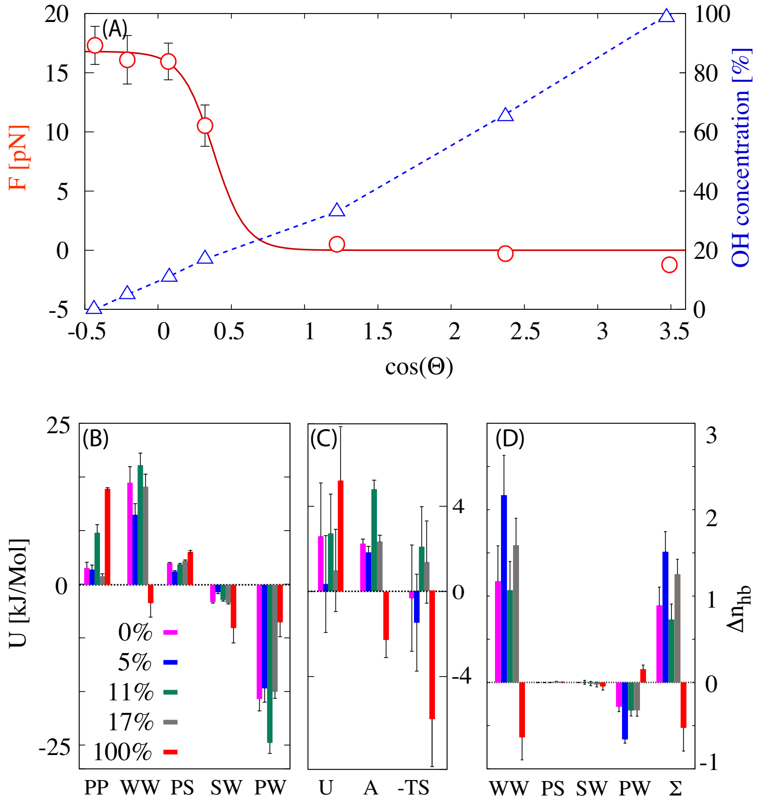

Figure 6.8.: (A) Average desorption force in dependence of the wetting coefficient $\cos\Theta$ obtained by static simulations of polyalanine (red points). Data points are fitted using $a/(\exp(b(\cos\Theta - c)) + 1)$ with $a = 16.8$ pN, $b = 9.17$ and $c = 0.38$ (red solid line). The relation between the OH-surface concentration and the wetting coefficient $\cos\Theta$ is shown by blue triangles (dashed blue line is to guide the eye). The simulations to determine the wetting coefficient were performed by Susanne Liese. (B) Energy decomposition of the total internal energy per monomer for different surface compositions. (C) Total internal energy per monomer U, free energy of desorption A and the entropic contribution $-TS$. (D) Difference in the number of hydrogen bonds $\Delta n_{\text{hb}} = n_{\text{hb}}^{\text{A}} - n_{\text{hb}}^{\text{B}}$ per monomer for the surface adsorbed configuration n_{hb}^{A} and the bulk configuration n_{hb}^{B}. For the highest OH-surface concentration (100%) we use an external force $F_{\text{Ext}} = 14.79$ pN to obtain the same peptide-surface separation as for the other surfaces ($< z >= 0.5$ nm). Hydrogen bonds are calculated according to the distance angle-criterion for distances smaller than 0.35 nm and angle smaller than 30°.

at small OH-concentrations. The hydrophobic CH_3-terminated side-chain of polyalanine blocks hydrogen bonds between the backbone and the OH-surface groups. For alanine the average number of hydrogen bonds per residue at 11% OH-surface concentration is $n_{\text{hb}}^{\text{A}}(PS) = 0.01$. Additional simulations of polyglycine at 11% OH-surface concentration yield an average number of $n_{\text{hb}}^{\text{A}}(PS) = 0.1$ hydrogen bonds per residue between peptide and surface. Still, this contribution is negligible compared to the water-water or peptide-water contributions to the total number of hydrogen bonds. For peptide adsorb-

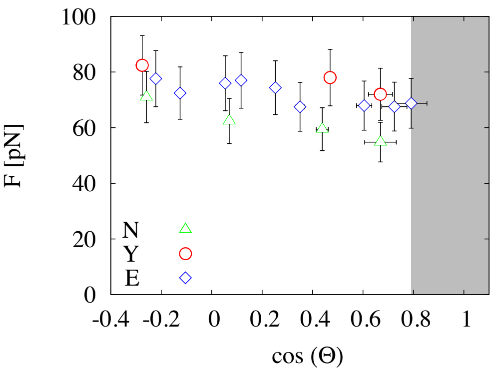

Figure 6.9.: Experimental results performed in the group of Professor Hugel by Tobias Pirzer and Bizan N. Balzer (with permission). Average desorption forces of polylysine (green triangles) and polytyrosine (red circles) and polyglutamic acid (blue diamonds) from heterogeneous SAMs in dependence of the wetting coefficient $\cos\Theta$ in 1 M NaCl. Each data set was taken with a different cantilever. Thus, the statistical error was estimated to have a maximum value of 13% [182]. The gray area denotes the region of vanishing peptide adsorption.

ing surface compositions the system gains hydrogen bonds in the adsorbed configuration.

For the non-adsorbing surface the gain of hydrogen bonds is larger in the bulk configuration. The main contributions inducing this change are the water-water and the water-surface interactions. Adsorption resistance is therefore driven by entropy and the maximizing of the number of hydrogen bonds.

6.4. Conclusion

Studying the desorption of single peptide chains at well characterized SAMs with different functional end-groups by a combination of simulation and experimental techniques, is an ideal starting point to gain microscopic understanding of peptide adsorbing and adsorption resistant surfaces. Such systems allow to identify the dominant contributions responsible for adsorption and adsorption resistance.

The results clearly demonstrate that the total internal energy results from a mutual cancellation of individual contributions among water, peptide and surface. A direct consequence of this cancellation and opposite trends of the single energy contributions is the non-monotonic dependence of the desorption force on the peptide hydrophobicity.

Adsorption is energetically favorable at the hydrophobic surface and can be either entropy or energy dominated. Adsorption is unfavorable for each type of homopeptide at the hydrophilic surface. The adsorption resistance at the hydrophilic surface results from strongly bound interfacial water, inhibiting direct peptide-surface interactions. Adsorption resistance is driven by the gain of entropy and hydrogen bonds.

Understanding peptide adsorption can be seen as first step in a bottom-up approach for describing and predicting protein adsorption at a larger scale. Understanding the basic mechanism contributes to the design of bioactive surfaces and to the control of protein adsorption and cellular response.

Chapter 7

Summary and Outlook

In this thesis, we develop a clear molecular understanding of ion specific effects and identify the main contributions underlying peptide-surface interactions. We demonstrate that the combination of atomistic simulations and Poisson-Boltzmann theory is an excellent tool to gain microscopic insight and to bridge from computational results to macroscopic experimentally accessible properties. We show that the fundamental physical correlations underlying ion specificity can be merged into a general analytical theory. Furthermore, we investigate peptide-surface interactions using atomistic simulations and single-molecule experiments in a close collaboration with the group of Professor Hugel at TUM. We identify the mechanism underlying peptide adsorption and adsorption resistance.

In chapter 2, we introduce a two-scale modeling approach to investigate anion specific effects at surfaces of varying surface charge and polarity. In this approach, single ions are simulated with explicit water at atomistically resolved planar surfaces, and the resulting potentials of mean force are imported into mean-field Poisson-Boltzmann theory. The merit of this approach is, that the discrete nature of water and the surface polarity are treated realistically, especially the changes of ion and surface hydration as an ion approaches the surface. The reversal of the Hofmeister series appears already on the single ion level when changing the nature of the surface from hydrophobic to hydrophilic. The Hofmeister phase diagrams display four regions of direct, altered, and inverse series and capture the full spectrum of experimentally observed phenomena.

In chapter 3, the anionic Hofmeister series is complemented by the cationic series. We extend the two-scale modeling approach to more realistic surfaces, consisting of hydrophobic and hydrophilic surface patches, similar to proteins. The resulting interfacial tension increments agree quantitatively with experimental data, capture the Hofmeister trend, especially the anomaly of lithium, and justify our choice of ionic force fields. We demonstrate that the preferred adsorption of large ions at hydrophobic surfaces in combination with the opposite charge of anions and cations unravel the long standing mystery why small anions but large cations are more efficient in the precipitation of proteins. We successfully explain the surface affinity of large anions by interface-adapted hydrophobic solvation theory. We provide evidence that the surface interaction of cations is more complex than for anions due to the in general smaller size and stronger hydration of cations, leading to a failure of the simple solvation theory. Especially, on hydrophilic surfaces, we demonstrate that cation-surface interactions go beyond a simple adsorption/repulsion behavior. This complexity can lead to small differences in macroscopic quantities and to a multiplicity of alterations in the Hofmeister series in dependence of surface charge and bulk salt concentration. Nevertheless, the results reveal that cations can have as strong an effect as anions on macroscopic quantities in agreement with experimental observations.

In chapter 4, we investigate ion binding to ionizable carboxyl surface groups. We demonstrate that at surfaces containing carboxylates, sodium acts as strong denaturant, supporting the explanation that sodium needs to be pumped out of the cell, where denaturation might weaken or hinder the function of proteins. In the presence of ionizable surface groups, the Hofmeister series is determined by the competition of direct ion binding to charged groups and adsorption at uncharged surface patches. Furthermore, we show that the ion-surface interactions strongly depend on the degree of dissociation and are therefore sensitive to the pH. Especially at high pH, ion binding to carboxylate groups becomes increasingly important.

In chapter 5, we merge the fundamental physical correlations of the in general complex ion-surface interactions into a generic analytical continuum model. Using a model, in which ions interact with surfaces via square-well potentials of finite depth and range, enables us to perform a global analysis in the complete parameter space of salt concentration, surface charge, and ion-surface affinity. We present stability diagrams which display the salting-in/salting-out behavior that is characteristic for protein precipitation. Salting-out occurs both for repulsive and attractive ion-surface interactions, and always involves a finite surface separation including bound water, a result that is well known from numerous protein crystallization studies. Moreover, we demonstrate that our model can be easily adjusted to realistic ion-surface interactions obtained from simulations. By comparing different ions, the direct and indirect Hofmeister series are reproduced in agreement with experiments. The generality of the results shows that the mechanism underlying ion specific phenomena is captured using finite-range square-well ion-surface potentials.

In chapter 6, we present a combination of experimental and simulation techniques to investigate peptide-surface interactions. In accordance with single-molecule experiments, we develop a fully atomistic description of the complete system. To characterize peptide-surface interactions, we determine the desorption force of single peptide chains from well characterized flat self-assembled monolayers with different functional end-groups. The results clearly demonstrate that the total internal energy results from a mutual cancellation of individual contributions among water, peptide, and surface. A direct consequence of this cancellation is the non-monotonic dependence of the desorption force on the peptide hydrophobicity. We show that the adsorption is energetically favorable at the hydrophobic surface and can be either entropy or energy driven. The adsorption is unfavorable for each type of peptide at the hydrophilic surface. The adsorption resistance at the hydrophilic surface results from strongly bound interfacial water, inhibiting direct peptide-surface interactions. We demonstrate that adsorption resistance is driven by the maximization of entropy and the gain of hydrogen bonds. The results presented here, can be seen as first step in a bottom-up approach to describe and predict protein adsorption at a larger scale. The microscopic insight into the basic mechanism contributes to the systematic design of bioactive surfaces and tissues and to the control of protein adsorption and cellular response.

In this thesis, we provide evidence that the question about the origin of the Hofmeister series can be answered in simple model systems. However, this answer cannot be given in terms of a single parameter for one type of ion that describes its specific effect under all circumstances. Rather, ion specific phenomena depend on the combination of ionic and surface properties leading to a diverse spectrum of direct, altered and reversed Hofmeister series.

The next logical steps are to extend the map of possible ion-macromolecule interactions, to improve the existing approach and to bridge from simple model systems to complex biological systems. An accurate description of any Hofmeister phenomenon must include all different interactions from water, surface and ion. Concerning the latter two, our work focuses on a small spectrum of biologically relevant groups and on monovalent, spherical ions. The large variety of biological surfaces, for instance the building blocks of proteins, protein backbone amide groups or different headgroups of biological membranes, provide numerous possibilities for further atomistic modeling. In addition, divalent cations like magnesium and calcium or complex ions like the guanidinium and non-spherical ions like thiocyanate are in the focus of protein science due to their strong effects on protein denaturation [12, 31]. Further research for those ions requires, first of all, a proper optimization of the ionic force field to reproduce thermodynamic bulk properties [68, 109]. Based on our results, we expect that the interaction of multivalent and multi-atomic ions with surfaces is complex, leading to a broad range of new and interesting phenomena. In order to make our model applicable to large salt concentrations, non-electrostatic ion-ion interaction potentials, that are important in dense systems, will certainly be of use in the future [109, 149]. In order to bridge from simple model systems to complex biological surfaces, we establish two approaches to include the interaction of ions with different nonpolar, polar and charged surface groups. For the future, a joint approach using such coarse-grained modeling and molecular dynamics simulations of atomistically resolved biological surfaces like proteins [67], should be used. In combination with tailored experiments [118] and surface-specific techniques [38], this will provide further insight into the origin of the Hofmeister series in complex biological systems. As in the field of protein folding, the ultimate goal is to predict salting-in and salting-out including unfolding by knowing the primary structure, only.

In a general framework, the mechanism underlying ion specific phenomena is captured using finite-range square-well ion-surface potentials. The theory presented here, relies on the additivity assumption for the ion-surface interaction potentials. Although this is a good starting point, this assumption should be compared to the other limiting case of non-additivity. In addition, a more general approach of unequal ranges of ion-surface interactions for anions and cations can extend the scope of potential application. We expect, that this approach might provide an explanation of the controversially discussed Jones-Ray effect [38, 42].

Designing adsorption resistant surfaces is an active field of research with important technological and medical applications. In this work, we provide insight into the adsorption resistance of self-assembled monolayers with terminal hydroxyl-groups. Whether such surfaces are an alternative to ethylene glycol brushes [168, 169] or oligo- and polyethylene glycol functionalized surface films [81, 168, 170], depends on their stability and long-term durability in aqueous environment. In the light of marine biofouling, further simulations with for instance DOPA, a key compound in the formation of marine adhesive proteins, might be useful in order to verify adsorption resistance in a biological environment. Biofouling is a rich field of primarily experimental research. New and interesting approaches toward non-toxic anti-fouling surfaces exist. Especially, bio-inspired surfaces including for example the nanoscale roughness of shark skin [191] or self-healing surfaces [192] provide exciting possibilities for further simulations and new challenges for atomistic modeling.

This thesis is my contribution to 'get specific about ion specific effects' and to the inspiring field of protein science.

Chapter 8

Danksagung

An dieser Stelle möchte ich mich bei all denjenigen bedanken, ohne die diese Arbeit nicht möglich gewesen wäre.
An erster Stelle gilt mein Dank meinem Doktorvater, Roland Netz, an dessen Lehrstuhl ich diese Arbeit verfassen durfte. In der angenehmen Arbeitsatmosphäre am Lehrstuhl konnte ich viel von meinem Doktorvater lernen und durch die große Freiheit bei meiner Forschung eigne Ideen einbringen. Neben den zahlreichen Konferenzteilnahmen hatte ich zudem die Möglichkeit während einem Aufenthalt in San Diego und Berkeley unsere Forschung vorzustellen und neue Kontakte zu knüpfen. In besonders guter Erinnerung werde ich die zahlreichen Exkursionen, Sommer- und Weihnachtsfeste und die jährliche Winterschule behalten.
Professor Martin Zacharias danke ich dafür, sich Zeit zu nehmen und meine Arbeit zu prüfen.
Ich bedanke mich ganz herzlich bei Sonja Ortner, unserer Sekretärin und guten Seele des Lehrstuhls. Ein herzliches Dankeschön geht an Dominik Horinek, dafür dass er all sein Wissen und seine Erfahrungen über MD Simulationen mit mir geteilt hat und mir bei Problemen stets mit Rat und Tat zur Seite zu gestanden ist. Bei meinen ehemaligen Bürokollegen Immanuel Kalcher und Alex Herz bedanke ich mich für ein sehr angenehmes Büroklima und zahlreiche fachliche und nichtfachliche Diskussionen. Bei allen Mitgliedern von T37 bedanke ich mich ganz besonders für die tolle Arbeitsatmosphäre. Insbesondere danke ich Maria für alle Ionen Diskussionen und die vielen hilfreichen Kommentare zu meiner Arbeit. Vielen Dank an Tobias, Susanne und Bizan für das Engagement bei unserem Peptid Projekt. Ich bedanke mich bei allen IDK-Studenten für die schöne Zeit bei den zahlreichen Workshops und Seminaren. Insbesondere bedanke ich mich bei Julia Zimmermann und Marilena Pinto für die großartige Unterstützung. Für finanzielle Unterstützung danke ich dem Elitenetzwerk Bayern für das Stipendium im Rahmen des Internationalen Doktorandenkolleg NanoBioTechnologie und das Forschungsstipendium.
Ich danke meinen Freunden und meiner Familie, die mich durch alle Höhen und Tiefen

der Promotion begleitet haben. Insbesondere danke ich Jan Neumann für die liebevolle Unterstützung, für seine Geduld und das Vertrauen, das er in mich und meine Fähigkeiten setzt. Meiner Schwester Jasmin danke ich dafür, dass sie mir stets zur Seite steht und mich in allen Fragen bezüglich der „Protein-Kolloide“ unterstützt und bestärkt. Meinen Eltern Brigitte und Klaus danke ich dafür, dass sie mich während meines gesamten Studiums und der Promotion stets unterstützt und ermutigt haben und immer an meinen Erfolg glauben.

Parts of this thesis have been published in or have been submitted to peer-reviewed journals. A part of this thesis is published in a book chapter and manuscripts for contributions in peer-reviewed journals are in preparation:

1. N. Schwierz, D. Horinek and R. R. Netz. Reversed Anionic Hofmeister Series: The Interplay of Surface Charge and Surface Polarity. *Langmuir*, 26(10):7370–7379, **2010**.
2. J. Dzubiella, M. Fyta, D. Horinek, I. Kalcher, R. R. Netz and N. Schwierz. *Specific Ion Effects*, in Ion-Specificity: From Solvation Thermodynamics to Molecular Simulations and Back, (ed. by W. Kunz, World Scientific Publishing, Singapore), 1st edition, **2010**.
3. N. Schwierz and R. R. Netz. Effective Interaction between two Ion-adsorbing Plates: Hofmeister Series and Salting-in/Salting-out Phase Diagrams from a Global Mean-field Analysis. *Submitted to Langmuir*, **2011**.
4. E. R. A. Lima, M. Boström, N. Schwierz and F. W. Tavares. Attractive Double-Layer Forces between Neutral Hydrophobic and Neutral Hydrophilic Surfaces. *Phys. Rev. E*, 84(6):061903, **2011**.
5. N. Schwierz, D. Horinek and R. R. Netz. Comparison of Anionic and Cationic Hofmeister Effects. *To be published*, **2011**.
6. N. Schwierz, D. Horinek and R. R. Netz. Specific Ion Binding to Charged Surface Groups. *To be published*, **2011**.
7. N. Schwierz, D. Horinek, S. Liese, T. Pirzer, B. N. Balzer, T. Hugel and R. R. Netz. The Role of Surface Hydrophobicity in Bioadhesion. *To be published*, **2011**.
8. S. Kienle, S. Liese, N. Schwierz, R. R. Netz and T. Hugel. The Effect of Temperature on Single Polypeptide Adsorption. *Accepted in Chem. Phys. Chem.*, **2011**.

Other publications, which are not related to the present thesis:

1. N. Schwierz, P. Nielaba. Colloidal Systems in Three-dimensional Microchannels: Lattice Control via Channel Width and External Force. *Phys. Rev. E*, 82(3), 031401, **2010**.

Appendix **A**

Appendix

A.1. Fit of the Ionic PMFs

To simplify the numerical solution of the Poisson-Boltzmann equation including the ionic PMFs, the entire PMFs are fitted by heuristic fit functions. For anions and cations at the hydrophobic CH3-SAM and at the hydrophilic OH-terminated SAM we use the function

$$\begin{aligned}
\frac{V^{\mathrm{PMF}}(z)}{k_B T} &= \frac{A}{(z+H)^{12}} - \frac{B}{(z+H)^{8}} \\
&+ C(z-D)e^{-E(z-D)^2} + Fe^{-G(z-J)^2} \\
&+ K\left[\left(e^{-L(z-M)}-1\right)^2-1\right] + N \\
&+ Oe^{-P(z-X_1)^2} + Qe^{-R(z-X_2)^2}
\end{aligned} \tag{A.1}$$

for $z \in [0, 1.4]$ and set $V^{\mathrm{PMF}}(z)$ to zero for $z > 1.4$ nm. The fit parameter N is used to provide a continuous function at the point $z = 1.4$ nm. All fit parameters are listed in table A.1 and in table A.2.

For heterogeneous surfaces consisting of hydrophobic and hydrophilic patches we introduce a uniform short range repulsion cut-off $V^{\mathrm{cut}} = 100$ k$_B$T for $V^{\mathrm{PMF}}(z) > 10$ k$_B$T to facilitate the same start point for all PMFs. This cut-off is used for all calculations in chapter 3.

Table A.1.: Fit parameters of the fit function for ionic PMFs used in chapter 2 at the hydrophobic CH$_3$-terminated SAM (upper set) and at the hydrophilic OH-terminated SAM (middle) as well as the additional fit parameters for Na$^+$, F$^-$ and Cl$^-$ at the hydrophilic SAM (bottom). The units of the parameters D, H, J, M, X_1, X_2 are nm, the units of the parameters C and L are nm^{-1}, the units of the parameters E, G, P, R are nm^{-2}, the unit of parameter A is nm^{12} and the unit of parameter B is nm^8.

CH$_3$-SAM,													
	A	H	B	C	D	E	F	G	J	K	L	M	N
Cl$^-$	0.002	0.260	0.131	3.147	0.220	1.740	3.216	5.895	0.429	2.868	3.744	0.654	0.001
F$^-$	0.246	0.441	2.513	2.201	1.108	3.788	2.937	4.985	0.810	2.223	2.742	0.887	-0.009
I$^-$	5.874	0.645	45.773	6.396	0.416	2.590	1.216	41.603	0.713	0.848	3.420	0.980	-0.008
Na$^+$	0.561	0.931	1.373	6.399	0.404	1.258	1.830	10.043	0.679	3.436	2.031	0.838	0.004
OH-SAM													
Cl$^-$	-10.39	0.913	-0.291	15.729	-0.906	1.365	0.440	136.75	0.344	1.469	4.593	0.396	0.004
F$^-$	19.422	1.038	17.910	296.83	-3.509	0.254	0.487	499.73	0.332	32.708	2.201	0.041	-0.038
I$^-$	0.064	0.582	1.642	4.013	-0.069	2.887	0.388	30.339	0.477	0.126	4.653	0.722	0.006
Na$^+$	5.227	1.048	-2.989	7.154	0.122	11.907	-4.780	5.028	-0.110	3.8e-9	4.018	2.633	-0.002
OH-SAM: Additional Fit Parameters													
	O	P	Q	R	X_1	X_2							
Cl$^-$	0.129	300	0	-	0.55	-							
Fl$^-$	0.310	300	0	-	0.52	-							
Na$^+$	0.532	2000	0.176	500	0.325	0.49							

Table A.2.: Same as table A.1 for all cations used in chapter 3

CH$_3$-SAM,													
	A	H	B	C	D	E	F	G	J	K	L	M	N
Li$^+$	3.920	0.590	41.059	5.537	0.411	3.610	1.420	49.280	0.663	0.038	4.020	1.282	-0.042
Na$^+$	-0.089	0.561	1.513	7.001	0.228	2.126	2.361	10.553	0.493	2.823	3.347	0.669	-0.033
K$^+$	0.842	2.479	0.401	4.247	0.766	81.993	0.181	32.042	1.074	0.096	3.238	1.045	-0.027
Cs$^+$	0.839	1.613	1.082	6.611	0.808	60.199	0.420	16.254	1.162	0.443	2.533	0.989	-0.043
CH$_3$-SAM: Additional Fit Parameters for Na$^+$													
	O	P	X_1										
Na$^+$	-0.195	621.55	0.9										
OH-SAM													
Li$^+$	10.149	0.942	18.238	4.282	-0.901	0.411	1.790	85.264	0.303	2.080	1.677	0.707	-0.002
Na$^+$	5.048	1.193	-4.625	10.883	0.124	16.061	-7.485	6.408	-0.053	2.9e-7	3.187	2.757	-0.004
K$^+$	1.637	1.544	-0.937	3.250	0.377	13.635	0.771	93.768	0.326	0.453	4.044	0.427	0.017
Cs$^+$	1.643	2.173	-0.322	4.815	-0.464	1.357	0.622	91.774	0.370	2.223	3.611	0.354	0.020
OH-SAM: Additional Fit Parameters													
	O	P	Q	R	X_1	X_2							
Li$^+$	-1.761	206.1	-1.915	203.1	0.224	0.341							
Na$^+$	0.483	2000	0.255	500	0.325	0.49							
K$^+$	0.105	2000	0	0	0.357	0							

For the uncharged COOH-SAM we use the function

$$\begin{aligned}\frac{V_{\text{Coul}}^{\text{PMF}}(z)}{k_BT} &= \frac{A}{(z+H)^{12}} - \frac{B}{(z+H)^8} \\ &+ C(z-D)e^{-E(z-D)^2} + K\left[\left(e^{-L(z-M)}-1\right)^2-1\right] \\ &+ \sum_i O_i e^{-P_i(z-Q_i)^2} - \Delta \end{aligned} \tag{A.2}$$

for $z \in [0, 1.4]$ and set it to zero otherwise. The fit parameter N is used to provide a continuous function at $z = 1.4$. In the case of fluoride we use two separate fit functions. For $0.336 < z < 1.4$ we use equation Eq. A.2 while for $0 < z < 0.336$ we use

$$\frac{V_{\text{Coul}}^{\text{PMF}}(z)}{k_BT} = \sum_i o_i e^{-p_i(z-q_i)^2} - \Delta_2$$

The number of fit variables O_i, P_i, Q_i depends on the detailed structure of the single PMFs.

For heterogeneous surfaces consisting of uncharged COOH-groups and charged COO$^-$-groups we introduce a uniform short range repulsion cut-off $V^{\text{cut}} = 100\,\text{k}_B\text{T}$ for $V^{\text{PMF}}(z) > 10\,\text{k}_B\text{T}$. All fit parameters are listed in table A.4 and in table A.4. For the charge COO$^-$-terminated SAM we use the function

$$\begin{aligned}\frac{V_{\text{Coul}}^{\text{PMF}}(z)}{k_BT} &= \frac{A}{(z+H)^{12}} - \frac{B}{(z+H)^8} \\ &+ C(z-D)e^{-E(z-D)^2} + K\left[\left(e^{-L(z-M)}-1\right)^2-1\right] \\ &+ \sum_i O_i e^{-P_i(z-Q_i)^2} - \frac{R}{z+S} \end{aligned} \tag{A.3}$$

for $z \in [0, 1.3]$. Before fitting, all PMFs at the charges surface are shifted such that the values at $z = 1.3$ nm correspond to the bare Coulomb-interaction of the ion with the charged surface group. The prefactor of the long-ranged Coulomb potential is calculated from

$$\frac{\alpha}{1.3} = \frac{V_{\text{Coul}}^{\text{PMF}}(z=1.3)}{k_BT} \tag{A.4}$$

and subtracted from the fit function. The resulting ion-surface interaction potential

$$\frac{V^{\text{PMF}}(z)}{k_BT} = \frac{V_{\text{Coul}}^{\text{PMF}}(z)}{k_BT} - \frac{\alpha}{z}. \tag{A.5}$$

is zero for $z > 1.3$ nm.

Table A.3.: Fit parameters of the fit function for ionic PMFs used in chapter 4 at COOH-terminated SAM as well as the additional fit parameters for F^- at the hydrophilic SAM (bottom). The units of the parameters D, H, J, M, Q_i are nm, the units of the parameters C and L are nm^{-1}, the units of the parameters E, P_i are nm^{-2}, the unit of parameter A is nm^{12} and the unit of parameter B is nm^8.

COOH-SAM

	A	H	B	C	D	E	K	L	M
Cl^-	-3.896	-0.231	0.924	8.339	-0.211	12.186	0.266	4.260	0.534
F^-	2.065	-2.162	8.214	9.162	0.465	20.515	0.006	5.908	0.848
I^-	0.030	1.137	0.656	4.540	0.726	28.440	0.131	3.469	0.865
Na^+	1.717	0.080	1.346	1.322	-0.472	1.259	0.175	3.357	0.662
Cs^+	1.716	0.088	1.403	1.533	-0.488	1.391	0.752	4.365	0.318
Li^+	1.435	0.509	5.616	3.308	0.544	7.245	0.211	2.413	0.924

	O_0	P_0	Q_0	O_1	P_1	Q_1	O_2	P_2	Q_2
Cl^-	0.917	302.689	0.380	0.429	11.285	0.541	-0.417	646.257	0.217
F^-	-1246.8	168.898	0.140	-0.517	19.762	0.437	-0.606	76.403	0.650
I^-	0.733	73.415	0.597	0.465	359.383	0.406	0	0	0
Na^+	-0.572	75.240	0.406	0	0	0	0	0	0
Cs^+	-2.360	84.785	0.232	0	0	0	0	0	0
Li^+	-1.059	100.297	0.306	0	0	0	0	0	0

	O_3	P_3	Q_3	O_4	P_4	Q_4	Δ
Cl^-	0	0	0	0	0	0	-0.019
F^-	0.844	944.034	0.335	0	0	0	-0.001
I^-	0	0	0	0	0	0	-0.057
Na^+	0	0	0	0	0	0	0.002
Cs^+	0	0	0	0	0	0	0.007
Li^+	0	0	0	0	0	0	-0.096

COOH-SAM - additional fit function for F^- for $0 < z < 0.336$

	o_0	p_0	q_0	o_1	p_1	q_1	o_2	p_2	q_2
F^-	-1.960	159.456	0.139	-0.517	793.333	0.308	-20.953	29.758	0.591

	o_3	p_3	q_3	Δ_2
F^-	16.134	-8.966	0.130	20.315

Table A.4.: Fit parameters of the fit function for ionic PMFs used in chapter 4 at charged COO^--terminated SAM. The units of the parameters D, H, J, M, Q_i are nm, the units of the parameters C and L are nm^{-1}, the units of the parameters E, P_i are nm^{-2}, the unit of parameter A is nm^{12} and the unit of parameter B is nm^8.

	COO^--SAM								
	A	H	B	C	D	E	K	L	M
Cl^-	28514300	751474	2.321	30.992	-0.554	1.102	-31.210	-0.016	-0.653
F^-	1.743	-3.566	0.514	-1.609	1.352	1.634	32.467	0.148	0.878
I^-	0.018	0.340	0.109	30.938	-0.598	1.044	-0.891	0	-0.827
Na^+	-10.028	23.214	1.184	0	0	0	0	0.634	9.647
Cs^+	5746.940	1924.780	1.614	0	0	0	0	1.954	9.647
	O_0	P_0	Q_0	O_1	P_1	Q_1	O_2	P_2	Q_2
Cl^-	154.775	0.355	0.564	1.414	149.034	0.704	-246.338	0.290	0.809
F^-	-1.454	389.277	0.523	0.819	305.343	0.675	-0.168	23.046	1.068
I^-	-0.463	183.776	0.870	29.396	62.169	0.371	-2.516	6.744	0.819
Na^+	-22.494	152.505	0.019	4.833	486.425	0.209	-9.097	26.240	0.246
Cs^+	-15.197	217.488	0.090	10.168	235.345	0.280	-11.214	98.174	0.306
	O_3	P_3	Q_3	O_4	P_4	Q_4	R	S	α
Cl^-	0	0	0	0	0	0	-257.695	1.568	0.672
F^-	0	0	0	0	0	0	20636	-630.188	0.691
I^-	0	0	0	0	0	0	154.457	138.099	0.777
Na^+	7.029	107.631	0.391	-0.952	284.333	0.573	-0.068	0.144	-0.514
Cs^+	-0.705	28.162	0.644	0	0	0	0.566	0.045	-0.790

A.2. Ionic Force Fields and Surface Modeling

All Lennard-Jones parameters of ions and surface atoms are listed in table A.5. Note that the ion-water Lennard-Jones diameters σ_{iW} are given, so we determine the ion-ion diameters according to the Lorentz-Berthelot and geometric rules, denoted by σ_{ii}^{LB} and σ_{ii}^{geo}, respectively. In this work, we have used the geometric rule for all other LJ interactions.

Table A.5.: Lennard-Jones (LJ) parameters used in the simulations. σ_{iW} and ϵ_{iW} are the LJ parameters for the interaction between the water oxygen atom and the ions or the terminal groups of the nonpolar and polar SAMs. σ_{ii}^{LB} is the Lennard-Jones diameter according to the Lorentz-Berthelot combination rule, $\sigma_{ij}^{LB} = (\sigma_{ii}^{LB} + \sigma_{jj}^{LB})/2$, σ_{ii}^{geo} and ϵ_{ii} are the Lennard-Jones parameters according to the geometric combination rules, $\sigma_{ij}^{geo} = \sqrt{\sigma_{ii}^{geo}\sigma_{jj}^{geo}}$ and $\varepsilon_{ij} = \sqrt{\varepsilon_{ii}\varepsilon_{jj}}$. The negative charge of the CH_3- and OH-terminal groups is compensated by positive partial charges on the adjacent CH_2 groups of the SAM.

atom/molecule	σ_{iW} (Å)	ϵ_{iW} (kJ/mol)	σ_{ii}^{LB} (Å)	σ_{ii}^{geo} (Å)	ϵ_{ii} (kJ/mol)	q ($\lvert e\rvert$)
Li^+	2.27	1.00	1.37	1.63	1.54	1.0
Na^+	2.65	1.00	2.13	2.22	1.54	1.0
K^+	2.97	1.00	2.77	2.79	1.54	1.0
Cs^+	3.25	1.00	3.33	3.34	1.54	1.0
F^-	3.30	0.55	3.43	3.44	0.46	-1.0
Cl^-	3.78	0.52	4.40	4.52	0.42	-1.0
I^-	4.25	0.32	5.33	5.71	0.16	-1.0
CH_3	3.44	0.75	-	3.75	0.87	-0.014
O (of OH)	3.06	0.74	-	2.95	0.85	-0.734
H (of OH)	-	-	-	-	-	0.408
C (of COOH)	3.36	0.42	-	3.58	0.28	0.33
O (of COOH)	2.95	0.91	-	2.76	1.28	-0.45
O (of COOH)	3.06	0.74	-	2.95	0.85	-0.288
H (of COOH)	-	-	-	-	-	0.408
C (of COO^-)	3.36	0.42	-	3.58	0.28	0.27
O (of COO^-)	2.95	0.91	-	2.76	1.28	-0.635
O (of SPC/E)	3.169	0.650	3.169	3.169	0.650	-0.848
H (of SPC/E)	-	-	-	-	-	0.424

A.3. Local Dielectric Constant and Critical Coagulation Concentration

The water density profile $\rho(z)$ at the hydrophobic CH_3-terminated SAM and at the hydrophilic OH-terminated SAM is approximated by the fit function

$$\begin{aligned}\frac{\rho(z)}{\rho_0} &= a_1 e^{-b_1(z-c_1)^2} + a_2 e^{-b_2(z-c_2)^2} + a_3 e^{-b_3(z-c_3)^2} \\ &+ a_4 \tanh(b_4(z-c_4)) + a_5 \tanh(b_5(z-c_5)) \\ &+ d_1. \end{aligned} \tag{A.6}$$

At the CH_3-SAM/water interface the fit function is set to zero for $z \in [0, 0.179]$. The fit parameters of the density profile $\rho(z)$ at the CH_3-terminated and the OH-terminated SAM as well as the position of the Gibbs dividing surface are listed in table A.6.

The critical coagulation concentration c_{coag} (Eq. 2.17) has to be solved numerically since Φ_{DH} has an implicit dependence on the salt concentration. To facilitate the numerical solution, we fit the dependence of the Debye Hückel surface potential Φ_{DH} on the salt concentration c_0 and bare surface charge σ_{surf} to a polynomial. Since in the salt concentration range of interest the dependence of Φ_{DH} on σ_{surf} is linear to a good approximation, we make the fitting ansatz

$$\Phi_{\text{DH}} = \alpha(c_0) + \beta(c_0)\sigma_{\text{surf}}. \tag{A.7}$$

The parameters $\alpha(c_0)$ and $\beta(c_0)$ are fitted using the following expressions

$$\alpha(c_0) = a_1 c_0 + a_2 c_0^2 + a_3 c_0^3 + a_4 c_0^4 + a_5, \tag{A.8}$$

$$\beta(c_0) = b_1 c_0^{-1} + b_2 c_0^{-2} + b_3. \tag{A.9}$$

All fit parameters are listed in table A.7. Using Eq. A.7 and Eq. A.9, the critical coagulation concentration c_{coag} is obtained by solving Eq. 2.17 numerically.

Table A.6.: Fit parameters of the fit function for the water density profile from molecular dynamic simulation at the hydrophobic CH_3-terminated SAM and at the hydrophilic OH-terminated SAM and position of the Gibbs dividing surface $\mathrm{z_{GDS}}$ in nm, for which the surface excess of water itself vanishes. The units of the parameters b_1, b_2, b_3, b_4, b_5 are nm^{-2} and the units of the parameters c_1, c_2, c_3, c_4, c_5 are nm.

	$\mathrm{a_1}$	$\mathrm{a_2}$	$\mathrm{a_3}$	$\mathrm{a_4}$	$\mathrm{a_5}$	$\mathrm{b_1}$	$\mathrm{b_2}$	$\mathrm{b_3}$
CH_3-SAM	0.908	-0.09	0.252	-3.102	3.998	104.373	162.505	37.409
OH-SAM	0.109	-0.084	0	2.136	-1.636	200.012	300.074	0
	$\mathrm{b_4}$	$\mathrm{b_5}$	$\mathrm{c_1}$	$\mathrm{c_2}$	$\mathrm{c_3}$	$\mathrm{c_4}$	$\mathrm{c_5}$	$\mathrm{d_1}$
CH_3-SAM	3.437	2.575	0.45	0.862	0.771	0.036	0.047	0.104
OH-SAM	13.851	12.945	0.225	0.347	0	0.143	0.161	0.50
	$\mathrm{z_{GDS}}$							
CH_3-SAM	0.319							
OH-SAM	0.086							

Table A.7.: Fit parameters for the concentration dependence of the functions $\alpha(c_0)$ and $\beta(c_0)$ in eq A.7. Parameter a_1 is in units mV $(\mathrm{mol/L})^{-1}$, a_2 in mV $(\mathrm{mol/L})^{-2}$, a_3 in mV $(\mathrm{mol/L})^{-3}$, a_4 in mV $(\mathrm{mol/L})^{-4}$, a_5 in mV, b_1 in $\mathrm{molmVm^2/LC}$, b_2 in $\mathrm{mol^2mVm^2/L^2C}$ and b_3 in $\mathrm{mVm^2/C}$.

				CH_3-SAM				
	a_1	a_2	a_3	a_4	a_5	b_1	b_2	b_3
NaFl	5.909	4.285	6.397	0.794	0.078	7.193	-0.023	0.254
NaCl	-6.922	5.745	-2.465	1.978	-0.263	9.473	-0.044	0.226
NaI	-35.457	30.14	-21.566	9.234	-1.195	12.639	-0.073	0.174
				OH-SAM				
	a_1	a_2	a_3	a_4	a_5	b_1	b_2	b_3
NaF	-40.482	-8.739	-57.073	6.218	-0.849	10.002	-0.050	0.248
NaCl	-16.240	-4.920	-19.528	3.124	-0.366	07.144	-0.024	0.289
NaI	-6.706	-7.903	-7.866	-0.905	-0.178	6.065	-0.014	0.306

A.4. Equilibration at Hydrophobic and Hydrophilic Surfaces

Fig. A.1A, B show the PMFs for Na^+ at the nonpolar and polar surface after different simulation times. The differences between the PMFs at the nonpolar surface after 0.5 ns, 0.7 ns and 1 ns are smaller than 0.1 k_BT and thus negligible, while at the polar surface the difference between the PMF after 0.5 ns and 1 ns are larger than 2 k_BT for small distances from the interface, indicating that the equilibration at the hydrophilic surface is slow compared to the hydrophobic surface. After 3 ns the PMF of Na^+ at the hydrophilic surface changes by less than 0.2 k_BT.

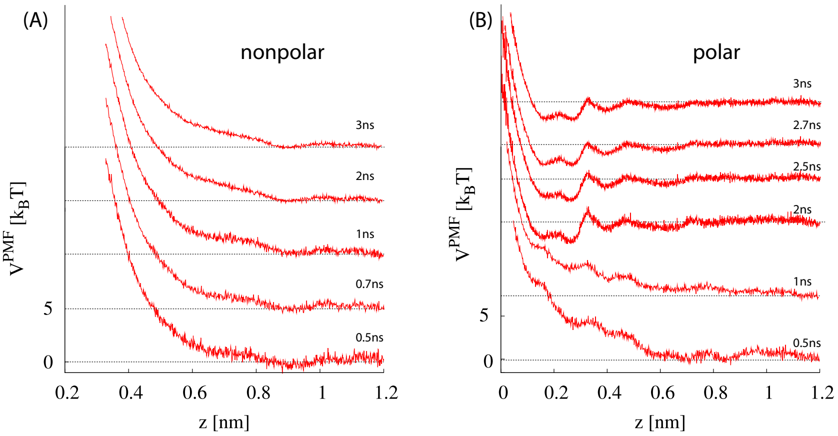

Figure A.1.: PMFs of Na $^+$ at the hydrophobic (A) and the hydrophilic surface (B) in dependence of the time of Umbrella sampling. PMFs for different times are shifted vertically with horizontal dotted lines indicating their base lines.

A.5. Influence of Ionic Force Fields and Water Models

The choice of the force field of the ions is crucial for the results of molecular dynamics simulations. Therefore, we used force field parameters for anions and cations that were previously optimized for the SPC/E water model [108] to reproduce thermodynamic solvation properties [68]. From the three different cation parameter sets given in [68] we have used parameter set 2 for all cations in our calculations. This choice was mainly motivated by recent work showing that relatively high Lennard-Jones energy parameter for cations yield accurate ion pairing properties as judged by comparison with experimental osmotic coefficient data [109]. Fig. A.2A-C show a comparison of the PMFs obtained by using the three different parameter sets of [68] at the hydrophobic surface. The difference between the resulting PMFs from the 3 parameter sets is smaller that the difference between the ions and one expects the same qualitative results. Fig. A.2D,E show a comparison of PMFs obtained for the two different water models SPC and SPC/E. The difference between the resulting PMFs is small. Still, the choice of the SPC/E water model is recommended since the ionic force fields where optimized for SPC/E water. Fig. A.2F shows a comparison of the PMFs obtained by using parameter sets 2 and 3 of

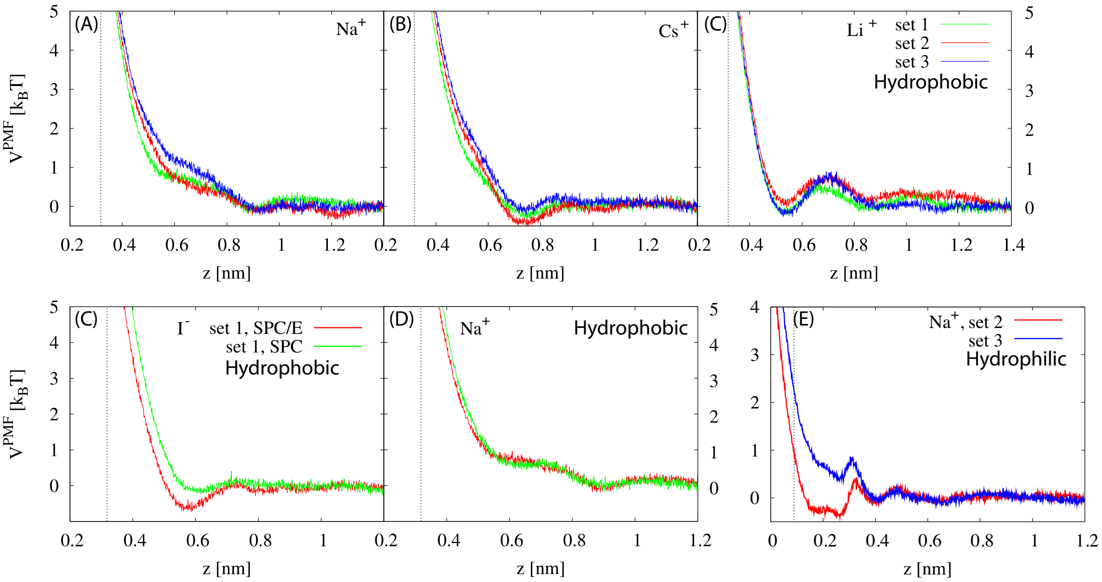

Figure A.2.: Comparison of the PMF of Na^+ (A), Cs^+ (B) and Li^+ (C) at the hydrophobic SAM/water interface for the three different parameter sets. Comparison of the PMF of iodide (D) and sodium (E) at the hydrophobic SAM/water interface for the two different water models SPC and SPC/E. For the cation parameter set 1 is used. (E) Comparison of the PMF of sodium at the hydrophilic SAM/water interface for two different parameter sets. At the hydrophobic surface umbrella sampling is done for 1 ns, discarding the first 200 ps for equilibration. At the hydrophilic surface umbrella sampling is done for 3 ns, discarding the first 1 ns for equilibration.

[68] at the hydrophilic surface. Here, the difference between the parameter sets is about 1 k_BT at small separations. Using different force fields or different water models has a quantitative influence on the results. The development of ionic force fields based on thermodynamic solvation properties and experimental data like osmotic coefficient data is therefore fundamental for quantitative predictions.

Appendix B

Appendix 2

B.1. Force-extension Curves at the Hydrophobic Surface

The desorption force of 9 different homopolypeptides consisting of 12 amino acids and the polypeptide $(GVGVP)_3$ are determined using dynamic simulations with constant pulling velocity (v=0.1 m/s) and static pulling simulations. The results of these simulations, i.e. the force F in dependence of the separation from the surface z, are shown in Fig. B.1 for all peptides at the hydrophobic CH_3-terminated SAM. The separation is measured from the surface defined by the mean position of the terminal C and O surface atoms for the hydrophobic and hydrophilic surfaces, respectively. The lines result from the dynamic pulling for different initial configurations. Open symbols result from 20 ns static simulation where the cantilever is held at a fixed separation from the surface discarding the first 5 ns for equilibration. For all peptides the results from the dynamic pulling are in good agreement with the results from the pulling in the limit of vanishing pulling speed. Therefore, the dissipative contribution on the hydrophobic surface is small enough not to cause equilibration problems. For the positively charged lysine two different desorption paths are obtained. In the first path the peptide desorbs at small separations ($z_{\mathrm{AFM}} = 0.7$ nm) and the desorption force drops to zero. In the second path the peptide re-adsorbs on the surface. Therefore, a non-vanishing force is observed until the peptide desorbs at $z_{\mathrm{AFM}} = 1.6$ nm. Still, the different paths result in similar desorption forces but in different rupture lengths (see table B.1). Most peptides show a similar desorption process in which peptide desorbs gradually amino acid by amino acid from the hydrophobic surface. Exceptions are the peptides E, N and K. During the pulling simulations these peptides desorb from the surface and adsorb again. Therefore, the energy difference between the surface adsorbed configuration and the stretched configuration is not well defined and those peptides are excluded from the energy decomposition.

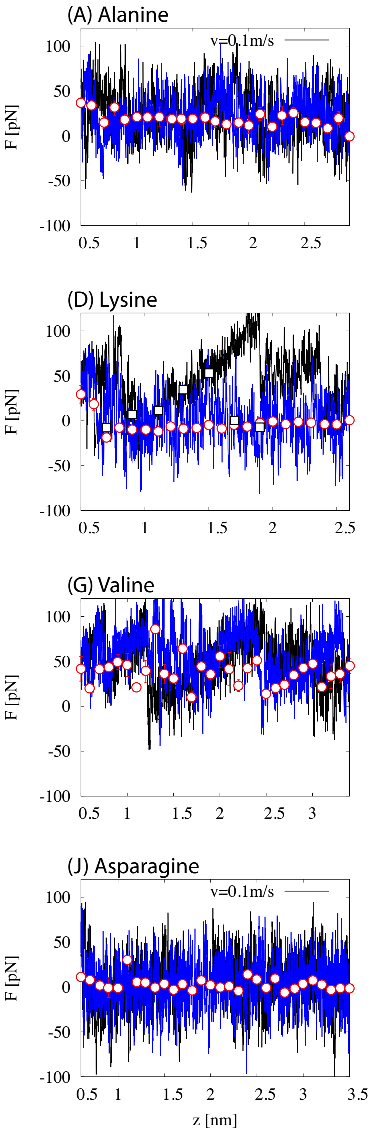

Figure B.1.: Dynamic desorption force (lines) and static force (open points) in dependence of the surface separation on the hydrophobic CH_3-terminated SAM for 9 different homopolypeptides consisting of 12 amino acids and the polypeptide $(GVGVP)_3$.

B.2. Force-extension Curves at the Hydrophilic Surface

Fig. B.2 shows the desorption force in dependence of the surface separation at the hydrophilic OH-terminated SAM for the same peptides as in Fig. B.1. Different starting points of the force-extension curves result from the different separations of the first amino acid from the surface in the different initial configurations. The desorption force of glutamic acid depends on the initial configuration. We observe two desorption paths for which the forces are different. The reason for the different paths is the combination of

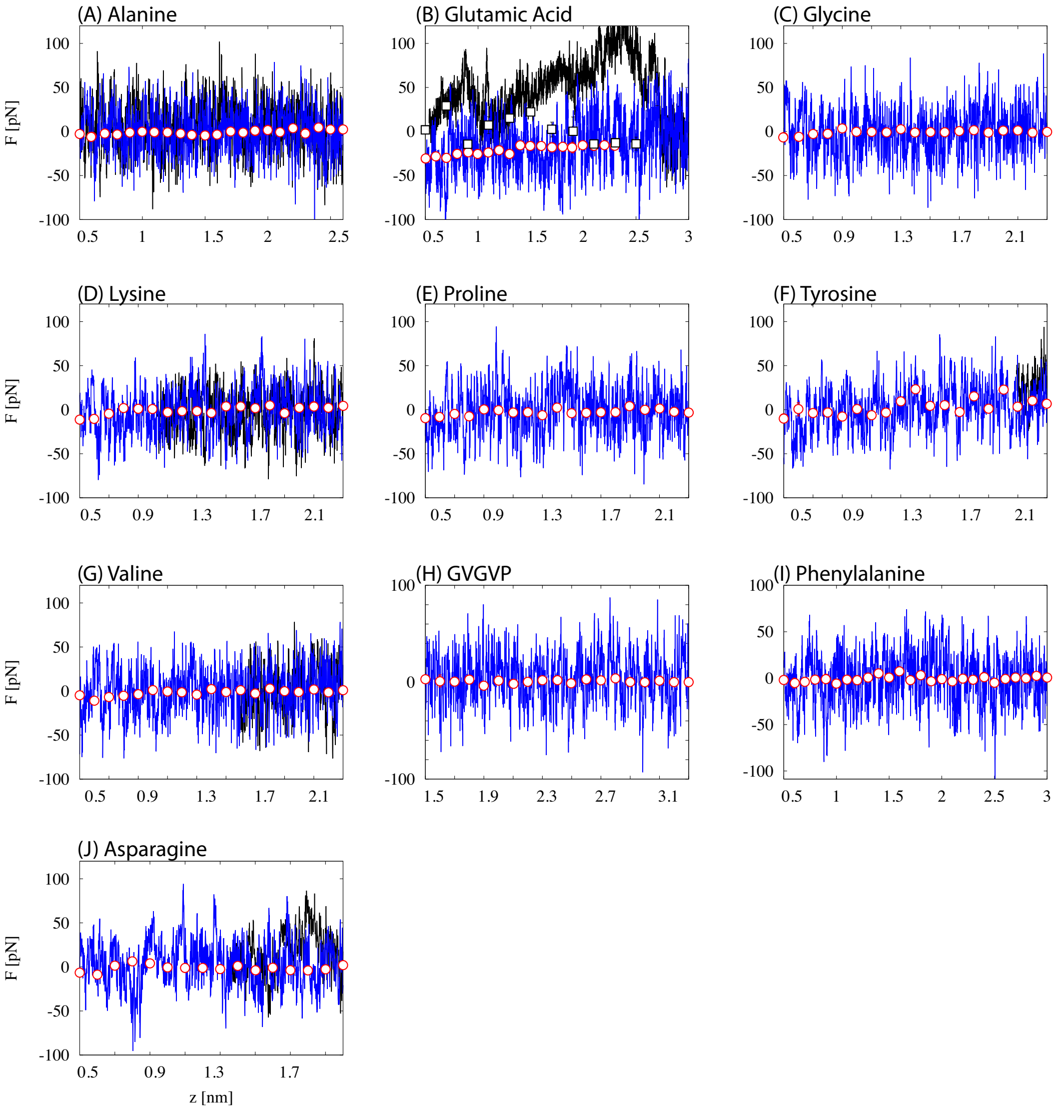

Figure B.2.: Dynamic desorption force (lines) and static force (open points) in dependence of the surface separation on the hydrophilic OH-terminated SAM for 9 different homopolypeptides consisting of 12 amino acids and the polypeptide $(GVGVP)_3$.

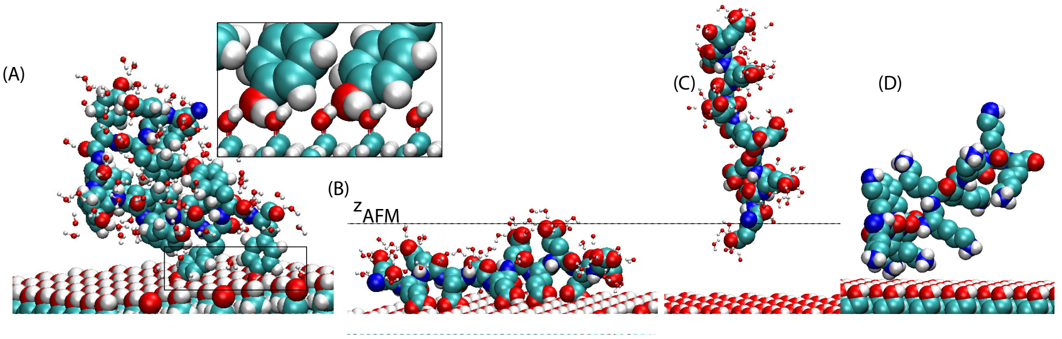

Figure B.3.: Simulation snapshots of adsorbing peptides at the hydrophilic surface. (A) Snapshot of tyrosine after equilibration. The inset shows the interaction between the OH-groups of two side-chain with the surface. (B) Adsorbing configuration and (C) non-adsorbing configuration of glutamic acid for $z_{\text{AFM}} = 0.7$ nm. The broken line indicates the position of the AFM tip. (D) Snapshot of lysine at the hydrophilic surface for $z_{\text{AFM}} = 0.7$ nm. Hydrogen bonding between the side-chains and the surface partially cancel the image charge repulsion.

repulsive image charge forces acting on charged peptides and the formation of hydrogen bonds between the polar groups of the side-chain and the OH-surface groups. For the first desorption path, we find adsorption of the peptide at the hydrophilic surface. In the adsorbing configuration (Fig. B.3B) 2 hydrogen bonds form between each protonated side-chain and the surface. For the second desorption path the peptide is repelled from the surface. For the non-adsorbing configuration (Fig. B.3C) the image charge repulsion dominates and no hydrogen bonds form between peptide and surface. The magnitude of the image charge force F_{ic} can be estimated from

$$F_{\text{ic}} = \frac{1}{2} \sum_{ij} \frac{q_i q_j}{4\pi\epsilon\epsilon_0 (2(z_i - z_j))^2} \tag{B.1}$$

where $q_i = -1$ is the charge of the deprotonated side-chains, ϵ is the relative dielectric constant and $(z_i - z_j)$ is the distance of the charges perpendicular to the surface. Using the configurations obtained from the static simulations yields an image charge force of 12 pN for $z_{\text{AFM}} = 0.7$ nm.

For lysine at the hydrophilic surface the repulsion is weaker than estimated from image charge repulsion alone. The reason is that lysine forms hydrogen bonds with the OH-surface groups (Fig. B.3D) which partially cancel the image charge repulsion.

We find a weak peptide-surface interaction for tyrosine leading to an adsorption force of about 4 pN. For asparagine direct peptide-surface interactions are observed as well. Still, the desorption force is almost zero. The reason for the peptide-surface interaction observed for these amino acids is that they contain polar groups in their side-chains. For all nonpolar side-chains direct peptide-surface interactions are inhibited by the strongly bound first hydration layer of water at the hydrophilic surface and the adsorption force vanishes.

B.3. Spontaneous Desorption

During the initial relaxation, all peptides adsorbs readily onto the hydrophobic CH_3-terminated SAM. Spontaneous desorption during equilibration is never observed at these hydrophobic surfaces except for fully charged lysine and glutamic acid peptides where the image charge repulsion is larger than the attractive adsorption force. In order to mimic charge regulation [179], the glutamic acid and lysine are not fully charged but the degree of dissociation is smaller than 1. According to the pK_a of glutamic acid ($pK_a = 4.25$) and lysine ($pK_a = 10.53$) the dissociation degree of these peptides at pH 7 is reduced to 0.5 [179, 193]. In contrast to the adsorption on the hydrophobic surface, most peptides desorb spontaneously during the equilibration at the hydrophilic surface. Adsorption on the hydrophilic OH-terminated SAM during the 10 ns equilibration is only observed for amino acids containing polar groups (E, Y, N). The simulation results of the 10 peptides are summarized in table B.1.

Table B.1.: Details of the 10 peptides used in simulations: Glutamic acid (E), asparagine (N), lysine (K), glycine (G), alanine (A), proline (P), valine (V), tyrosine (Y), phenylalanine (F) and the polypeptide GVGVP. The table shows the side-chain, the residue volume v_r from [193], the scaled hydrophobicity h_S from [184], spontaneous desorption of complete peptide during 10 ns equilibration from the hydrophilic OH-terminated SAM p_sd ($p_\mathrm{sd} = 1$ spontaneous desorption observed, $p_\mathrm{sd} = 0$ adsorption during equilibration), the average desorption forces on the hydrophobic $\mathrm{F}_\mathrm{Des}^\mathrm{CH3}$ and the hydrophilic surface $\mathrm{F}_\mathrm{Des}^\mathrm{OH}$, the free energy of desorption A for the complete peptide and the rupture length L.

Residue	side-chain	v_r^* [Å^{-3}]	h_S	p_sd	$\mathrm{F}_\mathrm{Des}^\mathrm{CH3}$ [pN]	$\mathrm{F}_\mathrm{Des}^\mathrm{OH}$ [pN]	A [kJ/mol]	L [nm]
E	$-(CH_2)_2-COO$	109	0.08	0	19.48 ± 4.00	-21.36 ± 1.28	-	0.9
						$+14.02 \pm 5.85$		
N	$-CH_2-CO-NH_2$	94	0.236	0	1.85 ± 1.06	$+0.30 \pm 0.80$	-	2.7
K	$-(CH_2)_4-NH_3^+$	135	0.283	1	21.82 ± 5.19	-0.003 ± 1.05	-	0.2
					20.84 ± 8.14			1.1
G	-H	48	0.501	1	16.04 ± 0.59	-0.55 ± 0.41	16.42 ± 0.60	1.7
A	$-CH_3$	67	0.616	1	17.31 ± 1.61	-1.17 ± 0.52	23.98 ± 2.23	2.3
GVGVP	-	-	0.673	1	29.95 ± 2.54	$+1.1 \pm 0.37$	55.918 ± 4.75	3.1
P	$-(CH_2)_3$	90	0.711	1	50.33 ± 3.43	-2.14 ± 0.82	78.80 ± 5.36	2.6
V	$- CH-(CH_3)_2$	105	0.85	1	39.81 ± 3.76	-1.76 ± 0.80	83.91 ± 7.92	3.5
Y	$-CH_2-C_6H_5-OH$	141	0.88	0	24.65 ± 2.65	$+3.83 \pm 2.13$	48.98 ± 5.27	3.3
F	$-CH_2-C_6H_6$	135	1.00	1	45.09 ± 2.94	-1.15 ± 0.68	97.76 ± 6.37	3.6

B.4. Force in Dependence of OH-concentration

Fig. B.4 shows simulation snapshots of the heterogeneous methyl/hydroxyl SAMs and the force-extension curves using dynamic simulations with constant pulling velocity ($v = 0.1$ m/s) and static pulling simulations for alanine. The results from the dynamic pulling and the static simulations are in good agreement. For high OH-surface concentrations (33, 66%) we observe spontaneous desorption during the NPT equilibration indicating adsorption resistance.

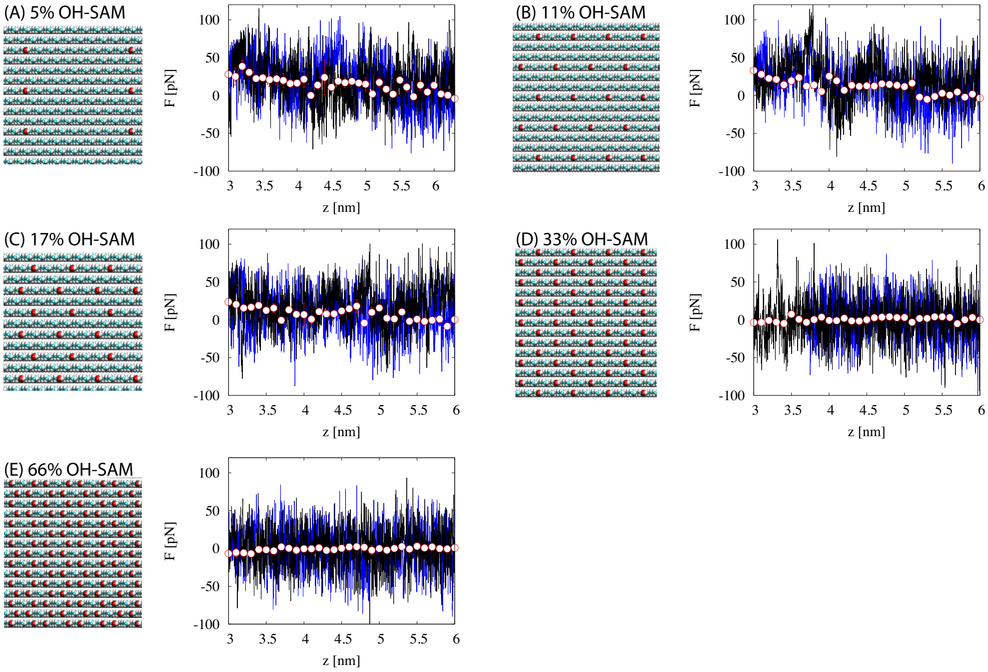

Figure B.4.: Snapshot of the surface composition (left) and force-extension curves (right) of alanine for pulling velocity $v = 0.1$ m/s and different initial configurations (solid lines) and static simulation results (open points) for different OH surface concentrations (A) 5% OH, (B) 11% OH, (C) 17% OH, (D) 33% OH and (E) 66% OH.

B.5. Hydrogen Bonds of Adsorbed and Desorbed Configuration

Fig. B.5 shows the difference in the number of hydrogen bonds per amino acid $\Delta n_{\mathrm{hb}} = n_{\mathrm{hb}}^{\mathrm{A}} - n_{\mathrm{hb}}^{\mathrm{B}}$ for the forced adsorbed configuration $n_{\mathrm{hb}}^{\mathrm{A}}$ and the bulk configuration $n_{\mathrm{hb}}^{\mathrm{B}}$ in dependence of the average position of the peptide alanine from the surface using different constant external forces for the OH-terminated SAM. The difference in the number of hydrogen bonds in the configurations is decomposed into the contributions of water-water, peptide-surface, surface-water and peptide-water hydrogen bonds. At the

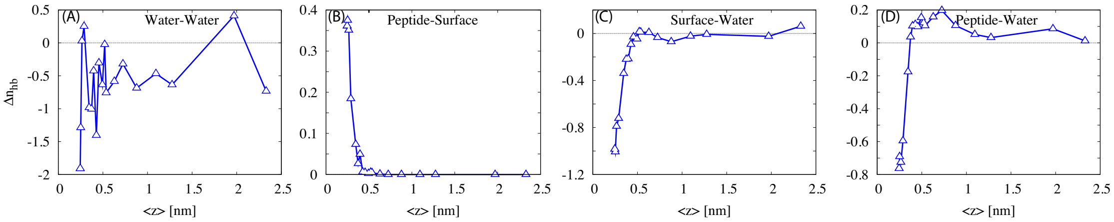

Figure B.5.: Difference in the number of hydrogen bonds per amino acid $\Delta n_{\mathrm{hb}} = n^{\mathrm{A}}_{\mathrm{hb}} - n^{\mathrm{B}}_{\mathrm{hb}}$ for the surface adsorbed configuration $n^{\mathrm{A}}_{\mathrm{hb}}$ and the bulk configuration $n^{\mathrm{B}}_{\mathrm{hb}}$ in dependence of the average position $< z >$ obtained from different constant external forces acting on alanine on the OH-terminated surface. (A-D) show the decomposition into the contributions of water-water, peptide-surface, surface-water and peptide-water hydrogen bonds.

hydrophilic surface with 100% OH-surface concentration the total number of hydrogen bonds in the bulk configuration is larger than in the surface adsorbed configuration. Adsorption resistant is therefore driven by the gain of entropy and hydrogen bonds.

The number of hydrogen bonds can be further analyzed by dividing the simulation box into three regions. We calculate the total number of hydrogen bonds in the region including the hydrogen bonds with the next neighbors at the edges of the regions. The number corresponds to the actual total number of hydrogen bonds between the water molecules and not to the number of hydrogen bonds that each water molecule forms with its neighbors (which is a factor of two higher).

Region 1: 1 nm thick layer above the surface containing N_1 water molecules and a total number of $\mathrm{N}^{\mathrm{HB}}_{\mathrm{WW1}}$ hydrogen bonds. At the hydrophilic surface $\mathrm{N}^{\mathrm{HB}}_1$ is the sum of water-water hydrogen bonds $\mathrm{N}^{\mathrm{HB}}_{\mathrm{WW1}}$ and water-surface hydrogen bonds $\mathrm{N}^{\mathrm{HB}}_{\mathrm{SW1}}$

$$\mathrm{N}^{\mathrm{HB}}_1 = N^{\mathrm{HB}}_{\mathrm{WW1}} + N^{\mathrm{HB}}_{\mathrm{SW1}} \tag{B.2}$$

Region 2: A water slap in between the edges of the surfaces (due to the periodic boundary conditions in the simulation) which has a distance of 1 nm from each surface and contains N_2 water molecules and a total number of $\mathrm{N}^{\mathrm{HB}}_2$ hydrogen bonds.

Region 3: 1 nm thick layer at the top of the simulation box. Note that due to the symmetry of the system the number of water molecules and the total number of hydrogen bonds in this region is identical to region 1. Table B.2 shows the number of water molecules and the number of hydrogen bonds in the different regions for the two configurations where the peptide is in bulk or at the surface. Simulation snapshots of the water molecules and the hydrogen bond in a cutout of region 1 and 2 are shown in Fig. B.6 for the two configuration for the hydrophilic 100% OH-terminated SAM.

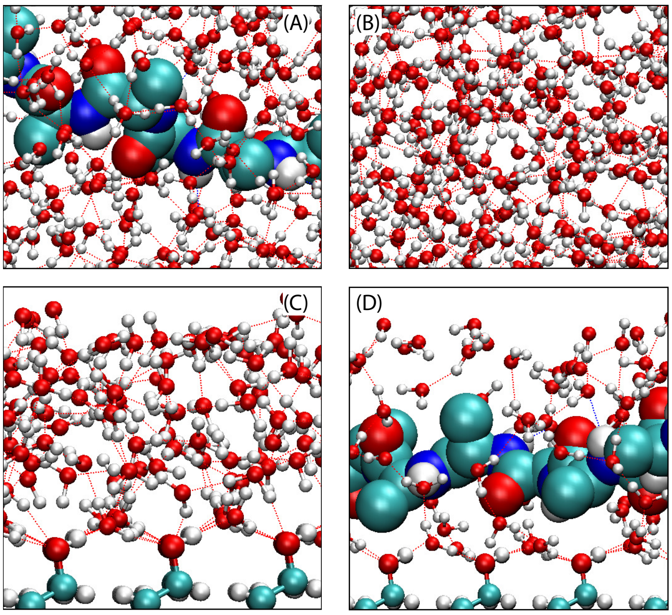

Figure B.6.: Simulation snapshots of the water molecules and the hydrogen bonds in a cutout of region 1 and 2 for the two configuration for the hydrophilic 100% OH-terminated SAM. (A) Region 2 with peptide. (B) Region 2 without peptide. (C) Region 1 without peptide. (D) Region 1 with peptide.

Table B.2.: Number of water molecules N_1 and N_2 and the number of hydrogen bonds N_1^{HB} and N_2^{HB} in the different regions for the two configurations where the peptide is in bulk or at the hydrophobic or at the hydrophilic surface. N is the total number of water molecules in the simulation box and N_{WW}^{HB} is the total number of water-water hydrogen bonds. The number of hydrogen bonds corresponds to the actual total number of hydrogen bonds between the water molecules and not to the number of hydrogen bonds that each water molecule forms with its neighbors (which is a factor of two higher). Note that this definition is the same as in Gromacs 3.3.1 but not in Gromacs 4.5.3 where the number of water-water molecules are by definition 1 in bulk water. Hydrogen bonds are calculated according to the distance angle-criterion for distances smaller than 0.35 nm and angle smaller than 30°.

	100% OH-SAM		CH_3-SAM	
	bulk	surface	bulk	surface
N	3755	3755	3776	3776
N_{WW}^{HB}	6343.1	6335.48	6425.26	6439.32
N_1	539	508	426	380
N_1^{HB}	901.65	852.27	692.23	517.66
N_1^{HB}/N_1	1.67	1.68	1.625	1.36
	Water slap			
	bulk	surface		
N_2	2924	3016		
N_2^{HB}	5040.8	5404		
N_2^{HB}/N_2	1.72	1.79		

Bibliography

[1] N. Schwierz, D. Horinek and R. R. Netz. Reversed Anionic Hofmeister Series: The Interplay of Surface Charge and Surface Polarity. *Langmuir*, 26(10):7370–7379, **2010**.

[2] J. Dzubiella, M. Fyta, D. Horinek, I. Kalcher, R. R. Netz and N. Schwierz. *Specific Ion Effects*, in Ion-Specificity: From Solvation Thermodynamics to Molecular Simulations and Back, (ed. by W. Kunz, World Scientific Publishing, Singapore), 1st edition, **2010**.

[3] E. R. A. Lima, M. Boström, N. Schwierz and F. W. Tavares. Attractive Double-Layer Forces between Neutral Hydrophobic and Neutral Hydrophilic Surfaces. *Phys. Rev. E*, 84(6):061903, **2011**.

[4] N. Schwierz, D. Horinek and R. R. Netz. Comparison of Anionic and Cationic Hofmeister Effects. *To be published*, **2011**.

[5] N. Schwierz, D. Horinek and R. R. Netz. Specific Ion Binding to Charged Surface Groups. *To be published*, **2011**.

[6] N. Schwierz and R. R. Netz. Effective Interaction between two Ion-adsorbing Plates: Hofmeister Series and Salting-in/Salting-out Phase Diagrams from a Global Mean-field Analysis. *Submitted to Langmuir*, **2011**.

[7] N. Schwierz, D. Horinek, S. Liese, T. Pirzer, B. N. Balzer, T. Hugel and R. R. Netz. The Role of Surface Hydrophobicity in Bioadhesion. *To be published*, **2011**.

[8] S. Kienle, S. Liese, N. Schwierz, R. R. Netz and T. Hugel. The Effect of Temperature on Single Polypeptide Adsorption. *Accepted in Chem. Phys. Chem.*, **2011**.

[9] W. Kunz. *Specific Ion Effects* (World Scientific Publishing, Singapore), 1st edition, **2010**.

[10] F. Hofmeister. Zur Lehre von der Wirkung der Salze (About the science of the effect of salt). *Arch. Exp. Pathol. Phar.*, 24(24):247–260, **1888**.

[11] W. Kunz, J. Henle and B. W. Ninham. 'Zur Lehre von der Wirkung der Salze' (about the science of the effect of salts): Franz Hofmeister's historical papers. *Curr. Opin. Colloid Interface Sci.*, 9(1-2):19–37, **2004**.

[12] M. Cacace, E. Landau and J. Ramsden. The Hofmeister series: salt and solvent effects on interfacial phenomena. *Q. Rev. Biophys.*, 30(3):241–277, **1997**.

[13] K. Collins and M. Washabaugh. The Hofmeister effect and the behavior of water at interfaces. *Q. Rev. Biophys.*, 18(4):323–422, **1985**.

[14] J. Lyklema. Lyotropic sequences in colloid stability revisited. *Adv. Colloid Interface Sci.*, 100-102:1–12, **2003**.

[15] W. Kunz, P. Lo Nostro and B. W. Ninham. The present state of affairs with Hofmeister effects. *Curr. Opin. Colloid Interface Sci.*, 9(1-2):1–18, **2004**.

[16] R. Baldwin. How Hofmeister ion interactions affect protein stability. *Biophys. J.*, 71(4):2056–2063, **1996**.

[17] J. Broering and A. Bommarius. Evaluation of Hofmeister effects on the kinetic stability of proteins. *J. Phys. Chem. B*, 109(43):20612–20619, **2005**.

[18] W. Melander and C. Horvath. Salt Effects on Hydrophobic Interactions in Precipitation and Chromatography of Proteins: An Interpretation of the Lyotropic Series. *Arch. Biochem. Biophys.*, 183(1):200–215, **1977**.

[19] P. H. von Hippel and K.-Y. Wong. Neutral Salts: The Generality of Their Effects on the Stability of Macromolecular Conformations. *Science*, 145(3632):577–580, **1964**.

[20] K. D. Collins. Ions from the Hofmeister series and osmolytes: effects on proteins in solution and in the crystallization process. *Methods*, 34:300–311, **2004**.

[21] M. Ries-Kautt and A. Ducruix. Relative effectiveness of various ions on the solubility and crystal growth of lysozyme. *J. Biol. Chem.*, 264(2):745–748, **1989**.

[22] R. Curtis and L. Lue. A molecular approach to bioseparations: Protein-protein and protein-salt interactions. *Chem. Eng. Sci.*, 61(3):907–923, **2006**.

[23] J. Ha, M. Capp, M. Hohenwalter et al. Thermodynamic stoichiometries of participation of water, cations and anions in specific and nonspecific-binding of LAC repressor to DNA - possible thermodynamic origins of the glutamate effect on protein-DNA interactions. *J. Mol. Biol.*, 228(1):252–264, **1992**.

[24] C. Anderson and M. Record. Salt nucleic-acid interactions. *Annu. Rev. Phys. Chem.*, 46:657–700, **1995**.

[25] C. Suelter. Enzymes activated by monovalent cations. *Science*, 168(3933):789, **1970**.

[26] J. Heyda, J. Pokorna, L. Vrbka et al. Ion specific effects of sodium and potassium on the catalytic activity of HIV-1 protease. *Phys. Chem. Chem. Phys.*, 11(35):7599–7604, **2009**.

[27] J. Traube. The attraction pressure. *J. Phys. Chem.*, 14(5):452–470, **1910**.

[28] C. L. Henry, C. N. Dalton, L. Scruton et al. Ion-specific coalescence of bubbles in mixed electrolyte solutions. *J. Phys. Chem. C*, 111(2):1015–1023, **2007**.

[29] J. J. Garcia-Celma, L. Hatahet, W. Kunz et al. Specific Anion and Cation Binding to Lipid Membranes Investigated on a Solid Supported Membrane. *Langmuir*, 23(20):10074–10080, **2007**.

[30] H. I. Petrache, T. Zemb, L. Belloni et al. Salt screening and specific ion adsorption determine neutral-lipid membrane interactions. *Proc. Natl. Acad. Sci. U.S.A.*, 103(21):7982–7987, **2006**.

[31] Y. Zhang and P. S. Cremer. Interactions between macromolecules and ions: the Hofmeister series. *Curr. Opin. Chem. Biol.*, 10(6):658–663, **2006**.

[32] W. Kunz, L. Belloni, O. Bernard et al. Osmotic coefficients and surface tensions of aqueous electrolyte solutions: Role of dispersion forces. *J. Phys. Chem. B*, 108(7):2398–2404, **2004**.

[33] N. Vlachy, M. Drechsler, J.-M. Verbavatz et al. Role of the surfactant headgroup on the counterion specificity in the micelle-to-vesicle transition through salt addition. *J. Colloid Interface Sci.*, 319(2):542–548, **2008**.

[34] D. J. Tobias and J. C. Hemminger. Getting specific about specific ion effects. *Science*, 319(5867):1197–1198, **2008**.

[35] E. F. Aziz, N. Ottosson, S. Eisebitt et al. Cation-specific interactions with carboxylate in amino acid and acetate aqueous solutions: X-ray absorption and ab initio calculations. *J. Phys. Chem. B*, 112(40):12567–12570, **2008**.

[36] J. S. Uejio, C. P. Schwartz, A. M. Duffin et al. Characterization of selective binding of alkali cations with carboxylate by x-ray absorption spectroscopy of liquid microjets. *Proc. Natl. Acad. Sci. U. S. A.*, 105(19):6809–6812, **2008**.

[37] G. Neilson and J. Enderby. Aqueous solutions and neutron scattering. *J. Phys. Chem.*, 100(4):1317–1322, **1996**.

[38] P. Petersen and R. Saykally. On the nature of ions at the liquid water surface. *Annu. Rev. Phys. Chem.*, 57:333–364, **2006**.

[39] C. Raduge, V. Pflumio and Y. Shen. Surface vibrational spectroscopy of sulfuric acid-water mixtures at the liquid-vapor interface. *Chem. Phys. Lett.*, 274(1-3):140–144, **1997**.

[40] M. Shultz, S. Baldelli, C. Schnitzer et al. Aqueous solution/air interfaces probed with sum frequency generation spectroscopy. *J. Phys. Chem. B*, 106(21):5313–5324, **2002**.

[41] P. A. Franken, A. E. Hill, C. W. Peters et al. Generation of Optical Harmonics. *Phys. Rev. Lett.*, 7:118–119, **1961**.

[42] P. Petersen, R. Saykally, M. Mucha et al. Enhanced concentration of polarizable anions at the liquid water surface: SHG spectroscopy and MD simulations of sodium thiocyanide. *J. Phys. Chem. B*, 109(21):10915–10921, **2005**.

[43] P. Petersen and R. Saykally. Adsorption of ions to the surface of dilute electroyte solutions: The Jones-Ray effect revisited. *J. Am. Chem. Soc.*, 127(44):15446–15452, **2005**.

[44] A. Omta, M. Kropman, S. Woutersen et al. Negligible effect of ions on the hydrogen-bond structure in liquid water. *Science*, 301(5631):347–349, **2003**.

[45] J. Batchelor, A. Olteanu, A. Tripathy et al. Impact of protein denaturants and stabilizers on water structure. *J. Am. Chem. Soc.*, 126(7):1958–1961, **2004**.

[46] M. Gurau, S. Lim, E. Castellana et al. On the mechanism of the Hofmeister effect. *J. Am. Chem. Soc.*, 126(34):10522–10523, **2004**.

[47] L. M. Pegram and M. T. Record, Jr. Quantifying accumulation or exclusion of H+, HO-, and Hofmeister salt ions near interfaces. *Chem. Phys. Lett.*, 467(1-3):1–8, **2008**.

[48] K. D. Collins, G. W. Neilson and J. E. Enderby. Ions in water: Characterizing the forces that control chemical processes and biological structure. *Biophys. Chem.*, 128:95–104, **2007**.

[49] K. Collins. Charge density-dependent strength of hydration and biological structure. *Biophys. J.*, 72(1):65–76, **1997**.

[50] P. Debye and E. Hückel. Zur Theorie der Elektrolyte. I. Gefrierpunktserniedrigung und verwandte Erscheinungen (Lowering of freezing point and related phenomena). *Z. Phys.*, 24:185–206, **1923**.

[51] G. Gouy. Constitution of the Electric Charge at the Surfaces of an Electrolyte. *J. Phys. (France)*, 9(4):457–467, **1910**.

[52] D. L. Chapman. A Contribution to the Theory of Electrocapillarity. *Philos. Mag.*, 25(148):475–481, **1913**.

[53] L. Onsager and N. N. T. Samaras. The Surface Tension of Debye-Hückel Electrolytes. *J. Chem. Phys.*, 2(8):528–536, **1934**.

[54] B. Conway. State of water and hydrated ions at interfaces. *Adv. Colloid Interface Sci.*, 8(2-3):91–211, **1977**.

[55] L. Buhiyan, D. Bratko and C. Outhwaite. Electrolyte surface-tension in the modified Poisson-Boltzmann approximation. *J. Phys. Chem.*, 95(1):336–340, **1991**.

[56] M. Boström, D. R. M. Williams and B. W. Ninham. Specific Ion Effects: Why DLVO Theory Fails for Biology and Colloid Systems. *Phys. Rev. Lett.*, 87(16):168103, **2001**.

[57] S. Edwards and D. Williams. Double layers and interparticle forces in colloid science and biology: Analytic results for the effect of ionic dispersion forces. *Phys. Rev. Lett.*, 92(24):248303, **2004**.

[58] D. Ben-Yaakov, D. Andelman and R. Podgornik. Dielectric decrement as a source of ion-specific effects. *J. Chem. Phys.*, 134(7):074705, **2011**.

[59] M. Boström, F. Tavares, S. Finet et al. Why forces between proteins follow different Hofmeister series for pH above and below pI. *Biophys. Chem.*, 117(3):217–224, **2005**.

[60] B. W. Ninham and V. Yaminsky. Ion Binding and Ion Specificity: The Hofmeister Effect and Onsager and Lifshitz Theories. *Langmuir*, 13(7):2097–2108, **1997**.

[61] K. Karraker and C. Radke. Disjoining pressures zeta potentials and surface tensions of aqueous non-ionic surfactant/electrolyte solutions: theory and comparison to experiment. *Adv. Colloid Interface Sci.*, 96(1-3):231–264, **2002**.

[62] M. Manciu and E. Ruckenstein. Specific ion effects via ion hydration: I. Surface tension. *Adv. Colloid Interface Sci.*, 105:63–101, **2003**.

[63] A. P. Dos Santos and Y. Levin. Ion Specificity and the Theory of Stability of Colloidal Suspensions. *Phys. Rev. Lett.*, 106(16):167801, **2011**.

[64] P. Jungwirth. Spiers Memorial Lecture: Ions at aqueous interfaces. *Faraday Discus.*, 141:9–30, **2009**.

[65] P. Jungwirth and D. J. Tobias. Specific Ion Effects at the Air/Water Interface. *J. Chem. Rev.*, 106(4):1259–1281, **2006**.

[66] D. Horinek, A. Herz, L. Vrbka et al. Specific ion adsorption at the air/water interface: The role of hydrophobic solvation. *Chem. Phys. Lett.*, 479(4-6):173–183, **2009**.

[67] M. Lund, L. Vrbka and P. Jungwirth. Specific ion binding to nonpolar surface patches of proteins. *J. Am. Chem. Soc.*, 130(35):11582–11583, **2008**.

[68] D. Horinek, S. I. Mamatkulov and R. R. Netz. Rational design of ion force fields based on thermodynamic solvation properties. *J. Chem. Phys.*, 130(12):124507, **2009**.

[69] Y. Zhang and P. S. Cremer. The inverse and direct Hofmeister series for lysozyme. *Proc. Natl. Acad. Sci. U.S.A.*, 106(36):15249–15253, **2009**.

[70] S. Finet, F. Skouri-Panet, M. Casselyn et al. The Hofmeister effect as seen by SAXS in protein solutions. *Curr. Opin. Colloid Interface Sci.*, 9(1-2):112 – 116, **2004**.

[71] T. López-León, A. B. Jódar-Reyes, D. Bastos-González et al. Hofmeister Effects in the Stability and Electrophoretic Mobility of Polystyrene Latex Particles. *J. Phys. Chem. B*, 107(24):5696–5708, **2003**.

[72] T. López-León, A. Jódar-Reyes, J. Ortega-Vinuesa et al. Hofmeister effiects on the colloidal stability of an IgG-coated polystyrene latex. *J. Colloid Interface Sci.*, 284(1):139–148, **2005**.

[73] J. Lyklema. Simple Hofmeister series. *Chem. Phys. Lett.*, 467(4-6):217–222, **2009**.

[74] T. López-León, M. J. Santander-Ortega, J. L. Ortega-Vinuesa et al. Hofmeister Effects in Colloidal Systems: Influence of the Surface Nature. *J. Phys. Chem. C*, 112(41):16060–16069, **2008**.

[75] T. Robertson. Contributions to the theory of the mode of action of inorganic salts upon proteins in solution. *J. Biol. Chem.*, 9(3):303–326, **1911**.

[76] H. Kim, E. Tuite, B. Norden et al. Co-ion dependence of DNA nuclease activity suggests hydrophobic cavitation as a potential source of activation energy. *Eur. Phys. J. E*, 4(4):411–417, **2001**.

[77] A. Haertl, J. A. Garrido, S. Nowy et al. The ion sensitivity of surface conductive single crystalline diamond. *J. Am. Chem. Soc.*, 129(5):1287–1292, **2007**.

[78] S. Jenkins, W. Heineman and H. Halsall. Extending the detection limit of solid-phase electrochemical enzyme-immunoassay to the attomole level. *Analy. Biochem.*, 168(2):292–299, **1988**.

[79] J. Schakenraad and Busscher. Cell polymer interactions - the influence of protein adsorption. *Colloid Surface*, 42(3-4):331–343, **1989**.

[80] S. W. Schneider, S. Nuschele, A. Wixforth et al. Shear-induced unfolding triggers adhesion of von Willebrand factor fibers. *Proc. Natl. Acad. Sci.*, 104(19):7899–7903, **2007**.

[81] A. Rosenhahn, S. Schilp, H. J. Kreuzer et al. The role of "inert" surface chemistry in marine biofouling prevention. *Phys. Chem. Chem. Phys.*, 12(17):4275–4286, **2010**.

[82] M. S. Powell and N. K. H. Slater. Removal rates of bacterial cells from glass surfaces by fluid shear. *Biotechnol. Bioeng.*, 24(11):2527–2537, **1982**.

[83] E. Ostuni, R. G. Chapman, R. E. Holmlin et al. A Survey of StructureâĹŠProperty Relationships of Surfaces that Resist the Adsorption of Protein. *Langmuir*, 17(18):5605–5620, **2001**.

[84] A. Rosenhahn, J. A. Finlay, M. E. Pettit et al. Zeta potential of motile spores of the green alga Ulva linza and the influence of electrostatic interactions on spore settlement and adhesion strength. *Biointerphases*, 4(1):7–11, **2009**.

[85] E. Vogler. Structure and reactivity of water at biomaterial surfaces. *Adv. Colloid Interface Sci.*, 74:69–117, **1998**.

[86] J. M. Berg, L. G. T. Eriksson, P. M. Claesson et al. Three-Component Langmuir-Blodgett Films with a Controllable Degree of Polarity. *Langmuir*, 10(4):1225–1234, **1994**.

[87] M. Hoefling, F. Iori, S. Corni et al. Interaction of Amino Acids with the Au(111) Surface: Adsorption Free Energies from Molecular Dynamics Simulations. *Langmuir*, 26(11):8347–8351, **2010**. PMID: 20426434.

[88] A. Serr, D. Horinek and R. R. Netz. Polypeptide friction and adhesion on hydrophobic and hydrophilic surfaces: A molecular dynamics case study. *J. Am. Chem. Soc.*, 130(37):12408–12413, **2008**.

[89] D. Horinek, A. Serr, M. Geisler et al. Peptide adsorption on a hydrophobic surface results from an interplay of solvation, surface, and intrapeptide forces. *Proc. Natl. Acad. Sci. U.S.A.*, 105(8):2842–2847, **2008**.

[90] D. Horinek, A. Serr, D. J. Bonthuis et al. Molecular Hydrophobic Attraction and Ion-Specific Effects Studied by Molecular Dynamics. *Langmuir*, 24(4):1271–1283, **2008**.

[91] X. Chatellier, T. Senden, J. Joanny et al. Detachment of a single polyelectrolyte chain adsorbed on a charged surface. *Europhys. Lett.*, 41(3):303–308, **1998**.

[92] T. Hugel and M. Seitz. The study of molecular interactions by AFM force spectroscopy. *Macromol. Rapid Commun.*, 22(13):989–1016, **2001**.

[93] M. Seitz, C. Friedsam, W. Jostl et al. Probing solid surfaces with single polymers. *Chem. Phys. Chem.*, 4(9):986–990, **2003**.

[94] R. Breslow and T. Guo. Surface tension measurements show that chaotropic salting-in denaturants are not just water-structure breakers. *Proc. Natl. Acad. Sci. U.S.A.*, 87(1):167–169, **1990**.

[95] T. Lin and S. Timasheff. On the role of surface tension in the stabilization of globular proteins. *Protein Sci.*, 5(2):372–381, **1996**.

[96] M. Record, W. Zhang and C. Anderson. Analysis of effects of salts and uncharged solutes on protein and nucleic acid equilibria and processes: A practical guide to recognizing and interpreting polyelectrolyte effects, Hofmeister effects, and osmotic effects of salts. *Adv. Protein Chem.*, 51:281–353, **1998**.

[97] S. Timasheff. Control of protein stability and reactions by weakly interacting cosolvents: The simplicity of the complicated. *Adv. Protein Chem.*, 51:355–432, **1998**.

[98] B. Hess and N. F. A. van der Vegt. Cation specific binding with protein surface charges. *Proc. Natl. Acad. Sci. U.S.A.*, 106(32):13296–13300, **2009**.

[99] P. Smith. Computer simulation of cosolvent effects on hydrophobic hydration. *J. Phys. Chem. B*, 103(3):525–534, **1999**.

[100] A. S. Thomas and A. H. Elcock. Molecular dynamics simulations of hydrophobic associations in aqueous salt solutions indicate a connection between water hydrogen bonding and the Hofmeister effect. *J. Am. Chem. Soc.*, 129(48):14887–14898, **2007**.

[101] S. Pal and F. Müller-Plathe. Molecular Dynamics Simulation of Aqueous NaF and NaI Solutions near a Hydrophobic Surface. *J. Phys. Chem. B*, 109(13):6405–6415, **2005**.

[102] R. Zangi, M. Hagen and B. J. Berne. Effect of ions on the hydrophobic interaction between two plates. *J. Am. Chem. Soc.*, 129(15):4678–4686, **2007**.

[103] T.-M. Chang and L. X. Dang. Recent Advances in Molecular Simulations of Ion Solvation at Liquid Interfaces. *Chem. Rev.*, 106(4):1305–1322, **2006**.

[104] S. Marčelja. Selective coalescence of bubbles in simple electrolytes. *J. Phys. Chem. B*, 110(26):13062–13067, **2006**.

[105] D. Horinek, A. Serr, D. J. Bonthuis et al. Molecular Hydrophobic Attraction and Ion-Specific Effects Studied by Molecular Dynamics. *Langmuir*, 24(4):1271–1283, **2008**.

[106] M. Lund, P. Jungwirth and C. E. Woodward. Ion Specific Protein Assembly and Hydrophobic Surface Forces. *Phys. Rev. Lett.*, 100(25):258105, **2008**.

[107] W. R. P. Scott, P. H. Hunenberger, I. G. Tironi et al. The GROMOS Biomolecular Simulation Program Package. *J. Phys. Chem. A*, 103(19):3596–3607, **1999**.

[108] H. J. C. Berendsen, J. R. Grigera and T. P. Straatsma. The missing term in effective pair potentials. *J. Phys. Chem.*, 91(24):6269–6271, **1987**.

[109] M. Fyta, I. Kalcher, J. Dzubiella et al. Ionic force field optimization based on single-ion and ion-pair solvation properties. *J. Chem. Phys.*, 132(2):024911, **2010**.

[110] F. Sedlmeier, J. Janecek, C. Sendner et al. Water at polar and nonpolar solid walls. *Biointerphases*, 3(3):FC23–FC39, **2008**.

[111] U. Essmann, L. Perera, M. L. Berkowitz et al. A smooth particle mesh Ewald method. *J. Chem. Phys.*, 103(19):8577–8593, **1995**.

[112] G. M. Torrie and J. P. Valleau. Nonphysical sampling distributions in Monte Carlo free-energy estimation: Umbrella sampling. *J. Comput. Phys.*, 23(2):187–199, **1977**.

[113] S. Kumar, J. M. Rosenberg, D. Bouzida et al. Multidimensional Free-Energy Calculations Using the Weighted Histogram Analysis Method. *J. Comput. Chem.*, 16(11):1339–1350, **1995**.

[114] D. Van Der Spoel, E. Lindahl, B. Hess et al. GROMACS: Fast, flexible, and free. *J. Comput. Chem.*, 26(16):1701–1718, **2005**.

[115] G. Luo, S. Malkova, J. Yoon et al. Ion Distributions near a Liquid-Liquid Interface. *Science*, 311(5758):216–218, **2006**.

[116] D. Evans and H. Wennerström. *The Colloidal Domain: Where Physics, Chemistry, Biology and Technology Meet* (Wiley-VCH, New York), 2nd edition, **1999**.

[117] V. A. Parsegian and D. Gingell. On the Electrostatic Interaction across a Salt Solution between Two Bodies Bearing Unequal Charges. *Biophys. J.*, 12(9):1192–1204, **1972**.

[118] M. Dishon, O. Zohar and U. Sivan. From Repulsion to Attraction and Back to Repulsion: The Effect of NaCl, KCl, and CsCl on the Force between Silica Surfaces in Aqueous Solution. *Langmuir*, 25(5):2831–2836, **2009**.

[119] C. Sendner, D. Horinek, L. Bocquet et al. Interfacial Water at Hydrophobic and Hydrophilic Surfaces: Slip, Viscosity, and Diffusion. *Langmuir*, 25(18):10768–10781, **2009**.

[120] J. Janecek and R. Netz. Interfacial Water at Hydrophobic and Hydrophilic Surfaces: Depletion versus Adsorption. *Langmuir*, 23(16):8417–8429, **2007**.

[121] H. Boroudjerdi, Y.-W. Kim, A. Naji et al. Statics and dynamics of strongly charged soft matter. *Physics Reports*, 416(3-4):129–199, **2005**.

[122] R. Aveyard and S. Saleem. Interfacial-Tension at alkane-aqueous electrolyte interfaces. *J. Chem. Soc. Farad. T1*, 72:1609–1617, **1976**.

[123] R. Aveyard, S. Saleem and R. Heselden. Desorption of electrolytes at liquid-vapor and liquid-liquid interfaces. *J. Chem. Soc. Farad. T1*, 73:84–94, **1977**.

[124] P. Nandi and D. Robinson. Effects of Salts on Free-Energies of Nonpolar Groups in Model Peptides. *J. Am. Chem. Soc.*, 94(4):1308–1315, **1972**.

[125] P. Koelsch, P. Viswanath, H. Motschmann et al. Specific ion effects in physicochemical and biological systems: Simulations, theory and experiments. *Colloid Surf. A*, 303(1-2):110–136, **2007**.

[126] W. F. McDevit and F. A. Long. The Activity Coefficient of Benzene in Aqueous Salt Solutions. *J. Am. Chem. Soc.*, 74(7):1773–1777, **1952**.

[127] Specific ion effects in colloidal and biological systems. *Curr. Opin. Colloid Interface Sci.*, 15(1-2):34–39, **2010**.

[128] L. M. Pegram and M. T. Record, Jr. Thermodynamic origin of Hofmeister ion effects. *J. Phys. Chem. B*, 112(31):9428–9436, **2008**.

[129] P. Benas, L. Legrand and M. Ries-Kautt. Strong and specific effects of cations on lysozyme chloride solubility. *Acta Crystallogr. Sect. D-Biol. Crystallogr.*, 58(Part 10, 1):1582–1587, **2002**.

[130] F. Dumont, J. Warlus and A. Watillon. Influence of the point of zero charge of titanium-dioxide hydrosols on the ionic adsorption sequences. *J. Colloid Interface Sci.*, 138(2):543–554, **1990**.

[131] R. Sprycha. Electrical double-layer at alumina electrolyte interface. 1. Surface-charge and zeta potential. *J. Colloid Interface Sci.*, 127(1):1–11, **1989**.

[132] A. Green. Studies in the physical chemistry of the proteins X. The solubility of hemoglobin in solutions of chlorides and sulfates of varying concentration. *J. Biol. Chem.*, 95(1):47–66, **1932**.

[133] W. Poillon and J. Bertles. Deoxygenated sickle hemoglobin - effects of lyotropic salt on its solubility. *J. Biol. Chem.*, 254(9):3462–3467, **1979**.

[134] A. Salis, M. S. Bhattacharyya and M. Monduzzi. Specific Ion Effects on Adsorption of Lysozyme on Functionalized SBA-15 Mesoporous Silica. *J. Phys. Chem. B*, 114(23):7996–8001, **2010**.

[135] P. Jungwirth and D. J. Tobias. Molecular Structure of Salt Solutions:A New View of the Interface with Implications for Heterogeneous Atmospheric Chemistry. *J. Phys. Chem. B*, 105(43):10468–10472, **2001**.

[136] D. Horinek and R. R. Netz. Specific Ion Adsorption at Hydrophobic Solid Surfaces. *Phys. Rev. Lett.*, 99(22):226104, **2007**.

[137] P. Weissenborn and R. Pugh. Surface tension of aqueous solutions of electrolytes: Relationship with ion hydration, oxygen solubility, and bubble coalescence. *J. Colloid Interf. Sci.*, 184(2):550–563, **1996**.

[138] P. Bauduin, A. Renoncourt, D. Touraud et al. Hofmeister effect on enzymatic catalysis and colloidal structures. *Curr. Opin. Colloid Interface Sci.*, 9(1-2):43–47, **2004**.

[139] L. M. Pegram and M. T. Record, Jr. Hofmeister salt effects on surface tension arise from partitioning of anions and cations between bulk water and the air-water interface. *J. Phys. Chem. B*, 111(19):5411–5417, **2007**.

[140] G. Hummer, S. Garde, A. E. Garcia et al. An information theory model of hydrophobic interactions. *Proc. Natl. Acad. Sci.*, 93(17):8951–8955, **1996**.

[141] D. M. Huang, C. Cottin-Bizonne, C. Ybert et al. Aqueous electrolytes near hydrophobic surfaces: Dynamic effects of ion specificity and hydrodynamic slip. *Langmuir*, 24(4):1442–1450, **2008**.

[142] M. Lund, P. Jungwirth and C. E. Woodward. Ion Specific Protein Assembly and Hydrophobic Surface Forces. *Phys. Rev. Lett.*, 100(25):258105, **2008**.

[143] T. Waigh. *Applied biophysics: a molecular approach for physical scientists* (World Scientific Publishing, Singapore), 1st edition, **2010**.

[144] L. Vrbka, J. Vondrasek, B. Jagoda-Cwiklik et al. Quantification and rationalization of the higher affinity of sodium over potassium to protein surfaces. *Proc. Natl. Acad. Sci. U. S. A.*, 103(42):15440–15444, **2006**.

[145] J. Dzubiella. Salt-specific stability and denaturation of a short salt-bridge-forming alpha-helix. *J. Am. Chem. Soc.*, 130(42):14000–14007, **2008**.

[146] M. H. Stipanuk. *Biochemical and Physiological Aspects of Human Nutrition* (W.B. Saunders Company, Philadelphia), 2 edition, **2000**.

[147] T. Brody. *Nutritional Biochemistry.* (Academic Press, San Diego), 2 edition, **1999**.

[148] K. Hu and A. Bard. Use of atomic force microscopy for the study of surface acid-base properties of carboxylic acid-terminated self-assembled monolayers. *Langmuir*, 13(19):5114–5119, **1997**.

[149] I. Kalcher, J. C. F. Schulz and J. Dzubiella. Ion-Specific Excluded-Volume Correlations and Solvation Forces. *Phys. Rev. Lett.*, 104(9):097802, **2010**.

[150] E. Leontidis, A. Aroti, L. Belloni et al. Effects of monovalent anions of the Hofmeister series on DPPC lipid Bilayers part II: Modeling the perpendicular and lateral equation-of-state. *Biophys. J.*, 93(5):1591–1607, **2007**.

[151] T. Zemb, L. Belloni, M. Dubois et al. Can we use area per surfactant as a quantitative test model of specific ion effects? *Curr. Opin. Colloid Interface Sci.*, 9(1-2):74–80, **2004**.

[152] H. Petrache, I. Kimchi, D. Harries et al. Measured depletion of ions at the biomembrane interface. *J. Am. Chem. Soc.*, 127(33):11546–11547, **2005**.

[153] V. Padmanabhan, J. Daillant, L. Belloni et al. Specific ion adsorption and short-range interactions at the air aqueous solution interface. *Phys. Rev. Lett.*, 99(8):086105, **2007**.

[154] I. Kalcher and J. Dzubiella. Structure-thermodynamics relation of electrolyte solutions. *J. Chem. Phys.*, 130(13):134507, **2009**.

[155] R. Zangi. Can Salting-In/Salting-Out Ions be Classified as Chaotropes/Kosmotropes? *J. Phys. Chem. B*, 114(1):643–650, **2010**.

[156] E. Schneck and R. R. Netz. From simple surface models to lipid membranes: Universal aspects of the hydration interaction from solvent-explicit simulations. *Curr. Opin. Colloid Interface Sci.*, in press, **2011**.

[157] I. Kalcher, J. C. F. Schulz and J. Dzubiella. Electrolytes in a nanometer slab-confinement: Ion-specific structure and solvation forces. *J. Chem. Phys.*, 133(16):164511, **2010**.

[158] J. Forsman. Ion Adsorption and Lamellar-Lamellar Transitions in Charged Bilayer Systems. *Langmuir*, 22(7):2975–2978, **2006**.

[159] B. Ninham and V. Parsegian. Electrostatic potential between surfaces bearing ionizable groups in ionic equilibrium with physiological saline solution. *J. Theor. Biol.*, 31(3):405–428, **1971**.

[160] D. Harries, R. Podgornik, V. A. Parsegian et al. Ion induced lamellar-lamellar phase transition in charged surfactant systems. *J. Chem. Phys.*, 124(22):224702, **2006**.

[161] R. Podgornik. Electrostatic correlation forces between surfaces with surface specific ionic interactions. *J. Chem. Phys.*, 91(9):5840–5849, **1989**.

[162] I. Gradshteyn and I. Ryzhik. *Table of Integrals, Series, and Products* (Academic Press, Inc), 5th edition, **1994**.

[163] A. Abramowitz and I. Stegun. *Handbook of Mathematical Functions with Formulas, Graphs, and Mathematical Tables* (National Bureau of Standards), 10th edition, **1972**.

[164] A. McPherson. Introduction to protein crystallization. *Methods*, 34(3):254–265, **2004**.

[165] S. Marcelja and N. Radic. Repulsion of interfaces due to boundary water. *Chem. Phys Lett.*, 42(1):129–130, **1976**.

[166] D. Gruen and S. Marcelja. Spatially varying polarization in water - a model for the electric double-layer and the hydration force. *J. Chem. Soc. Faraday Trans.II*, 79(2):225–242, **1983**.

[167] S. Schilp, A. Kueller, A. Rosenhahn et al. Settlement and adhesion of algal cells to hexa (ethylene glycol)-containing self-assembled monolayers with systematically changed wetting properties. *Biointerphases*, 2(4):143–150, **2007**.

[168] S. Jeon, J. Lee, J. Andrade et al. Protein surface interactions in the presence of polyethylene oxide. 1. Simplified theory. *J. Colloid Interface Sci.*, 142(1):149–158, **1991**.

[169] S. Jeon and J. Andrade. Protein surface interactions in the presence of polyethylene oxide. 2. Effect of protein size. *J. Colloid Interface Sci.*, 142(1):159–166, **1991**.

[170] S. Schilp, A. Rosenhahn, M. E. Pettitt et al. Physicochemical Properties of (Ethylene Glycol)-Containing Self-Assembled Monolayers Relevant for Protein and Algal Cell Resistance. *Langmuir*, 25(17):10077–10082, **2009**.

[171] R. Wang, H. Kreuzer and M. Grunze. Molecular conformation and solvation of oligo(ethylene glycol)-terminated self-assembled monolayers and their resistance to protein adsorption. *J. Phys. Chem. B*, 101(47):9767–9773, **1997**.

[172] L. Ista, M. Callow, J. Finlay et al. Effect of substratum surface chemistry and surface energy on attachment of marine bacteria and algal spores. *Appl. Environ. Microbiol.*, 70(7):4151–4157, **2004**.

[173] J. Finlay, M. Callow, L. Ista et al. The influence of surface wettability on the adhesion strength of settled spores of the green alga Enteromorpha and the diatom Amphora. *Integr. Comp. Biol.*, 42(6):1116–1122, **2002**.

[174] Y. Wei and R. A. Latour. Benchmark Experimental Data Set and Assessment of Adsorption Free Energy for Peptide-Surface Interactions. *Langmuir*, 25(10):5637–5646, **2009**.

[175] B. Marshall, M. Long, J. Piper et al. Direct observation of catch bonds involving cell-adhesion molecules. *Nature*, 423(6936):190–193, **2003**.

[176] R. Latour and C. Rini. Theoretical analysis of adsorption thermodynamics for hydrophobic peptide residues on SAM surfaces of varying functionality. *J. Biomed. Mater Res.*, 60(4):564–577, **2002**.

[177] J. Janecek and R. Netz. Interfacial Water at Hydrophobic and Hydrophilic Surfaces: Depletion versus Adsorption. *Langmuir*, 23(16):8417–8429, **2007**.

[178] A. Katchalsky, N. Shavit and H. Eisenberg. Dissociation of weak polymeric acids and bases. *J. Polym. Sci.*, 13(68):69–84, **1954**.

[179] R. R. Netz. Charge regulation of weak polyelectrolytes at low- and high-dielectric-constant substrates. *J. Phys. Condens. Mat.*, 15(1):S239, **2003**.

[180] H. Berendsen, J. Postma, W. van Gunsteren et al. Molecular-dynamics with coupling to an external bath. *J. Chem. Phys.*, 81(8):3684–3690, **1984**.

[181] T. Darden, D. York and L. Pedersen. Particle Mesh Ewald - an N.log(N) method for Ewald sums in large systems. *J. Chem. Phys.*, 98(12):10089–10092, **1993**.

[182] T. Pirzer, M. Geisler, T. Scheibel et al. Single molecule force measurements delineate salt, pH and surface effects on biopolymer adhesion. *Phys. Biol.*, 6(2):025004, **2009**.

[183] A. F. Stalder, G. Kulik, D. Sage et al. A snake-based approach to accurate determination of both contact points and contact angles. *Colloid Surf. A*, 286(1-3):92–103, **2006**.

[184] S. Black and D. Mould. Development of hydrophobicity parameters to analyze proteins which bear posttranslational or cotranslational modifications. *Anal. Biochem.*, 193(1):72–82, **1991**.

[185] R. Rekker. *The hydrophobic fragmental constant* (Elsevier Scientific Publishing Company, Amsterdam), **1977**.

[186] K. Dill. Additivity principles in biochemistry. *J. Biol. Chem.*, 272(2):701–704, **1997**.

[187] D. Horinek and R. R. Netz. Can Simulations Quantitatively Predict Peptide Transfer Free Energies to Urea Solutions? Thermodynamic Concepts and Force Field Limitations. *J. Phys. Chem. A*, 115(23):6125–6136, **2011**.

[188] E. E. Meyer, K. J. Rosenberg and J. Israelachvili. Recent progress in understanding hydrophobic interactions. *Proc. Natl. Acad. Sci. U.S.A.*, 103(43):15739–15746, **2006**.

[189] D. Chandler. Interfaces and the driving force of hydrophobic assembly. *Nature*, 437(7059):640–647, **2005**.

[190] N. Singh and S. M. Husson. Adsorption thermodynamics of short-chain peptides on charged and uncharged nanothin polymer films. *Langmuir*, 22(20):8443–8451, **2006**.

[191] J. F. Schumacher, M. L. Carman, T. G. Estes et al. Engineered antifouling microtopographies - effect of feature size, geometry, and roughness on settlement of zoospores of the green alga Ulva. *Biofouling*, 23(1):55–62, **2007**.

[192] J. Hester, P. Banerjee and A. Mayes. Preparation of protein-resistant surfaces on poly(vinylidene fluoride) membranes via surface segregation. *Macromolecules*, 32(5):1643–1650, **1999**.

[193] T. E. Creighton. *Proteins Structure and Molecular Properties* (W. H. Freeman & Co, New York), 2nd edition, **1993**.